2015

Ab initio approach to quantum field theories on the light front

Yang Li
Iowa State University

***Ab initio* approach to quantum field theories on the light front**

by

Yang Li

A dissertation submitted to the graduate faculty

in partial fulfillment of the requirements for the degree of

DOCTOR OF PHILOSOPHY

Major: Nuclear Physics

Program of Study Committee:
James P. Vary, Co-major Professor
Kirill Tuchin, Co-major Professor
Craig A. Ogilvie
Pieter Maris
Marshall Luban
Tathagata Basak

Iowa State University

Ames, Iowa

2015

DEDICATION

This thesis is dedicated to my parents.

TABLE OF CONTENTS

ACKNOWLEDGEMENTS v

ABSTRACT vii

CHAPTER 1. QUANTUM FIELD THEORY ON THE LIGHT FRONT . . 1

1.1 Quantum Field Theory 2

1.2 Lorentz Symmetry 4

1.3 Light-Front Dynamics 6

1.4 Light-Front Quantization 10

1.5 Fock Space Representation 14

1.6 Non-Perturbative Methods 16

1.6.1 Light-Front Tamm-Dancoff coupled integral equations 17

1.6.2 Discretized Light-Cone Quantization 18

1.6.3 Basis Light-Front Quantization 19

1.6.4 Effective Hamiltonian 20

1.7 Motivation and Outline 22

CHAPTER 2. BASIS LIGHT-FRONT QUANTIZATION APPROACH TO HEAVY QUARKONIUM 24

2.1 Confinement from Light-Front Holography 25

2.1.1 Light-Front Holography 26

2.1.2 Longitudinal confinement 27

2.2 Effective One-Gluon Exchange 29

2.2.1 Effective interaction 30

2.2.2 Positronium 33

2.3 Basis Representation of Heavy Quarkonium . . . 35
2.3.1 Basis expansion . . . 36
2.3.2 Quantum number identification . . . 37
2.4 Numerical Results . . . 39
2.4.1 Spectroscopy . . . 40
2.4.2 Parton distributions . . . 43
2.4.3 Elastic form factors . . . 44
2.4.4 Decay constants . . . 49
CHAPTER 3. NON-PERTURBATIVE RENORMALIZATION . . . 53
3.1 Scalar Yukawa Model . . . 55
3.2 Fock Sector Dependent Renormalization . . . 57
3.2.1 Counterterms . . . 57
3.2.2 Renormalization conditions . . . 60
3.3 Truncation up to Two-Body $(\chi + \varphi)$ . . . 62
3.4 Truncation up to Three-Body $(\chi + 2\varphi)$ . . . 65
3.4.1 Eigenvalue equation and renormalization . . . 65
3.4.2 Numerical results . . . 66
3.4.3 Self-Energy function . . . 69
3.4.4 Fredholm critical coupling . . . 72
3.5 Truncation up to Four-Body $(\chi + 3\varphi)$ . . . 73
3.5.1 Eigenvalue equation and renormalization . . . 73
3.5.2 Numerical results . . . 79
3.6 Form Factor . . . 85
CHAPTER 4. CONCLUSIONS AND OUTLOOK . . . 89
APPENDIX A. CONVENTIONS . . . 92
APPENDIX B. JACOBI DIFFERENTIAL EQUATION . . . 103
APPENDIX C. ANGULAR INTEGRALS . . . 105
APPENDIX D. GAUSS QUADRATURES . . . 107
BIBLIOGRAPHY . . . 109

ACKNOWLEDGEMENTS

First and foremost, I wish to thank my advisor, Prof. James P. Vary, Ph.D. Not only he advised me on research, but also taught me to enjoy physics and research. He has always been supportive, patient and encouraging. He is the ideal Ph.D. advisor a graduate student can dream of. I also wish to thank Prof. Pieter Maris, Ph.D. He appears whenever I need help. I also benefit from his high standard and insightful critique. I could not forget thanking Prof. Xingbo Zhao, Ph.D. He is an inspiring mentor and a valuable colleague. With his passion and diligence in research, he is always a role model. I would like to thank Prof. Vladimir A. Karmanov, Ph.D. Collaborating with him is a real pleasure.

Paul W. Wiecki is a distinguished colleague and a great companion. I wish him success in experimental condensed matter physics. Tai Kong, Rui Jiang, Ph.D., Guangyao Chen, Ph.D., Tian Xin are good friends. I couldn't thank enough of them for their friendship.

It has been an great honor for me to work with Prof. Kirill Tuchin, Ph.D., Guangyao Chen, Ph.D., Lekha Adihkari, Ph.D. and Meijian Li. I would also like to express my appreciation to other committee members: Prof.'s Craig A. Ogilvie, Ph.D., Marshall Luban, Ph.D., Tathagata Basak, Ph.D., German Valencia, Ph.D. (ex-member) for their guidance and support throughout the course of my research.

I would like to take this opportunity to thank all those who helped me in various ways for conducting research and the writing of this thesis, including but not limited to: Hugh D. Potter, Jun Li, Ph.D.'s, Prof. Taihua Heng, Ph.D., Prof. Andrey Shirokov, Ph.D., George Papadimitriou, Ph.D., Robert Holliday, A.V. Smirnov, Ph.D., Prof. Stanley J. Brodsky, Ph.D., Prof. Guy de Téramond, Ph.D., Arkadiusz P. Trawiński, Ph.D., Prof. Soeren Prell, Ph.D. and John R. Spence, Ph.D.

Finally, I wish to thank Jordan, Molly and other waiters and waitresses who brought me food and coffee/tea over the years, and gave me the first greetings of the day.

This work was supported in part by the Department of Energy under Grant Nos. DE-FG02-87ER40371. Computational resources were provided by the National Energy Research Supercomputer Center (NERSC), which is supported by the Office of Science of the U.S. Department of Energy under Contract No. DE-AC02-05CH11231.

ABSTRACT

We develop and apply methods for solving non-perturbative quantum field theories in the Hamiltonian formalism. The current work is a first step towards an *ab initio* approach to QCD bound-state problems.

In particular, we investigate heavy quarkonium within the basis light-front quantization approach. We implement a phenomenological confinement from the Light-Front Holographic QCD and a theoretically derived one-gluon exchange effective interaction. We adopt the holographic light-front wavefunctions as our basis and solve the bound-state problem by diagonalizing the Hamiltonian matrix. We obtain the mass spectrum for charmonium and bottomonium. We also compute the decay constants and the elastic form factors for selected mesons. The results compare favorably with experimental measurements and with other established methods.

We also address systematic non-perturbative renormalization in a simpler model, the scalar Yukawa model, using the a Fock sector dependent renormalization scheme. We apply the Fock sector truncation up to four constituent particles. The eigenvalue equation is properly renormalized and a set of coupled integral equations are derived. We solve these equations by a parallel numerical iterative procedure. We find that the lowest (one- and two-body) Fock sectors dominate the physical state up to a non-perturbative coupling $\alpha \approx 1.7$. By comparing with lower sector truncations, we show that the form factor converges with respect to the Fock sector expansion in the perturbative and non-perturbative regime. This calculation demonstrates the use of the systematic Fock sector expansion with a proper non-perturbative renormalization as an *ab initio* approach to solve light-front quantum field theory.

These results initiate a pathway for solving the strong interaction bound-state problems from first principles.

CHAPTER 1. QUANTUM FIELD THEORY ON THE LIGHT FRONT

The discovery of the Standard Model scalar boson (the Higgs boson) in 2012 with the Large Hadron Collider (LHC) at CERN, represents one of the great triumphs of quantum field theory [1, 2]. Indeed the Nobel Prize was given to two of the theorists who proposed the scalar field that completes the Standard Model and predicted the existence of such a particle, back in the 60s. Another well-known benchmark for the impressive success of quantum field theory is the prediction of the electron anomalous magnetic moment [3], which agrees with the experimentally measured value (CODATA 2014, [4]) up to the *eleventh* digit.

However, much of the success of quantum field theory is based on the perturbative approach. In this approach, calculations are done order-by-order in terms of the coupling constant α, and the physical observables are expressed as the power series of α up to the truncation order. Thus perturbation theory is only valid if the coupling constant α is small and the observable in consideration can be approximated by a finite power series[1]. Both conditions are violated by the bound-state problem in strong interaction physics, which is one of the central problems in nuclear physics. Therefore, solving quantum field theory in the non-perturbative regime is not only a theoretical challenge, but also essential to understand hadrons, strong interaction bound states, from first principles.

This thesis addresses the non-perturbative approach to quantum field theories within the so-called *light-front Hamiltonian* formalism [6]. We investigates some of the recently proposed non-perturbative approaches in the light-front Hamiltonian formalism, based on the research work performed by the author in collaboration with others. Special emphasis is placed on those

[1] As an counterexample, the bound-state spectrum of the hydrogen atom cannot be directly calculated from the perturbation theory, even though the coupling constant of quantum electrodynamics (QED) $\alpha_{\text{QED}} \approx 1/137$ is small. The bound-state spectrum and wavefunctions can be solved with the Schrödinger equation or with the Bethe-Salpeter equation and then perturbation theory can be applied for addition corrections. See, e.g., Ref. [5] for more discussions.

works where the author is also the lead author on the refereed publications. These explorations result in breakthroughs that will facilitate a possible pathway to the ultimate goal of solving for the bound states of the hadrons entirely from first principles — i.e. with no adjustable parameters aside from those in the initial Lagrangian. In order to demonstrate a range of observables accessible with the light-front Hamiltonian formalism, this thesis presents, among other advances, initial applications to heavy quark-antiquark bound states, charmonium and bottomonium.

This chapter provides the necessary background information of quantum field theory in the light-front Hamiltonian formulation. More detailed definitions and conventions are collected in the Appendix A. Expositions of quantum field theory can be found in any good textbook on the topic, e.g. Weinberg 2005 [7]. Introduction to light-front Hamiltonian theory can be found in the review papers on the topic, e.g. [8, 9, 10, 11, 12] and the references therein. We introduce the motivations of our work and outline the structure of the thesis at the end of this chapter.

Throughout this thesis, we use the natural units, $\hbar = c = 1$, unless otherwise stated.

1.1 Quantum Field Theory

Quantum field theory (QFT) is the quantum theory of relativistic fields and their interactions. The two essential ingredients of QFT are special relativity and quantum mechanics [7]. A quantum field, using mathematical terms, is an operator-valued distribution. The easiest way to visualize quantum fields is to consider the quantum vibrations of a 3-dimensional crystal lattice [13]. The generalized coordinates of the system in the Heisenberg picture are the displacements of the ions $\hat{q}_i(t)$, where the index $i = 1, 2, \cdots$ enumerates the ions. Taking the lattice spacing to zero, $\hat{q}_i(t)$ becomes a quantum field $\hat{q}(t, \boldsymbol{r})$ (phonon field), where the ion index has been replaced by a 3-dimensional coordinate vector $\boldsymbol{r} = (x, y, z)$ in the continuum limit. Therefore, QFT can be viewed as the theory of a many-body system with an infinite number of degrees of freedom.

The infinite number of degrees of freedom brings in new features to QFT. Two of these features are the infrared (IR) and ultraviolet (UV) divergences. Such divergences have to

be managed with care through mathematical procedures covered by the term "renormalization". Although renormalization is not limited to QFTs with divergences, most realistic QFTs would be crippled without renormalization — in particular, all known fundamental theories are renormalizable. Order-by-order renormalization in perturbation theory is widely practiced, but non-perturbative renormalization approaches are less developed. A specific approach to non-perturbative renormalization is also one of the major topics of this thesis and will be demonstrated within the scalar Yukawa model.

Another distinct feature of QFT is the emergence of the gauge symmetries. Gauge symmetries are local symmetries (i.e. symmetries depending on space-time) generated from Lie groups. These QFTs, known as the gauge theories, not only admit a beautiful geometric interpretation, but also find application in the description of the fundamental forces of nature. The Standard Model of particle physics is a gauge theory based on the product Lie group $\mathrm{SU}(3) \times \mathrm{SU}(2) \times \mathrm{U}(1)$, which describes the strong, weak and electromagnetic interactions in a unified framework. Of the three symmetry groups, SU(3) is associated with the quantum chromodynamics (QCD) which is one of the main focii of this thesis.

QCD is responsible for the strong interaction between quarks and gluons, as well as the nuclear force between protons and neutrons. One of the most striking properties of QCD is confinement, which states that while quarks and gluons are colored objects[2], no naturally occurring particles carry color. Quarks and gluons therefore are confined into colorless (color singlet) QCD bound states, known as hadrons. Confinement is a dynamical property and cannot be obtained from perturbation theory, as far as we know. The non-perturbative dynamics of QCD is believed also to be closely related to the dynamical generation of the majority part of the hadron masses. Furthermore, it is also responsible for binding nucleons together in a nucleus. Last but not least, non-perturbative QCD at finite temperature holds the key for understanding the hot dense matters occurring in heavy ion collisions and compact stars. Therefore, solving QCD in the non-perturbative regime is one of the central tasks of nuclear physics.

Lattice QCD [14], is considered as one of the most successful non-perturbative approaches.

[2]In QFT, in particular, QCD, "color" refers to an internal degree of freedom and is not related to the optical colors.

Lattice QCD is based on the path integral formulation of QCD in Euclidean space-time. It defines the quantum fields on a discretized lattice with a finite lattice spacing and evaluates the path integral using stochastic techniques. Typical observables calculated from Lattice QCD are the n-point functions, which can be used to extract additional observables including the bound-state masses. Derived from Schwringer's action principle [15], the Dyson-Schwinger equation (DSE) is another *ab initio* approach based on the Lagrangian formalism in Euclidean space-time [16]. In this approach, the n-pioint functions are solved from coupled integral equations.

In principle, diagonalizing the QCD Hamiltonian provides the hadron spectrum and wave-functions that describe mesons and baryons in terms of quark and gluon degrees of freedom in *Minkowski* space. This is the Hamiltonian formalism, an *ab initio* approach complementary to the Lagrangian formulations. Furthermore, the Hamiltonian formalism can also generate real-time evolution of quantum fields, valuable for heavy ion physics and strong field physics. However, diagonalizing the QCD Hamiltonian is a formidable task and remains a fundamental challenge in theoretical physics. This thesis investigates a particular Hamiltonian formalism of QFT (esp., QCD), known as the light-front quantum field theory (LFQFT). LFQFT defines quantum states on the light front $t + z$. The non-perturbative solutions are generated by diagonalizing the light-front Hamiltonian operator $P^- = (H - P_z)/2$. Reformulating the Hamiltonian on the light front makes a dramatic difference, and it has been shown that LFQFT is a natural framework for tackling relativistic bound-state problems [17]. We will formulate the problem later in this chapter, and discuss the possible ways to solve it.

1.2 Lorentz Symmetry

Einstein's special relativity demands that physical laws are invariant under the inhomogeneous Lorentz transformation of space-time coordinates $x = (x^0, x^1, x^2, x^3) \equiv (t, \boldsymbol{x})$:

$$x'^\mu = \Lambda^\mu_\nu x^\nu + a^\mu, \tag{1.1}$$

where $\mu, \nu = 0, 1, 2, 3$ are coordinate indices. Here and elsewhere paired repeating coordinate indices (ν in this example) are summed over, unless otherwise stated. a^μ is an arbitrary 4-vector

and Λ^μ_ν satisfies,

$$g_{\mu\nu}\Lambda^\mu_\alpha\Lambda^\nu_\beta = g_{\alpha\beta}, \tag{1.2}$$

where $g^{\mu\nu} = g_{\mu\nu} = \mathrm{diag}\{+1, -1, -1, -1\}$ is the *Minkowski* space metric tensor. The inhomogeneous Lorentz transformations form a group, $\mathrm{ISO}(3,1) \triangleq \mathbb{R}^{1,3} \rtimes \mathrm{SO}(3,1)$, called the Poincaré group in physics.

Quantum mechanics postulates that the quantum state of a system is modeled by a vector[3] of Hilbert space. Then the Lorentz symmetry is implemented as a unitary representation of the Poincaré algebra acting in that Hilbert space, whose 10 generators P^μ, $M^{\mu\nu}$ satisfy,

$$\begin{aligned} &\big[P^\mu, P^\nu\big] = 0, \qquad \big[P^\mu, M^{\alpha\beta}\big] = i\big(g^{\mu\alpha}P^\beta - g^{\mu\beta}P^\alpha\big), \\ &\big[M^{\mu\nu}, M^{\rho\sigma}\big] = i\big(g^{\mu\sigma}M^{\nu\rho} - g^{\nu\sigma}M^{\mu\rho} + g^{\nu\rho}M^{\mu\sigma} - g^{\mu\rho}M^{\nu\sigma}\big). \end{aligned} \tag{1.3}$$

Here $P^\mu = (P^0, P^1, P^2, P^3) \equiv (P^0, \boldsymbol{P})$ are the momentum operators, and $M^{\mu\nu} = -M^{\nu\mu}$, whose 6 components, $J^i = \frac{1}{2}\epsilon^{ijk}M^{jk}$, $K^i = M^{0i}$, are the rotation generators (i.e., the angular momentum operators) and the boost generators.

Note that four momentum operators commute with each other, and thus admit mutual eigenstates, i.e. quantum states labeled by a 4-momentum. Such states can be further identified by a complete set of mutually commuting operators. For Lorentz symmetry, one choices is [10, 11],

$$\big\{P^\mu, W^2 \equiv W_\mu W^\mu, W^+ \equiv W^0 + W^3\big\}, \quad W^\mu \equiv -\frac{1}{2}\varepsilon^{\mu\nu\rho\sigma}P_\nu M_{\rho\sigma} \tag{1.4}$$

where W^μ is called the Pauli-Lubanski vector. Then, the fully identified quantum states satisfy,

$$\hat{P}^\mu|p^\mu, j, m_j\rangle = p^\mu|p^\mu, j, m_j\rangle, \tag{1.5}$$

$$\hat{W}^2|p^\mu, j, m_j\rangle = -m^2 j(j+1)|p^\mu, j, m_j\rangle, \tag{1.6}$$

$$\hat{W}^+|p^\mu, j, m_j\rangle = p^+ m_j|p^\mu, j, m_j\rangle. \tag{1.7}$$

Here p^μ, j, m_j are c-numbers directly associated with the eigenvalues. $p^+ = p^0 + p^3$. $m^2 = P_\mu P^\mu \equiv P^2$ is a Casimir operator[4]. To distinguish from these c-numbers, we have put "hats"

[3] More precisely, a quantum state is modeled by a "ray" in a Hilbert space. The distinction, though non-trivial, usually can be circumvented due to the simple topology of the Poincaré group. See [7] for more discussions.

[4] The Poincaré algebra has two Casimir operators, P^2 and W^2.

on operators. We will drop the operator hats whenever there is no danger of confusion. The meanings of j, m_j can be made clear by introducing a vector, $\boldsymbol{\mathcal{J}} = (\mathcal{J}^1, \mathcal{J}^2, \mathcal{J}^3)$,

$$\mathcal{J}^3 = \frac{W^+}{P^+}, \ \boldsymbol{\mathcal{J}}^\perp = \frac{1}{m}(\boldsymbol{W}^\perp - \boldsymbol{P}^\perp \mathcal{J}^3), \tag{1.8}$$

where $P^+ = P^0 + P^3$, $\boldsymbol{\mathcal{J}}^\perp = (\mathcal{J}^1, \mathcal{J}^2)$. For simplicity, we only consider the massive states ($m > 0$) here. Components of this vector satisfy,

$$\left[\mathcal{J}^i, \mathcal{J}^j\right] = i\epsilon^{ijk}\mathcal{J}^k, \quad \boldsymbol{\mathcal{J}}^2 \equiv (\mathcal{J}^1)^2 + (\mathcal{J}^1)^2 + (\mathcal{J}^1)^2 = -W^2/m^2. \tag{1.9}$$

Therefore, $\{\mathcal{J}^1, \mathcal{J}^2, \mathcal{J}^3\}$ span an angular momentum algebra $< \mathcal{J}^1, \mathcal{J}^2, \mathcal{J}^3 > \simeq \mathfrak{su}_2$, and the eigenvalue Eqs. (1.5–1.7) becomes,

$$\hat{P}^\mu |p^\mu, j, m_j\rangle = p^\mu |p^\mu, j, m_j\rangle, \tag{1.10}$$

$$\hat{\boldsymbol{\mathcal{J}}}^2 |p^\mu, j, m_j\rangle = j(j+1)|p^\mu, j, m_j\rangle, \tag{1.11}$$

$$\hat{\mathcal{J}}^3 |p^\mu, j, m_j\rangle = m_j |p^\mu, j, m_j\rangle. \tag{1.12}$$

Therefore, j and m_j are the intrinsic total angular momentum[5] (spin) and its magnetic projection, respectively, and they satisfy $j = 0, \frac{1}{2}, 1, \frac{3}{2}, \cdots$, $-j \leq m_j \leq j$. According to Wigner, a quantum state $|p^\mu, j, m_j\rangle$ represents a particle with 4-momentum p^μ, spin j, and magnetic projection m_j [7]. Note that, according to the Wigner classification, there is no real distinction between elementary and composite particles [7]. Therefore, the mass spectrum and state vectors of a self-bound system can be unambiguously obtained from Eq.'s (1.10–1.12). In quantum field theories, these operators are constructed in terms of the quantum fields.

1.3 Light-Front Dynamics

Quantum mechanics postulates that the dynamical evolution of a quantum state $|\psi(t)\rangle$ is dictated by the Schrödinger equation,

$$i\frac{\partial}{\partial t}|\psi(t)\rangle = H|\psi(t)\rangle. \tag{1.13}$$

[5] One should beware of the possible confusion around the name "total angular momentum". Lorentz scalar $\boldsymbol{\mathcal{J}}^2$ represents the intrinsic part of the total angular momentum of a particle, i.e. the spin of the particle. The total angular momentum of the particle $\boldsymbol{J}^2$ is not a Lorentz scalar, as it takes into account not only the the intrinsic angular momentum (i.e. the spin), but also the orbital motion of the particle.

Table 1.1: Five forms of relativisitic dynamics.

	time parameter	Σ	kinematical	dynamical
instant form	$x^0 \equiv t$	$x^0 = 0$	$\boldsymbol{P}, \boldsymbol{J}$	P^0, $\boldsymbol{K}$
front form	$x^+ \equiv t + z$	$x^+ = 0$	P^+, $\boldsymbol{P}^\perp$, K^3, J^3, $K^1 + J^2$, $K^2 - J^1$	P^-, $J^1 + K^2$, $J^2 - K^1$
point form	$\tau \equiv (t^2 - \boldsymbol{x}^2 - a^2)^{\frac{1}{2}}$, $(t > 0)$	$\tau = 0$	$\boldsymbol{K}$, $\boldsymbol{J}$	P^0, $\boldsymbol{P}$
hyperboloid	$\tau_z \equiv (t^2 - z^2 - a^2)^{\frac{1}{2}}$, $(t > 0)$	$\tau_z = 0$	$\boldsymbol{P}^\perp$, K^3, J^3	$P^0, P^3, \boldsymbol{K}^\perp, \boldsymbol{J}^\perp$
hyperboloid	$\tau_\perp \equiv (t^2 - \boldsymbol{x}_\perp^2 - a^2)^{\frac{1}{2}}$, $(t > 0)$	$\tau_\perp = 0$	P^3, $\boldsymbol{K}^\perp$, J^3	$P^0, \boldsymbol{P}^\perp, K^3, \boldsymbol{J}^\perp$

Σ is the quantization surface. a is a non-zero constant, $a^2 > 0$. $\boldsymbol{x}_\perp^2 = x^2 + y^2$.

Here H is the Hamiltonian operator quantized at some instant of time, say $t = 0$. In relativity, however, time does not play any special role. Indeed, the time of a moving (in z-direction) inertial observer, relative to a stationary observer, according to the Lorentz transformation, is:

$$t' = \gamma_{\rm V}(t + \beta_{\rm V} z), \tag{1.14}$$

where $\beta_{\rm V} = V/c$, $\gamma_{\rm V} = (1 - \beta_{\rm V}^2)^{-\frac{1}{2}}$ depends on the velocity of the moving observer V. Therefore, equal-time quantization signifies different quantization surfaces for different observers. In this regards, it was Dirac who first pointed out that quantization in QFT can be generalized to additional forms of dynamics [6].

Each form is associated with a particular choice of time, the direction of dynamical evolution, and a quantization surface Σ defined at the initial "time". The quantum state of the system is defined at any fixed "time" slice. States at different "time" are related by dynamical evolution [8, 12].

Each form of dynamics also classifies the 10 generators of the Poincaré symmetry. If a Lorentz transformation preserves the quantization surface, its unitary representation, the quantum operator, does not involve the dynamical evolution, thus is "simple" [6, 8]. These transformations are called kinematical. Operators other than the kinematical ones are called dynamical operators, as they involve dynamical evolution directly. Usually, dynamical operators contain a non-diagonal part of the Hamiltonian, i.e., the interaction. Different forms of dynamics may have different kinematical operators.

With some fairly general requirements, there are in total five forms of relativistic dynamics

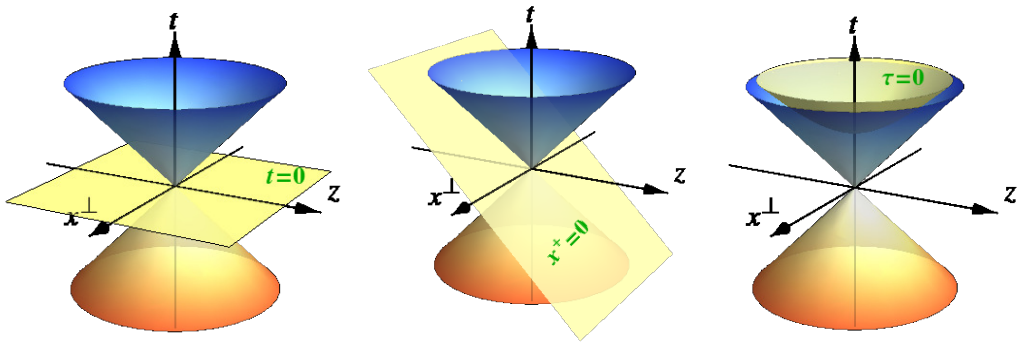

Figure 1.1: The quantization surfaces of the instant form (*left*), the front form (*center*) and the point form (*right*) in the (2+1) dimensions.

[8, 12]. These forms are summarized in Table 1.1 (see also Fig. 1.1). Of all five forms, the front form, the form selected for this thesis, has the maximal number of generators of kinematical operators, 7. The kinematical operators of the front form will be discussed in detail below.

Before introducing light-front dynamics, it is useful to introduce the light-front parametrization of variables first [9, 10, 11]. For a 4-vector $v = (v^0, v^1, v^2, v^3) \equiv (v^0, \boldsymbol{v})$, the light-front parameterization is, $v^\pm = v^0 + v^3$, $\boldsymbol{v}^\perp = (v^1, v^2)$. In particular, define light-front coordinates $x^\pm \equiv x^0 \pm x^3$, $\boldsymbol{x}^\perp = (x^1, x^2)$, and light-front momenta $p^\pm = p^0 \pm p^3$, $\boldsymbol{p}^\perp = (p^1, p^2)$. From the Lorentz invariant $p \cdot x = p^0 x^0 - \boldsymbol{p} \cdot \boldsymbol{x} = \frac{1}{2} p^+ x^- + \frac{1}{2} p^- x^+ - \boldsymbol{p}^\perp \cdot \boldsymbol{x}^\perp$, it is easy to see that (x^+, p^-) is a conjugate pair, and similarly (x^-, p^+), $(\boldsymbol{x}^\perp, \boldsymbol{p}^\perp)$. The metric tensor within the light-front parametrization reads,

$$[g_{\mu\nu}] = \begin{pmatrix} g_{++} & g_{+-} & g_{+1} & g_{+2} \\ g_{-+} & g_{--} & g_{-1} & g_{-2} \\ g_{1+} & g_{1-} & g_{11} & g_{12} \\ g_{2+} & g_{2-} & g_{21} & g_{22} \end{pmatrix} = \begin{pmatrix} 0 & +1/2 & 0 & 0 \\ +1/2 & 0 & 0 & 0 \\ 0 & 0 & -1 & 0 \\ 0 & 0 & 0 & -1 \end{pmatrix}. \tag{1.15}$$

Note that the metric tensor is not diagonal, in contrast to that of the usual parametrization.

In light-front dynamics, the quantum state of the system is defined at fixed light-front time x^+, and evolves according to the light-front Schrödinger equation [10],

$$i \frac{\partial}{\partial x^+} |\psi(x^+)\rangle = \frac{1}{2} \hat{P}^- |\psi(x^+)\rangle \tag{1.16}$$

Here P^-, being the conjugate momentum of the light-front time x^+, plays the role of the Hamiltonian in light-front dynamics. The most general quantum field theory problems can

be solved from Eq. (1.16) with appropriate the initial conditions. If the Lagrangian does not explicitly depend on light-front time x^+, as is the typical bound-state problem, Eq. (1.16) can be reduced to the time-independent Schrödinger equation:

$$\frac{1}{2}\hat{P}^-|\psi_h\rangle = P_h^-|\psi_h\rangle. \tag{1.17}$$

Effectively, this is equivalent to diagonalizing the light-front Hamiltonian operator $\hat{P}^-$. In particular, for the self-bound systems, the eigenvalue P_h^- is just the light-front kinematic energy for a free particle. It can be obtained from the light-front dispersion relation:

$$P_\mu P^\mu = M_h^2 \implies P_h^- = \frac{\boldsymbol{P}_\perp^2 + M_h^2}{2P^+}, \tag{1.18}$$

where M_h is the invariant mass of the particle. Note that the light-front dispersion relation strongly resembles that of the non-relativistic dynamics: both are quadratic in terms of the transverse momenta, in contrast to the equal-time dispersion relation. With the help of Eq. (1.18), the time-independent Schrödinger equation can be written as,

$$(P^+\hat{P}^- - \boldsymbol{P}_\perp^2)|\psi_h\rangle = M_h^2|\psi_h\rangle. \tag{1.19}$$

The operator on left-hand side is just $\hat{P}^2 = P^+\hat{P}^- - \boldsymbol{P}_\perp^2$, and Eq. (1.19) is consistent with Eq. (1.10). In the literature, the operator $\hat{P}^2 = P^+\hat{P}^- - \boldsymbol{P}_\perp^2 \equiv \hat{H}_{\rm LC}$ is known as the "light-cone Hamiltonian"[6], although it has the mass squared dimension. Diagonalizing the light-cone Hamiltonian operator directly produces the invariant mass square eigenvalues M_h^2 and the state vectors $|\psi_h\rangle$. Eq. (1.19) will be our starting point for solving bound-state problems.

As we have mentioned, the 10 generators of the Poincaré algebra are also classified into two categories, kinematical and dynamical. Rewritten in terms of light-front parametrization, the kinematical generators are [6, 8, 9, 10, 11, 12],

$$\left\{P^+, \quad \boldsymbol{P}^\perp, \quad E^- \equiv \frac{1}{2}M^{+-} = K^3, \quad E^i \equiv M^{+i} = K^i + \epsilon^{ij}J^j, \quad F^- \equiv M^{12} = J^3\right\}, \tag{1.20}$$

where $i = 1, 2$, $j = 1, 2$, $\epsilon^{12} = -\epsilon^{21} = 1$, $\epsilon^{11} = \epsilon^{22} = 0$. Note that the paired repeating transverse coordinate indices are also summed over. The kinematical nature of P^+ and $\boldsymbol{P}^\perp$ also justifies our notation in Eq. (1.19), as the eigenvalues of these operators can be directly obtained, e.g.,

[6] In the literature, it is also known as the "mass squared operator".

by choosing the momentum basis, without actual diagonalization. The dynamical generators are [6, 8, 9, 10, 11, 12],

$$\Big\{P^-, \quad F^i \equiv \epsilon^{ij} J^{j-} = J^i + \epsilon^{ij} K^j \Big\}, \quad (i,j=1,2). \tag{1.21}$$

$(E^-, \boldsymbol{E}^\perp)$ form a closed algebra and they are sometimes referred to as the generators of the "light-front boosts". Similarly, $(F^-, \boldsymbol{F}^\perp)$ also form a closed algebra and they are sometimes called the generators of "light-front rotations"[7].

We can express the spin operators $\boldsymbol{\mathcal{J}}$ in terms of these operators:

$$\begin{aligned} \mathcal{J}^3 =& J^3 + \frac{1}{P^+}(E^1 P^2 - E^2 P^1), \\ \mathcal{J}^i =& \frac{1}{m}\big[P^+ F^i + \mathcal{J}^3 P^i\big] - \frac{1}{m}\epsilon^{ij}\big[P^- E^j + K^3 P^j\big]. \end{aligned} \tag{1.22}$$

As we can see, the transverse spins $\boldsymbol{\mathcal{J}}^\perp = (\mathcal{J}^1, \mathcal{J}^2)$ is dynamical, while $\mathcal{J}^3$ is kinematical. As a result, the total spin $\boldsymbol{\mathcal{J}}^2 = \boldsymbol{\mathcal{J}}_\perp^2 + \mathcal{J}_3^2$ is also a dynamical operator. In principle, Eq. (1.11) has to be simultaneously diagonalized with Eq. (1.5) to obtain the spin j of the particle. In practice, however, it is more convenient to infer j from indirect methods, as it is only an integer or a half integer. These techniques will be discussed later.

1.4 Light-Front Quantization

The interaction of QCD is conventionally introduced through the Yang-Mills Lagrangian density [18],

$$\mathscr{L}_{\rm YM} = -\frac{1}{4} F^{\mu\nu a} F_{\mu\nu a} + \overline{\psi}(i\gamma_\mu D^\mu - m)\psi \tag{1.23}$$

where $a = 1, 2, \cdots, 8$ is the color index. Contraction of repeating Lorentz indices $\mu, \nu = 0, 1, 2, 3$ (including the purely transverse indices $i = 1, 2$) and color indices $a, b, c, d, e = 1, 2, \cdots, 8$ is understood. $D^\mu = \partial^\mu - i g_s A^{\mu a} T^a$ is the covariant derivative, g_s the strong interaction coupling. T^a are the generators of a SU(3) Lie group for color, commonly expressed in terms of the Gell-Mann matrices. The fields A and ψ describe the gluon and the quark degrees of freedom, respectively. We have suppressed the quark flavor indices for simplicity. $F^{\mu\nu a} \equiv$

[7] This is a legacy name and should not be taken literally, as clearly $< F^-, F^1, F^2 > \not\simeq \mathfrak{su}_2$. In fact, $(F^-, \boldsymbol{F}^\perp)$ generate rotations around the lightcone.

$\partial^\mu A^{\nu a} - \partial^\nu A^{\mu a} + g_s f^{abc} A^{\mu b} A^{\nu c}$, f^{abc} is the structure constant of the $\mathfrak{su}_3$ Lie algebra, namely, $[T^a, T^b] = i f^{abc} T^c$. It is convenient to introduce the strong interaction fine structure constant $\alpha_s \equiv g_s^2/(4\pi)$, which is more popular than g_s, and is often referred to as the strong interaction coupling.

In order to obtain the Hamiltonian, we should first identify the canonical variables, the generalized coordinates $\Psi^i(x)$ and generalized momenta $\Pi_i(x)$. By analogy to equal-time quantization [7], the canonical momenta $\Pi_i(x)$ are defined as,

$$\Pi_i(x) \equiv \frac{\delta L}{\delta \partial_+ \Psi^i(x)}, \qquad \partial_+ \Pi_i(x) \equiv \frac{\delta L}{\delta \Psi^i(x)}, \tag{1.24}$$

where $\partial_+ = \partial/\partial x^+$, $\delta/\delta f(x^-, \boldsymbol{x}^\perp)$ represents the functional derivative with respect to a spatial function $f(x^-, \boldsymbol{x}^\perp)$, and L is the Lagrangian,

$$L(x^+) \equiv \int \mathrm{d}^4x\, \delta(x^+ - y^+) \mathscr{L}(\Psi^i(y), \partial_+ \Psi^i(y)). \tag{1.25}$$

Note that the identified canonical variables $\Psi^i(x)$ and $\Pi_i(x)$ should satisfy the appropriate commutation relations on the equal light-front time sheets. Then, the Hamiltonian can be obtained from the standard Legendre transformation,

$$P^-(x^+) = 2 \sum_i \int \mathrm{d}^4y\, \delta(x^+ - y^+) \Big[\Pi_i(y) \partial_+ \Psi^i(y) - \mathscr{L}\big(\Psi^i(y), \partial_+ \Psi^i(y)\big) \Big]. \tag{1.26}$$

It is understood that the time derivative terms $\partial_+ \Psi^i(y)$ should be expressed in terms of the canonical variables through the equation of motion (1.24).

It is tempting to identify the field contents (for example, $A^{\mu a}$ and ψ for QCD) and their time derivatives as the canonical variables $\Psi^i(x)$ and $\Pi_i(x)$. This may be the case for simple field theories in the equal-time quantization. However, quantization on the light front often introduces constraints which complicate the theory. To illustrate the point, let us consider a scalar theory (Klein-Gordon):

$$\mathscr{L} = \frac{1}{2} \partial_\mu \varphi \partial^\mu \varphi - \frac{1}{2} m^2 \varphi^2 = \partial_+ \varphi \partial^+ \varphi - \frac{1}{2} \boldsymbol{\partial}^\perp \varphi \cdot \boldsymbol{\partial}^\perp \varphi - \frac{1}{2} m^2 \varphi^2. \tag{1.27}$$

The canonical momentum conjugate to φ is,

$$\pi(x) = \frac{\partial \mathscr{L}}{\partial \partial_+ \varphi} = \partial^+ \varphi, \tag{1.28}$$

where $\partial^+\varphi \equiv 2\frac{\partial}{\partial x^-}\varphi$ contains no time derivative term $\partial_+\varphi$. Therefore, Eq. (1.28) introduces a constraint for π and φ: $\pi(x) - \partial^+\varphi(x) = 0$.

The standard procedures to handle the quantization of a constrained system are due to Dirac [19, 20] (see also, [21, 22, 23]) and Schwinger [24, 25]. Another complication of QCD is the gauge redundancy associated with the local gauge symmetry. Fields related by gauge transformations represent the same physical degree of freedom. This redundancy can be removed by choosing a particular gauge. This gauge fixing condition, again, can be viewed as a constraint and handled accordingly. In light-front quantization, the most convenient gauge choice is the light-cone gauge [26]:

$$A^+ \equiv A^0 + A^3 = 0. \tag{1.29}$$

The light-front quantized QED (LFQED) Hamiltonian within the light-cone gauge reads [27, 28, 29],

$$\begin{aligned} \hat{P}^-_{\rm LFQED} = \int \mathrm{d}x^- \mathrm{d}^2x^\perp \Bigg[& \frac{1}{2}\,\overline{\psi}\gamma^+ \frac{(i\partial^\perp)^2 + m^2}{i\partial^+}\psi - \frac{1}{2}A^i(i\partial^\perp)^2 A^i \\ & + e\,\overline{\psi}\gamma_\mu A^\mu \psi + \frac{e^2}{2}\,\overline{\psi}\gamma_\mu A^\mu \frac{\gamma^+}{i\partial^+}\Big(\gamma_\nu A^\nu \psi\Big) + \frac{e^2}{2}\,\overline{\psi}\gamma^+\psi\frac{1}{(i\partial^+)^2}\Big(\overline{\psi}\gamma^+\psi\Big)\Bigg], \end{aligned} \tag{1.30}$$

where $\gamma^+ = \gamma^0 + \gamma^3$, $1/\partial^+$ and $1/(\partial^+)^2$ are the inverse of the respective derivatives, resulted from solving constraint equations (see Appendix A). The first two terms are the kinetic energies. The third term is the familiar QED vertex. The rest two terms are new to LFQED, called the instantaneous terms, also known as the contact terms. The dynamical degrees of freedom are $\psi_+(x) \equiv \frac{1}{2}\gamma^0\gamma^+\psi(x)$ and $A^i(x)$, and their canonical momenta are $i\psi^\dagger_+(x)$ and ∂^+A^i, respectively. The canonical commutation relations are,

$$\begin{aligned} \Big\{\psi_+(x), i\psi^\dagger_+(y)\Big\}_{x^+=y^+} &= \frac{1}{2}\gamma^0\gamma^+ i\delta(x^- - y^-)\delta^2(\boldsymbol{x}^\perp - \boldsymbol{y}^\perp) \\ \Big[A^i(x), \partial^+_y A^j(y)\Big]_{x^+=y^+} &= i\delta(x^- - y^-)\delta^2(\boldsymbol{x}^\perp - \boldsymbol{y}^\perp)\delta_{ij}. \end{aligned} \tag{1.31}$$

The remaining field components are constrained degrees of freedom, and can be obtained from the constraint equations derived from the equations of motion. It is heuristic to represent the interaction vertices by vertex diagrams, as shown in Fig. 1.2.

Similarly, the light-front quantized QCD (LFQCD) Hamiltonian within the light-cone gauge

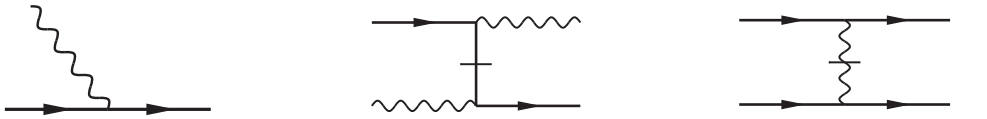

(a) $e\,\overline{\psi}\gamma_\mu A^\mu\psi$ (b) $\frac{e^2}{2}\overline{\psi}\gamma_\mu A^\mu\frac{\gamma^+}{i\partial^+}\gamma_\nu A^\nu\psi$ (c) $\frac{e^2}{2}\,\overline{\psi}\gamma^+\psi\frac{1}{(i\partial^+)^2}\overline{\psi}\gamma^+\psi$

Figure 1.2: Vertex diagrams associated with the LFQED Hamiltonian. The solid lines represent the fermion operators. The wavy lines represent the photon operators. The "instantaneous propagators" $1/(i\partial^+)$ and $1/(i\partial^+)^2$ are represented by lines with a bar across them.

is [30, 31, 32],

$$\begin{aligned}\hat{P}^-_{\rm LFQCD} = \int {\rm d}x^-{\rm d}^2x^\perp\,\Big[&\frac{1}{2}\,\overline{\psi}\gamma^+\frac{(i\partial^\perp)^2+m^2}{i\partial^+}\psi-\frac{1}{2}A^{ia}(i\partial^\perp)^2A^{ia}\\&+g_s\,\overline{\psi}\gamma_\mu A^{\mu a}T^a\psi+\frac{g_s^2}{2}\,\overline{\psi}\gamma_\mu A^{\mu a}T^a\frac{\gamma^+}{i\partial^+}\Big(\gamma_\nu A^{\nu b}T^b\psi\Big)+\frac{g_s^2}{2}\,\overline{\psi}\gamma^+T^a\psi\frac{1}{(i\partial^+)^2}\Big(\overline{\psi}\gamma^+T^a\psi\Big)\\&-g_s^2\,if^{abc}\,\overline{\psi}\gamma^+T^c\psi\frac{1}{(i\partial^+)^2}\Big(i\partial^+A^{\mu a}A^b_\mu\Big)+g_s\,if^{abc}\,i\partial^\mu A^{\nu a}A^b_\mu A^c_\nu\\&+\frac{g_s^2}{2}\,if^{abc}\,if^{ade}\,i\partial^+A^{\mu b}A^c_\mu\frac{1}{(i\partial^+)^2}\Big(i\partial^+A^{\nu d}A^e_\nu\Big)-\frac{g_s^2}{4}\,if^{abc}\,if^{ade}A^{\mu b}A^{\nu c}A^d_\mu A^e_\nu\Big].\end{aligned}\tag{1.32}$$

Here again the instantaneous terms appear along with the standard QCD vertices. Note also that LFQCD Hamiltonian contains no ghost, a feature shared among the axial gauges [18]. The identification of canonical variables are similar to QED, except for additional color indices[8], and the canonical commutation relations are,

$$\begin{aligned}\Big\{\psi_{i+}(x),i\psi^\dagger_{j+}(y)\Big\}_{x^+=y^+}&=\frac{1}{2}\gamma^0\gamma^+i\delta(x^--y^-)\delta^2(\boldsymbol{x}^\perp-\boldsymbol{y}^\perp)\delta_{ij},\quad(i,j=1,2,3)\\\Big[A^{ia}(x),\partial^+_yA^{jb}(y)\Big]_{x^+=y^+}&=i\delta(x^--y^-)\delta^2(\boldsymbol{x}^\perp-\boldsymbol{y}^\perp)\delta_{ab}.\quad(a,b=1,2,\cdots8)\end{aligned}\tag{1.33}$$

The vertex diagrams for LFQCD interactions are shown in Fig. 1.3.

At initial time $x^+=0$, the fields admit free-field expansions [10],

$$\psi_i(x)=\sum_{s=\pm\frac{1}{2}}\int\frac{{\rm d}^2\boldsymbol{p}^\perp{\rm d}p^+}{(2\pi)^32p^+}\vartheta(p^+)\Big[b_{si}(p)u_s(p)e^{-ip\cdot x}+d^\dagger_{si}(p)v_s(p)e^{+ip\cdot x}\Big],\tag{1.34}$$

$$A^{\mu a}(x)=\sum_{\lambda=\pm}\int\frac{{\rm d}^2\boldsymbol{k}^\perp{\rm d}k^+}{(2\pi)^32k^+}\vartheta(k^+)\Big[a_{\lambda a}(k)\varepsilon^\mu_\lambda(k)e^{-{\rm i}k\cdot x}+a^\dagger_{\lambda a}(k)\varepsilon^{\mu*}_\lambda(k)e^{+ik\cdot x}\Big],\tag{1.35}$$

where $\vartheta(z)$ is the Heaviside unit step function. Definitions of the Dirac spinors $u_s(p)$, $v_s(p)$ and the polarization vector $\varepsilon^\mu_\lambda(k)$ are detailed in Appendix A with various useful identities included.

[8]Quarks, anti-quarks and gluons carry color indices: ψ_i $(i=1,2,3)$ and $A^{\mu c}$ $(c=1,2,\cdots,8)$. We have suppressed the quark and anti-quark color indices in Eq. (1.32).

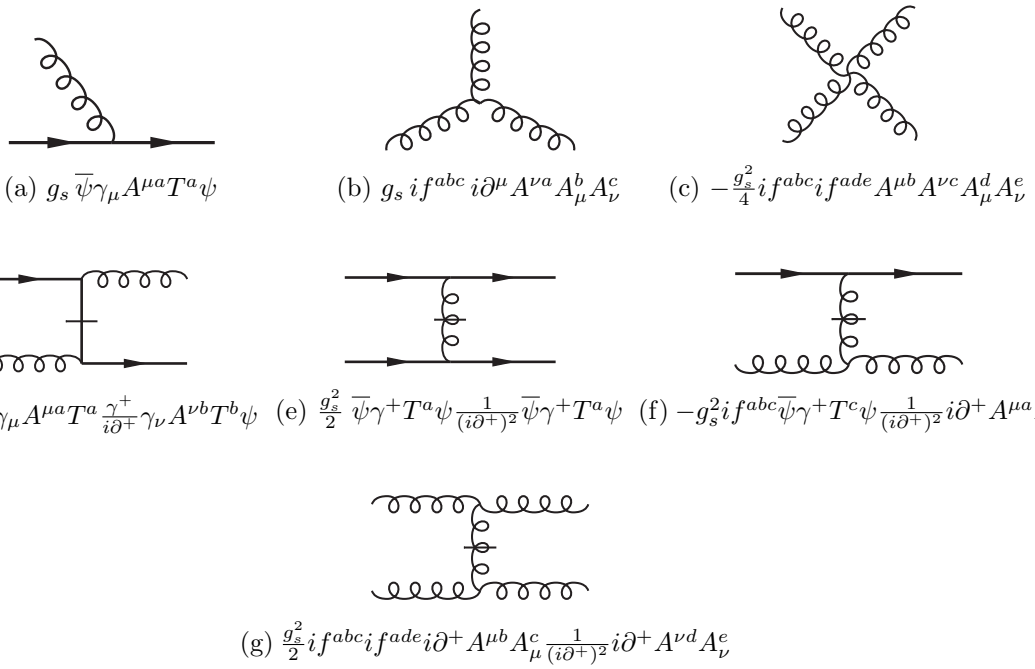

(a) $g_s\,\overline{\psi}\gamma_\mu A^{\mu a}T^a\psi$ (b) $g_s\,if^{abc}\,i\partial^\mu A^{\nu a}A^b_\mu A^c_\nu$ (c) $-\frac{g_s^2}{4}if^{abc}if^{ade}A^{\mu b}A^{\nu c}A^d_\mu A^e_\nu$

(d) $\frac{g_s^2}{2}\overline{\psi}\gamma_\mu A^{\mu a}T^a\frac{\gamma^+}{i\partial^+}\gamma_\nu A^{\nu b}T^b\psi$ (e) $\frac{g_s^2}{2}\,\overline{\psi}\gamma^+T^a\psi\frac{1}{(i\partial^+)^2}\overline{\psi}\gamma^+T^a\psi$ (f) $-g_s^2if^{abc}\overline{\psi}\gamma^+T^c\psi\frac{1}{(i\partial^+)^2}i\partial^+A^{\mu a}A^b_\mu$

(g) $\frac{g_s^2}{2}if^{abc}if^{ade}i\partial^+A^{\mu b}A^c_\mu\frac{1}{(i\partial^+)^2}i\partial^+A^{\nu d}A^e_\nu$

Figure 1.3: Vertex diagrams associated with the LFQCD Hamiltonian. The solid lines represent the quark operators. The curly lines represent the gluon operators. The "instantaneous propagators" $1/(i\partial^+)$ and $1/(i\partial^+)^2$ are represented by lines with a bar across it.

The creation and annihilation operators satisfy the canonical commutation relations,

$$\begin{aligned}\left[a_{\lambda a}(k),a^\dagger_{\lambda' b}(k')\right] =&2k^+\vartheta(k^+)(2\pi)^3\delta^3(k-k')\delta_{\lambda\lambda'}\delta_{ab},\\ \left\{b_{si}(p),b^\dagger_{s'j}(p')\right\} =&2p^+\vartheta(p^+)(2\pi)^3\delta^3(p-p')\delta_{ss'}\delta_{ij},\\ \left\{d_{si}(p),d^\dagger_{s'j}(p')\right\} =&2p^+\vartheta(p^+)(2\pi)^3\delta^3(p-p')\delta_{ss'}\delta_{ij},\end{aligned}\tag{1.36}$$

where $\delta^3(k-k')=\delta(k^+-k'^+)\delta^2(k^\perp-k'^\perp)$.

1.5 Fock Space Representation

Fock states can be defined in terms of the eigenstates of the free-field Hamiltonian, i.e., the light-front kinetic operator, and can be obtained by applying the creation operators on the Fock vacuum $|0\rangle$. Representing the full Hamiltonian and its eigenstates in the Fock states is especially convenient in light-front dynamics, because it has the maximal number of kinematical operators. In particular, all boost operators $(E^-,\boldsymbol{E}^\perp)$ are kinematical. As a result, different Fock sectors do not mix under the boost transformations. The expansion of a physical state

$|h(P,j,m_j)\rangle$ of a hadron h in the Fock space reads,

$$|h(P,j,m_j)\rangle = \sum_{n=0}^{\infty}\prod_{i=1}^{n}\sum_{\sigma_i}\int \frac{\mathrm{d}k_i^+\mathrm{d}^2\boldsymbol{k}_i^\perp}{(2\pi)^3 2k_i^+}\vartheta(k_i^+)\; 2P^+\vartheta(P^+)(2\pi)^3\delta^3(k_1+k_2+\cdots k_n-P)$$
$$\times\,\psi_{h/n}^{\sigma_1,\cdots,\sigma_n}(k_1,k_2,\cdots,k_n;P,j,m_j)\times a_{\sigma_1}^\dagger(k_1)\cdots a_{\sigma_n}^\dagger(k_n)\,|0\rangle\,. \quad (1.37)$$

Here $a_\sigma^\dagger(k)$ is the creation operator for the appropriate constituents (quark, anti-quark or gluon, determined by symmetry), k is the momentum, and $k^2=m_q^2$ for quarks and $k^2=\mu_g^2$ for gluons (normally equals to zero), σ is the spin projection of the particle. The Dirac deltas, $\delta^3(k-k')\equiv\delta(k^+-k'^+)\delta^2(\boldsymbol{k}^\perp-\boldsymbol{k}'^\perp)$, come from the light-front 3-momentum conservation.

The coefficients $\psi_{h/n}$, are the projection of the physical state to the Fock states,

$$S_n\times 2P^+\vartheta(P^+)(2\pi)^3\delta^3(k_1+k_2+\cdots k_n-P)\psi_{h/n}^{\sigma_1,\cdots,\sigma_n}(k_1,k_2,\cdots,k_n;P,j,m_j)$$
$$=\langle 0|a_{\sigma_n}(k_n)\cdots a_{\sigma_1}(k_1)|h(P,j,m_j)\rangle, \quad (1.38)$$

called the light-front wavefunctions (LFWFs). S_n is the appropriate symmetry factor resulted from the identical particle statistics. For example, for an n-boson Fock state, $S_n=1/n!$. LFWFs are invariant under the boost transformations. This is a major distinction between the LFWFs and the wavefunctions in the usual equal time formulation. This distinction comes from the kinematical nature of the light-front boost operators. As a result, the LFWFs can be expressed in terms of the boost-invariant variables,

$$x_i\equiv\frac{k_i^+}{P^+},\quad \boldsymbol{\kappa}_i^\perp\equiv\boldsymbol{k}_i^\perp-x_i\boldsymbol{P}^\perp, \quad (1.39)$$

which is equivalent to evaluating the LFWFs in a special reference frame where $P^+=1$, $\boldsymbol{P}^\perp=0$. x_i are known as the momentum fractions, $\boldsymbol{\kappa}_i$ the relative momenta. Noting $k_i^+\geq 0$, the light-front 3-momentum conservation implies,

$$0\leq x_i\leq 1,\quad \sum_{i=1}^{n}x_i=1,\quad \sum_{i=1}^{n}\boldsymbol{\kappa}_i^\perp=0. \quad (1.40)$$

Then, the LFWFs then can be written as,

$$\psi_{h/n}^{\sigma_1,\cdots,\sigma_n}(k_1,k_2,\cdots,k_n;P,j,m_j)\equiv\varphi_{h/n}^{\sigma_1,\cdots,\sigma_n}(\boldsymbol{\kappa}_1,x_1,\boldsymbol{\kappa}_2,x_2,\cdots,\boldsymbol{\kappa}_n,x_n;P^2,j,m_j), \quad (1.41)$$

without the explicit dependence on P^+ or $\boldsymbol{P}^\perp$.

The physical state $|h(P,j,m_j)\rangle$ is normalized as (cf. Eq. 1.36),

$$\langle h(P',j',m'_{j'})|h(P,j,m_j)\rangle = 2P^+\vartheta(P^+)(2\pi)^3\delta^3(P-P')\delta_{jj'}\delta_{m_jm'_{j'}}. \tag{1.42}$$

Then the normalization of the LFWFs reads,

$$\sum_{n=0}^{\infty} S_n \prod_{i=1}^{n}\sum_{\sigma_i}\int \frac{\mathrm{d}k_i^+\mathrm{d}^2\boldsymbol{k}_i^\perp}{(2\pi)^3 2k_i^+}\vartheta(k_i^+)\; 2P^+\vartheta(P^+)(2\pi)^3\delta^3(k_1+k_2+\cdots k_n-P)$$
$$\times\left|\psi_{h/n}^{\sigma_1,\cdots,\sigma_n}(k_1,k_2,\cdots,k_n;P,j,m_j)\right|^2 = 1. \tag{1.43}$$

Using the boost-invariant momenta, the normalization of the LFWFs can be written as,

$$\sum_{n=0}^{\infty} S_n \prod_{i=1}^{n}\sum_{\sigma_i}\int_0^1 \frac{\mathrm{d}x_i}{2x_i}\int \frac{\mathrm{d}^2\boldsymbol{\kappa}_i^\perp}{(2\pi)^3}\,(2\pi)^3\delta^2(\boldsymbol{\kappa}_1+\boldsymbol{\kappa}_2+\cdots+\boldsymbol{\kappa}_n)\delta(x_1+x_2+\cdots+x_n-1)$$
$$\times\left|\varphi_{h/n}^{\sigma_1,\cdots,\sigma_n}(\boldsymbol{\kappa}_1,x_1,\boldsymbol{\kappa}_2,x_2,\cdots,\boldsymbol{\kappa}_n,x_n;P^2,j,m_j)\right|^2 = 1. \tag{1.44}$$

The diagrammatic representation plays an important role in quantum field theory. The light-front graphical rules are based on the old-fashioned perturbation diagrams, first introduced by Weinberg [33] (see also [10, 11, 27, 34] for more details). These rules are essentially the diagrammatic interpretation of the vertices of the light-front Hamiltonian. They can be easily generalized to the non-perturbative case for Eq. (1.19) by introducing the vertex functions[9],

$$\Gamma_{n/h}^{\sigma_1,\cdots,\sigma_n}(k_1,k_2,\cdots,k_n;P,j,m_j) \equiv (s_n-M^2)\psi_{n/h}^{\sigma_1,\cdots,\sigma_n}(k_1,k_2,\cdots,k_n;P,j,m_j), \tag{1.45}$$

where $s_n \equiv (k_1+k_2+\cdots+k_n)^2 = \sum_{i=1}^n \frac{\boldsymbol{k}_\perp^2+m_i^2}{x_i}$. The graphical rules for the vertex functions can be found in detail in Ref. [34].

1.6 Non-Perturbative Methods

In Fock space, Eq. (1.19) becomes a matrix eigenvalue problem, and the non-perturbative dynamics can be generated by the numerical diagonalization, e.g., QR algorithm, the Lanczos algorithm. However, the Fock space consists of infinite numbers of particles and the resulting Hamiltonian matrix is infinite-dimensional. In practice, the Hamiltonian matrix has to be

[9] In the definition of the vertex functions, it is also popular to factorize out the spin vectors. For example, for a physical electron $|e_{\rm ph}\rangle$ in the $|e\gamma\rangle$ sector, $\varepsilon_\mu^{\lambda *}(k)\bar{u}_s(p)\Gamma_2^\mu(k,p;P)u_\sigma(P) \equiv (s_2-M^2)\psi_2^{s\lambda}(k,p;P,\frac{1}{2},\sigma)$. See, e.g., [35], for more concrete examples.

made finite-dimensional to apply the numerical procedures. One then assesses convergence by a systematic investigation of the numerical results with increasing matrix dimension. This is the *ab initio* Hamiltonian approach to QFT. In this section, we summarize several non-perturbative methods that implement the *ab initio* Hamiltonian approach. Closely related methods include the Transverse Lattice approach [71, 72] and the Light-Front Coupled Cluster method [73]. An overview of the non-perturbative methods can be found in Ref. [17].

1.6.1 Light-Front Tamm-Dancoff coupled integral equations

Combining the free-field expansion Eq. (1.34) and the Fock space representation Eq. (1.37), the eigenvalue equation Eq. (1.19) becomes an infinite set of coupled integral equations for the light-front wavefunctions. The Light-Front Tamm-Dancoff approach imposes a Fock sector truncation, i.e., keeping only states with up to finite number of Fock constituents [36].

While at first sight this method seems to be the reincarnation of the original Tamm-Dancoff approach [37, 38] within light-front quantization, several extraordinary features of light-front dynamics, however, make the light-front Tamm-Dancoff approach distinct. The crucial difference is that the light-front vacuum is trivial[10], and is just the Fock vacuum. To see this, just note that,

$$k_a^+ = E_k + k_z = \sqrt{m_a^2 + \boldsymbol{k}_\perp^2 + k_z^2} + k_z > 0 \implies \sum_a k_a^+ > 0, \tag{1.46}$$

whereas the longitudinal momentum of the vacuum, by definition, is vanishing: $P^+_{\rm VAC} = 0$. Therefore, due to the conservation of the longitudinal momentum, the physical vacuum cannot contain any Fock space particles and it just the Fock vacuum $|0\rangle$. The simplicity of the vacuum is in sharp contrast to the complicated vacuum in equal-time quantization. In practical terms, the disconnected diagrams that dominate the amplitudes in equal-time quantization[11] do not contribute in light-front dynamics. The kinematical nature of boost transformations and the similarity of light-front dynamics to non-relativistic many-body problem also bring major computational advantages.

[10] We do not consider the so-called zero modes, which consist of excitations with $k_a^+ = 0$. We take the view that the zero modes can be regularized, and their contributions can be taken into account by a proper renormalization. For more on this topic, see Ref. [10] and the references therein.

[11] In the time-dependent perturbation theory, these "vacuum bubbles" can be analytically dealt with using Gell-Mann and Low theorem [39].

Of course, ultimately, the justification of the Fock sector truncation should come from the physics of QCD, i.e., whether the state vector of the bound state is dominated by low-lying Fock sectors. The successes of the constituent quark model and the parton model seem to support the Fock sector truncation as a reasonable approximation [40].

The obtained Light-Front Tamm-Dancoff coupled integral equations can be solved numerically. The continuum limit can be reached by extrapolating results from successive Fock sector truncations. The main advantage of this method is that it is analytically tractable. The main disadvantage of this method is that getting mass eigenvalues and light-front wavefunctions of states beyond the lowest states is numerically challenging. In Chapter 3, we will use the Light-Front Tamm-Dancoff coupled integral equation approach to solve the scalar Yukawa model in the single-particle (charge-one) sector.

1.6.2 Discretized Light-Cone Quantization

The Discretized Light-Cone Quantization (DLCQ) method seeks to diagonalize the Hamiltonian matrix in a finite-dimensional discretized momentum basis [41, 42]. The discretization is achieved by imposing periodic or anti-periodic boundary condition in a box in the coordinate space: $-L \leq x^- \leq L$, $-L_\perp \leq x, y \leq L_\perp$. For the cubic interactions, such as Yukawa, QED and QCD, the periodic boundary condition is applied to bosons and anti-periodic boundary condition to fermions. Then the momenta are discretized $k^+ = \frac{2\pi j}{L}$, $k^\perp = (\frac{2\pi n_x}{L_\perp}, \frac{2\pi n_y}{L_\perp})$, where j, n_x, n_y are (half-)integers for (anti-)periodic boundary conditions. As the Hamiltonian is block diagonal in terms of P^+, we can fix its value $P^+ \equiv \frac{2\pi K}{L}$, and the longitudinal momentum conservation implies, for each Fock sector,

$$\sum_a k_a^+ = P^+ \quad \Longrightarrow \quad \sum_a j_a = K. \tag{1.47}$$

Thanks to light-front boost invariance, the light-cone Hamiltonian $H_{\rm LC}$ and the LFWFs only depend on the momentum fractions $x \equiv \frac{k^+}{P^+} = \frac{j}{K}$ in the longitudinal direction, hence are independent to L. Therefore, K represents the resolution of the system in the longitudinal direction. The positivity of the longitudinal momentum k^+ and the longitudinal momentum conservation Eq. (1.47) limits the value of j to $0 < j < K$. As such, the finite resolution

K imposes a natural restriction on the number of particles allowed in the basis space. In the transverse direction, a cutoff Λ is imposed to regularize the transverse momenta through $m_i^2+p_{i\perp}^2 \leq x_i\Lambda^2$, which in turn restricts the transverse quantum numbers $-N_\perp \leq n_x, n_y \leq N_\perp$.

The resulting basis space is finite. In practice, Fock sector truncation is also used to reduce the number of particles, which renders the DLCQ approach as a variation of the Light-Front Tamm-Dancoff approach. The obtained Hamiltonian matrix can be diagonalized numerically. The continuum limit is achieved by taking $L \to \infty, L_\perp \to \infty, \Lambda \to \infty$. For any finite P^+, $L \to \infty$ also implies $K \to \infty$. The DLCQ approach has been fruitful in addressing non-perturbative quantum field theories [43], and in particular in 1+1 dimensions. It has also been introduced to string theory [44, 45].

1.6.3 Basis Light-Front Quantization

Basis Light-Front Quantization (BLFQ) is another matrix diagonalization approach similar to DLCQ [46]. It generalizes the discretized momentum basis to arbitrary basis subject to completeness and orthogonality. The flexibility in the choice of basis allows one to preserve the kinematic symmetries, and take advantage of the development of the semi-analytic approximation to QCD.

A typical choice of basis is the harmonic oscillator basis in the transverse direction and discretized momentum basis in the longitudinal direction [47, 48]. This basis preserves the rotational symmetry in the transverse plane, allowing the factorization of the center-of-mass motion in the single-particle basis [47, 48], and is also consistent with light-front holographic QCD [49].

The factorization of the center-of-mass motion within the finite basis is a valuable feature, since it provides amplitudes that are functions of purely internal coordinates, thereby providing transverse boost invariance. The center-of-mass excitations can be removed from the low-lying spectrum[12] by using the Lawson method [50]. Note that the factorization of the center-

[12]Removing the center-of-mass excitations from the low-lying spectrum has practical impact in numerical calculations. Diagonalization of large sparse matrices typically relies on iterative procedures, e.g. Lanczos/Arnoldi algorithm [51], with the advantage of exploiting only the lowest states in energy, instead of working with the full eigenspace. Without removing the center-of-mass motion, the low-lying spectrum could be filled with the center-of-mass excitations.

of-mass motion is possible in light-front dynamics because light-front boost transformations are kinematical. Therefore, the BLFQ approach exploits the similarity between light-front dynamics and the non-perturbative quantum many-body theory. Modern many-body methods can be directly applied to the BLFQ studies [52].

One should also note that the (anti-)symmetrization for (fermions) bosons in the relative coordinates could rapidly become intractable as the number of identical particles increases. In the single-particle coordinates, the bookkeeping of (anti-)symmetrization is straightforward in practical numerical calculation.

BLFQ has been applied to a range of non-perturbative problems in QED with success, including the electron anomalous magnetic moment [53, 54], electron generalized parton distribution [55], and positronium [56, 57]. It has also been extended to the time-dependent regime [58] and applied to the study of the non-linear Compton scattering [59]. The BLFQ approach is also the focus of this thesis. In Chapter 2, we will apply this approach to heavy quarkonium system as the first application to QCD bound states [60].

1.6.4 Effective Hamiltonian

One fundamental challenge faced in the Fock space Hamiltonian approaches is the exponential growth of the dimensionality of the Hamiltonian matrix in the many-body sector. For example, in DLCQ the matrix dimension d grows as $d \sim 2^{K-1} \times (2N_\perp)^{2K-2}$, where K and $2N_\perp$ are the resolutions in the longitudinal and transverse directions, respectively. For a modest grid $K = 2N_\perp = 10$, $d \sim 10^{20}$, far beyond the current computational capacity.

The idea of an effective Hamiltonian approach is to construct an effective Hamiltonian operator that acts on a smaller Hilbert space (model space) while preserving the low-lying spectrum [10, 61]. This approach is a well-known tool in quantum many-body theory, in particular, in the *ab initio* nuclear structure calculations [52].

Many methods exist for constructing the effective Hamiltonian and can be roughly divided into two categories. The standard effective Hamiltonian schemes employs a block transformation of the Hamiltonian operator such that the low-lying states completely decouple from the rest. This can be achieved through either a direct substitution (Bloch-Horowitz [62]) or a

similarity transformation (Bloch [63], Okubo [64], Suzuki-Lee [65]). The similarity transformation scheme for LFQCD within a weak coupling treatment was investigated by Wilson *et al.* [61, 66, 67]. The flow equation scheme evolves the Hamiltonian operator via a renormalization group flow equation [68, 69, 70]. The flow equation softens the far off-diagonal contribution, and the resulting effective Hamiltonian provides an appealing starting point for a few-body constituent model.

Let us illustrate the effective Hamiltonian approach by sketching the Bloch-Horowitz scheme. To solve the light-front eigenvalue problem in a Hilbert space,

$$H_{\rm LC}|\psi_a\rangle = M_a^2|\psi_a\rangle, \tag{1.48}$$

the effective Hamiltonian approach starts with a subspace (called P-space) with the projection operator P associated with it ($P^2 = P$). It is convenient to define another projection operator $Q = 1 - P$ with $Q^2 = Q$, $PQ = QP = 0$. Projecting the eigenvalue equation into the P-space and Q-space respectively:

$$\begin{aligned} PH_{\rm LC}P|\psi_a\rangle + PH_{\rm LC}Q|\psi_a\rangle =& M_a^2 P|\psi_a\rangle \\ QH_{\rm LC}P|\psi_a\rangle + QH_{\rm LC}Q|\psi_a\rangle =& M_a^2 Q|\psi_a\rangle \end{aligned} \tag{1.49}$$

Solve $Q|\psi_a\rangle$ from the second equation and substitute it to the first one, we get,

$$\left[PH_{\rm LC}P + PH_{\rm LC}Q(M_a^2 - QH_{\rm LC}Q)^{-1}QH_{\rm LC}P\right]|\psi_a\rangle = M_a^2 P|\psi_a\rangle. \tag{1.50}$$

Therefore, one can define an effective Hamiltonian,

$$H_{\rm eff}(\omega) = PH_{\rm LC}P + PH_{\rm LC}Q(\omega - QH_{\rm LC}Q)^{-1}QH_{\rm LC}P, \tag{1.51}$$

where ω is some arbitrary constant. Diagonalizing this effective Hamiltonian gives the mass eigenvalues $M_a^2(\omega)$ and eigenvectors $|\psi_a(\omega)\rangle$. The physical solutions can be found from solving the fix-point equation,

$$M_a^2(\omega) = \omega. \tag{1.52}$$

It should be pointed out that the effective Hamiltonian approach is often used in combination with other methods, e.g., Fock sector truncation (Light-Front Tamm-Dancoff approxi-

mation), including also a perturbative expansion[13]. For example, in the Bloch-Horowitz effective Hamiltonian, we have to invert the operator $\omega - QHQ$ to obtain the Q-space resolvent $G(\omega) \equiv (\omega - QHQ)^{-1}$, which is probably as hard as diagonalizing the full Hamiltonian. To proceed, we can rewrite H into the free part and the interacting part: $H = T + V$, and define the free resolvent $G_0(\omega) = (\omega - QH_0Q)^{-1}$. Then, G and G_0 satisfies the usually Lippmann-Schwinger equation for Green's function,

$$G = G_0 + G_0VG = G_0 + G_0VG_0 + G_0VG_0VG_0 + \cdots \tag{1.53}$$

The second equality is an iterative solution of the resolvent G. If V is small comparing to T, we can keep only the leading order term and the Bloch-Horowitz effective Hamiltonian becomes,

$$PH_{\rm LC}P + PH_{\rm LC}Q(\omega - QT_{\rm LC}Q)^{-1}QH_{\rm LC}P + \mathcal{O}(V^2). \tag{1.54}$$

Note that $QT_{\rm LC}Q$ is diagonal in the momentum basis.

1.7 Motivation and Outline

We identify that the main advantages of the light-front quantum field theory are the simplicity of the dynamics and vacuum structure, and its similarity to the non-relativistic quantum many-body problems. These advantages make it ideal to adopt the Hamiltonian formalism to study the relativistic bound-state problem, in particular, hadrons. With the Fock sector expansion, the problem is further turned into the many-body dynamics.

Based on these observations and the experience in other non-perturbative approaches, such as Lattice QCD and the *ab initio* nuclear structure calculations, our main motivation is to develop computational frameworks for solving the Light-Front QCD eigenvalue equation 1.19. Our present work will serve as benchmarks for future extensions that will address more realistic and more difficult aspects of QCD, though the current studies also have values in their own rights within the current development of hadron physics.

With this motivation, we study heavy quarkonium in Chapter 2 as the first QCD application of Basis Light-Front Quantization. We adopt the effective Hamiltonian approach, with an

[13] As pointed out before, the bound state problem is always non-perturbative, even if the coupling constant is not large.

effective one-gluon exchange interaction and a confining interaction coming from the Light-Front Holographic QCD. We solve the effective Hamiltonian eigenvalue problem within the BLFQ approach and obtain the spectroscopy. We also calculate several hadronic observables relevant for understanding the structures of the system.

We study the non-perturbative renormalization of the scalar Yukawa model in Chapter 3. We adopt a systematic renormalization scheme and solve the problem with a Fock sector expansion up to four constituent particles. The properly renormalized eigenvalue equation yields a set of coupled integral equations and it is solved using a numerical procedure. We calculate the form factor and compare the results from successive Fock sector truncations, which allows us to assess the convergence of the Fock sector expansion.

We conclude in Chapter 4.

As is mentioned, this thesis is based on the research work done by the author and collaborators [48, 47, 56, 57, 152, 153, 163, 60]. The remainder of this subsection summarizes the author's main contributions.

The author developed the analytic expression and the numerical algorithm for calculating the Talmi-Moshinsky coefficients for the harmonic oscillator basis within the holographic variables [47]. The author provided an independent derivation of the expressions used in the positronium project [56]. The author also developed and tested components of the codes for calculating the matrix elements [56].

For the scalar Yukawa model [152, 153, 163], the author cross-checked all analytic expressions. The author also proposed the analytic method to isolate and cancel the mass pole, which turned out to be critical for obtaining reliable numerical results for the problem. The author wrote independent codes to cross-check the numerical results. The author also wrote the codes for calculating the form factors. As the lead author, the author drafted the manuscript and oversaw the publication process.

The author carried out the derivation for the analytic work in the quarkonium project [60]. The author developed and tested the numerical codes, and analyzed the results. The author also drafted the manuscript and oversaw the publication process.

CHAPTER 2. BASIS LIGHT-FRONT QUANTIZATION APPROACH TO HEAVY QUARKONIUM

In this chapter, we study the heavy quarkonium in the Basis Light-Front Quantization Approach. Heavy quarkonium is the bound-state system of heavy quark-anti-quark ($q\bar{q}$) pair. It is an ideal laboratory for studying the interplay between perturbative and non-perturbative QCD [74]. The measurement of heavy quarkonium decay widths are useful for constraining Standard Model parameters. Experimental facilities, such as Belle, CLEO and LHC, have produced extensive data on heavy quarkonium.

Many theoretical tools have been developed to address the heavy quarkonium system, including the non-relativistic potential models [75, 76], non-relativistic QCD [77], heavy quark effective field theory [78], Dyson-Schwinger Equations [79, 80, 81, 82] and Lattice QCD [83]. Within light-front dynamics, several work have appeared [84, 85, 86, 87, 88, 89]. The recent discoveries of exotic states: the tetraquark [90] and the pentaquark [91], have renewed interests in the theoretical investigation of the heavy quarkonium spectroscopy.

The full QCD dynamics of quarkonium is generally believed to be very complicated [92]. In light-front language, a quarkonium state $|\psi_h\rangle$ has various many-body components in Fock space,

$$|\psi_h\rangle = |q\bar{q}\rangle + |q\bar{q}g\rangle + |q\bar{q}q\bar{q}\rangle + |q\bar{q}q\bar{q}g\rangle + \cdots \tag{2.1}$$

Working directly with these many-body dynamics is a formidable task. On the other hand, quarkonium (and hadrons in general) appear to have reasonable first approximations within very simple constituent model. The non-relativistic potential models [75], takes only the $|q\bar{q}\rangle$ sector into account, and the interactions between the quark and anti-quark are assumed to be a confining potential (linear, harmonic or others) plus a Coulomb-like potential. These

simple models turn out to be very successful in predicting the masses, decay widths and other properties of heavy quarkonium [76].

The constituent picture can be realized on the light front without the loss of relativity [61]. Such a path is provided by the effective Hamiltonian approach. The eigenvalue equation for an effective light-front Hamiltonian of two equal-mass (m_f) quarks operating only in the $q\bar{q}$ sector reads,

$$\left(\frac{\boldsymbol{k}_\perp^2 + m_f^2}{x(1-x)} + V_{\rm eff}\right)\psi_h(\boldsymbol{k}_\perp, x) = M_h^2 \psi_h(\boldsymbol{k}_\perp, x). \tag{2.2}$$

The effective interaction $V_{\rm eff}$ thus encodes all non-perturbative dynamics of the theory. The standard way of deriving $V_{\rm eff}$ is through the effective Hamiltonian approach [66], that systematically sums over the higher Fock space contributions. Recently, a remarkable approach was developed by Brodsky and de Téramond to obtain the effective light-front interaction based on the profound correspondence between bulk gravity and LFQCD, known as the Light-Front Holographic QCD [49]. This work provides a first approximation to LFQCD.

We address the heavy quarkonium in an effective Hamiltonian approach. We first adopt a confining interaction inspired by the Light-Front Holographic QCD. We further implement an effective one-gluon exchange interaction [56, 93]. These two pieces of interactions deal with the long- and short-distance physics, respectively. The wavefunctions of the Light-Front Holographic QCD provide a natural orthonormal basis. We therefore adopt this basis and solve the eigenvalue problem of the effective Hamiltonian within the Basis Light-Front Quantization approach. We will compute several important observables for heavy quarkonium: the spectroscopy, the decay constant and the form factors.

For the present study, we will focus on equal-mass systems ($m_q = m_{\bar{q}} \equiv m_f$), specifically, charmonium and bottomonium. Extension to heavy-light systems is in principle straightforward.

2.1 Confinement from Light-Front Holography

Confinement is an essential feature of QCD. In principle, the effective two-body confining potential can be systematically derived from the QCD Hamiltonian [94]. Work along that

line can be seen in Ref. [61, 85, 68, 69, 95] and the references therein. An alternative is the phenomenological approach inspired by, for example, the static potential extracted from Lattice QCD results. A comparison of these phenomenologies can be found in Ref. [96]. We adopt a phenomenological confinement from the Light-Front Holography [49].

2.1.1 Light-Front Holography

The idea of the holographic principle has deep roots in theoretical physics [97], including the light-front quantization [98]. Roughly speaking, it postulates that quantum gravity in a volume is encoded on the boundary of the region. The AdS/CFT correspondence [99, 100, 101] implements the first concrete model of the holographic principle, and establishes the duality between Type IIB string theory on $\mathrm{AdS}_5 \times S^5$ and $\mathcal{N} = 4$ supersymmetric Yang-Mills theory in the 4-dimensional Minkowski space[1]. Remarkably, for strong coupling gauge theory, the string theory dual can be described by a perturbative calculation around the large N_c limit. Therefore, not only this duality provides insights to quantum gravity and string theory, it also offers a fresh pathway to address non-perturbative gauge theories.

The holographic QCD approach is one of the efforts to apply the string/gauge duality to QCD [102]. This approach, also known as the AdS/QCD, studies classical field theory on AdS_5. The field contents are designed to match the symmetries of hadrons instead of seeking the exact gravity duals of QCD. In order to describe QCD confinement, holographic QCD breaks the conformal symmetry in AdS_5 by introducing either a cutoff $z \leq z_m$ in the fifth dimension (the "hard wall" model [103, 104]) or a dilaton field $\varphi(z) = \kappa^2 z^2$ (the "soft wall" model [105]). The location of the hard wall z_m or the strength of the dilaton field κ is matched to the typical QCD confinement scale $\sim 400\,\mathrm{MeV}$. The soft-wall model successfully reproduces Regge trajectories of hadron masses. The predictions based on AdS/QCD generally agree with experiments within 10%–15% [104].

The Light-Front Holography connects AdS/QCD to the semi-classical approximation to QCD on the light front [49] (see Eq. (2.2)). In this theory, the fifth dimension z is mapped to the impact parameter $\zeta_\perp = \sqrt{x(1-x)}r_\perp$, where $r_\perp = |\boldsymbol{r}_{q\perp} - \boldsymbol{r}_{\bar{q}\perp}|$ is the transverse separation

[1] AdS_5 stands for the 5-dimensional Anti-de Sitter space, and S^5 stands for 5-dimensional sphere.

of partons, x is the longitudinal momentum fraction of the quark and $(1-x)$ is that of the anti-quark. The dilaton field is mapped to the effective confining potential. In particular, the soft-wall dilaton field is mapped to the harmonic oscillator confining potential with the impact parameter:

$$\varphi(z) = \kappa^2 z^2 \quad \longrightarrow \quad V_{\rm eff} = \kappa^4 \zeta_\perp^2 + \text{const.} \tag{2.3}$$

It has been shown [106] that this confining potential has a nice interpretation from the conformal quantum mechanics [107].

The soft-wall confinement provides a natural starting point for developing an effective Hamiltonian for quarkonium. The soft-wall Hamiltonian

$$H_{\rm SW} = \frac{\boldsymbol{k}_\perp^2}{x(1-x)} + \kappa^4 \boldsymbol{\zeta}_\perp^2, \tag{2.4}$$

is a 2-dimensional harmonic oscillator in terms of the holographic variables $\boldsymbol{\zeta}_\perp \equiv \sqrt{x(1-x)}\boldsymbol{r}_\perp$ and its conjugate momentum $\boldsymbol{q}_\perp \equiv \boldsymbol{k}_\perp/\sqrt{x(1-x)}$. The eigenfunctions are the 2-dimensional harmonic oscillator functions,

$$\phi_{nm}(\boldsymbol{q}_\perp) = b^{-1}\sqrt{\frac{4\pi n!}{(n+|m|)!}}\left(\frac{q_\perp}{b}\right)^{|m|} \exp\Big(-\frac{q_\perp^2}{2b^2}\Big) L_n^{|m|}(q_\perp^2/b^2) e^{im\theta}, \tag{2.5}$$

where $q_\perp = |\boldsymbol{q}_\perp|$, $\theta = \arg \boldsymbol{q}_\perp$, $b \equiv \kappa$ is the harmonic oscillator scale parameter, and $L_n^\alpha(z)$ is the associated Laguerre polynomial. The corresponding eigenvalues are $2\kappa^2(2n+|m|+1)$, $n = 0, 1, 2, \cdots; m = 0, \pm 1, \pm 2, \cdots$. These eigenfunctions form a complete orthonormal basis. By adopting this basis, the soft-wall Hamiltonian becomes diagonal and the non-perturbative first approximation of the light-front holographic QCD is naturally encoded in the basis space.

2.1.2 Longitudinal confinement

We have adopted the soft-wall confinement. However, this confining potential alone is not sufficient for heavy quarkonium. The soft-wall confinement is designed for massless quarks, and it is inherently 2-dimensional. For the heavy quarkonium system, it should be modified to incorporate the quark masses and the longitudinal degree of freedom (see Ref. [108] for an *ansatz*),

$$H_{\rm SW} = \frac{\boldsymbol{k}_\perp^2}{x(1-x)} + \kappa^4 \boldsymbol{\zeta}_\perp^2 \quad \longrightarrow \quad H_{\rm SW} + H_{\rm L} = \frac{\boldsymbol{k}_\perp^2 + m_f^2}{x(1-x)} + \kappa^4 \boldsymbol{\zeta}_\perp^2 + V_{\rm L}(x), \tag{2.6}$$

where $m_f = m_q = m_{\bar{q}}$ is the quark mass, $V_{\rm L}$ is a confining potential in the longitudinal direction[2]. Here we adopt the longitudinal confining potential,

$$V_{\rm L}(x) = -\frac{\kappa^4}{4m_f^2}\partial_x\big(x(1-x)\partial_x\big). \tag{2.7}$$

Here, $\partial_x \equiv (\partial/\partial x)_{\boldsymbol{\zeta}_\perp}$.

The motivation of this longitudinal confining potential is four-fold.

First of all, the longitudinal dynamics is exactly solvable for this confining potential. The longitudinal eigenvalue equation reads,

$$\left[\frac{m_f^2}{x(1-x)} - \frac{\kappa^4}{4m_f^2}\partial_x\big(x(1-x)\partial_x\big)\right]\chi_l(x) = \omega_l\,\chi_l(x). \tag{2.8}$$

Here ω_l is the mass square eigenvalue and $\chi_l(x)$ is the corresponding eigenfunction. It is convenient to introduce a dimensionless quantity, $\mu \equiv 4m_f^2/\kappa^2$. By doing a change of variable $t = 2x-1$, $u_l(t) \equiv \chi_l(\frac{1}{2}(1+t))$, $\lambda_l = \omega_l 4m_f^2/\kappa^4$, Eq. (2.8) becomes,

$$\frac{\mathrm{d}}{\mathrm{d}t}\Big((1-t^2)\frac{\mathrm{d}}{\mathrm{d}t}u_l(t)\Big) + \Big[\lambda_l - \frac{\mu^2}{1-t^2}u_l(t)\Big] = 0. \tag{2.9}$$

This equation is the Legendre differential equation [109], whose solutions are the associated Legendre functions. To obtain the confining solution, we further impose boundary conditions $\chi_l(0) = \chi_l(1) = 0 \Leftrightarrow u_l(\pm 1) = 0$. For this boundary condition, the eigenvalues are,

$$\lambda_l = (l+\mu)(l+\mu+1) \implies \omega_l = 4m_f^2 + \kappa^2(2l+1) + \frac{\kappa^4}{4m_f^2}l(l+1), \quad l = 0,1,2,3,\cdots \tag{2.10}$$

The corresponding eigenfunctions are better expressed in terms of the Jacobi polynomial[3] $P_l^{(a,b)}(t)$,

$$u_l(x) = (1-t^2)^{\frac{\mu}{2}}P_l^{(\mu,\mu)}(t) \implies \chi_l(x) = \mathcal{N}_l\, x^{\frac{\mu}{2}}(1-x)^{\frac{\mu}{2}}P_l^{(\mu,\mu)}(2x-1), \tag{2.11}$$

where $\mathcal{N}_l$ is a normalization factor. The existence of analytic expression is a major numerical advantage for developing a longitudinal basis within the BLFQ approach.

[2]Note that following Light-Front Holography, the transverse direction refers to the direction of $\boldsymbol{\zeta}_\perp$, and the longitudinal direction is perpendicular to $\boldsymbol{\zeta}_\perp$, not simply to $\boldsymbol{r}_\perp$. Therefore, when we take the partial derivative with respect to x, we keep $\boldsymbol{\zeta}_\perp$ fixed, not $\boldsymbol{r}_\perp$.

[3]We use the Jacobi polynomials instead of the associated Legendre functions since, for non-integer μ, the associated Legendre function $P_l^\mu(t)$ does not necessarily satisfy the boundary condition $u_l(\pm 1) = 0$. Furthermore, using Jacobi polynomials the model provides a simple path for generalizing to the unequal mass scenario. See also Appendix B.

Secondly, the solutions $\chi_l(x)$ resemble the perturbative QCD (pQCD) asymptotic parton distribution $\sim x^\alpha(1-x)^\beta$ for mesons [110].

Thirdly, the longitudinal confinement is consistent with Light-Front Holography in the massless limit $m_f \ll \kappa$. In this limit, the longitudinal excitations are at high energy (see Eq. (2.10)) and the ground state wavefunction $\chi_0(x) = 1$. Thus we recover the massless theory of Brodsky and de Téramond.

Fourthly, in the non-relativistic limit $m_f \gg \kappa$, the longitudinal confinement sits on equal footing with the transverse confinement, where together, they form a 3-dimensional harmonic oscillator potential,

$$\kappa^2\zeta_\perp^2 - \frac{\kappa^4}{4m_f^2}\partial_x\big(x(1-x)\partial_x\big) \quad \longrightarrow \quad \frac{1}{4}\kappa^4\boldsymbol{r}^2, \tag{2.12}$$

and rotational symmetry is manifest.

In the literature, other longitudinal confining potentials have also been proposed [96, 111, 112].

As is mentioned, the eigenfunctions of the longitudinal dynamics form a complete orthonormal basis on $[0,1]$ with the boundary condition $\chi(0) = \chi(1) = 0$. These functions form a natural confining basis for the longitudinal degree of freedom. The normalized longitudinal basis functions are (see Fig. 2.1)

$$\chi_l(x) = \frac{\sqrt{4\pi l!(2l+2\mu+1)\Gamma(l+2\mu+1)}}{\Gamma(l+\mu+1)} x^{\frac{\mu}{2}}(1-x)^{\frac{\mu}{2}} P_l^{(\mu,\mu)}(2x-1), \tag{2.13}$$

where $\Gamma(z)$ is the gamma function.

2.2 Effective One-Gluon Exchange

The phenomenological confinement we introduced in Sect. 2.1 provides a first approximation to heavy quarkonium. It takes into account the long-distance physics. However, in order to reproduce the fine and hyperfine structures as well as the short-distance physics, we have to include additional contributions from QCD. For the heavy quarkonium system, the one-gluon exchange effective potential provides an appealing first approximation to the role of quark-gluon coupling in QCD. The omission of contributions from the higher Fock sectors can be justified

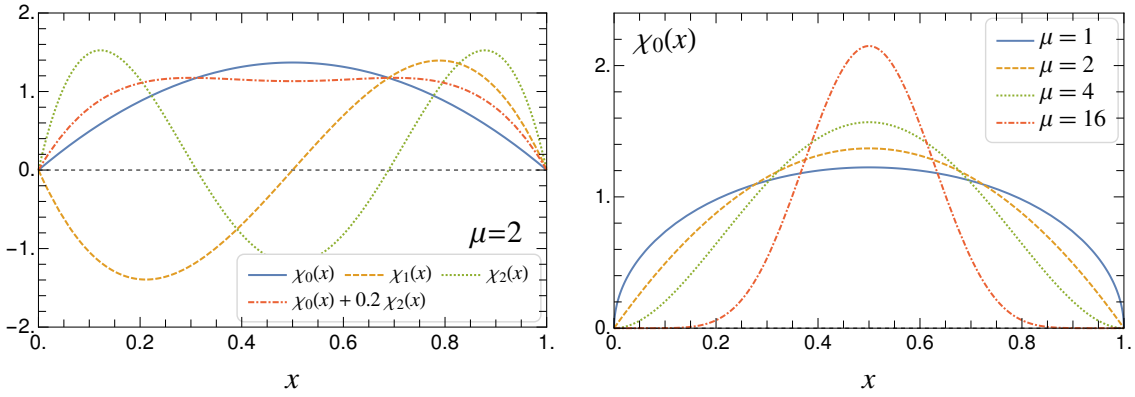

Figure 2.1: The normalized eigenfunctions of the longitudinal Hamiltonian Eq. (2.5). The analytic form of the functions is defined in Eq. (2.13).

by the asymptotic freedom of QCD. At the energy scale of the charm and bottom quarks, the perturbative QCD running coupling $\alpha_s \approx (0.2\text{–}0.3)$.

2.2.1 Effective interaction

To implement the one-gluon exchange, we adopt an effective one-gluon exchange first introduced by Ref. [93] as an *ansatz*. The derivation of this interaction based on the Okubo-Suzuki-Lee method [64, 65], was shown in Ref. [56]. This derivation is facilitated by the systematic perturbative expansion up to the next-to-leading order $\sim \mathcal{O}(\alpha_s)$. The applicability of the perturbation expansion is justified by the asymptotic freedom of QCD [61]. Note that the eigenvalue problem for the bound-state system will be solved non-perturbatively.

The use of the effective interaction is primarily motivated by the cancellation of the collinear divergence $1/(k_g^+)^2$ associated with the instantaneous gluon vertex that arises with the conventional choice of light-cone gauge [56, 113]. This severe divergence prohibits the use of the naïve Light-Front Tamm-Dancoff in gauge theories. The bonus of this procedure, of course, is the dramatic reduction of the matrix size, as one replaces the dynamical gluon sector $|q\bar{q}g\rangle$ by an effective interaction in the $|q\bar{q}\rangle$ sector.

Following Ref. [56] (cf. [93, 114, 115]), we introduce the one-gluon exchange in LFD. In the

color singlet sector[4], this term reads,

$$\hat{V}_{\rm OGE} = -4\pi\alpha_s \frac{N_c^2-1}{2N_c} \sum_{s,\bar{s},s',\bar{s}'} \int \frac{{\rm d}^2k_\perp}{(2\pi)^3} \int_0^1 \frac{{\rm d}x}{2x(1-x)} \int \frac{{\rm d}^2k'_\perp}{(2\pi)^3} \int_0^1 \frac{{\rm d}x'}{2x'(1-x')} \frac{S_{s,\bar{s},s',\bar{s}'}(\boldsymbol{k}_\perp, x, \boldsymbol{k}'_\perp, x')}{Q^2}$$
$$\times \frac{1}{\sqrt{N_c}} \sum_{i'=1}^{N_c} b^\dagger_{i's'}(\boldsymbol{k}'_\perp, x') d^\dagger_{i'\bar{s}'}(-\boldsymbol{k}'_\perp, 1-x') \times \frac{1}{\sqrt{N_c}} \sum_{i=1}^{N_c} d_{i\bar{s}}(-\boldsymbol{k}_\perp, 1-x) b_{is}(\boldsymbol{k}_\perp, x), \quad (2.14)$$

where $N_c = 3$, $(N_c^2-1)/(2N_c) = 4/3$ is the color factor, $S_{s,\bar{s},s',\bar{s}'}$ is the spinor matrix element,

$$S_{s,\bar{s},s',\bar{s}'}(\boldsymbol{k}_\perp, x, \boldsymbol{k}'_\perp, x') = \bar{u}_{s'}(\boldsymbol{k}'_\perp, x') \gamma_\mu u_s(\boldsymbol{k}_\perp, x) \bar{v}_{\bar{s}}(-\boldsymbol{k}_\perp, 1-x) \gamma^\mu v_{\bar{s}'}(-\boldsymbol{k}'_\perp, 1-x') + \text{c.t.}, \quad (2.15)$$

which is tabulated in Table 2.1. The counterterm (c.t.) will be described later in Eq. (2.17). Q^2 is the average squared 4-momentum transfer, $Q^2 = \frac{1}{2}\left(\sqrt{\frac{x'}{x}}\boldsymbol{k}_\perp - \sqrt{\frac{x}{x'}}\boldsymbol{k}'_\perp\right)^2 + \frac{1}{2}\left(\sqrt{\frac{1-x'}{1-x}}\boldsymbol{k}_\perp - \sqrt{\frac{1-x}{1-x'}}\boldsymbol{k}'_\perp\right)^2 + \frac{1}{2}(x-x')^2\left(\frac{m_q^2}{xx'} + \frac{m_{\bar{q}}^2}{(1-x)(1-x')}\right) + \mu_{\rm g}^2$, We have introduced a gluon mass $\mu_{\rm g}$ to regularize the Coulomb singularity. This singularity is integrable and does not carry physical significance [56, 114]. The gluon mass is used to improve the numerics and will be taken small compared to other scales in this application[5].

In Eq. (2.14), we have adopted the relative coordinates. The canonical commutation relations in the relatives coordinates are,

$$\begin{aligned} \left\{b_{i\sigma}(\boldsymbol{k}_\perp, x), b^\dagger_{i'\sigma'}(\boldsymbol{k}'_\perp, x')\right\} =& 2x(1-x)(2\pi)^3\delta^2(\boldsymbol{k}_\perp - \boldsymbol{k}'_\perp)\delta(x-x')\delta_{ii'}\delta_{\sigma\sigma'}, \\ \left\{d_{i\sigma}(\boldsymbol{k}_\perp, x), d^\dagger_{i'\sigma'}(\boldsymbol{k}'_\perp, x')\right\} =& 2x(1-x)(2\pi)^3\delta^2(\boldsymbol{k}_\perp - \boldsymbol{k}'_\perp)\delta(x-x')\delta_{ii'}\delta_{\sigma\sigma'}. \end{aligned} \quad (2.16)$$

In the effective one-gluon exchange interaction Eq. (2.14), we have also neglected the self-energy correction that survives the Fock sector truncation. Even without the self-energies, the one-gluon exchange introduces a logarithmic divergence [57, 93, 116]. This can be seen from the one-gluon exchange kernel by a transverse power counting. In particular, the leading power comes from the spin non-flip spinor matrix elements $S_{\uparrow\downarrow\uparrow\downarrow}$ and $S_{\downarrow\uparrow\downarrow\uparrow}$, which contain terms proportional to $\boldsymbol{k}_\perp^2$ or $\boldsymbol{k}_\perp'^2$. Such terms do not vanish in the large momentum limit[6]. In

[4] The color singlet wavefunction for $q\bar{q}$ system is $\frac{1}{\sqrt{3}}(|r\bar{r}\rangle + |b\bar{b}\rangle + |g\bar{g}\rangle)$, where r, b, g represent the three quark colors and $\bar{r}$, $\bar{b}$, $\bar{g}$ represents the anti-colors for anti-quarks. Note that the one-gluon annihilation channel vanishes within the color singlet sector, as the intermediate gluon carries color.

[5] In QED bound-state systems, e.g. positronium, this integrable singularity is partly responsible for generating the binding. In practice, we found it is sufficient to take the photon mass below a threshold value [56, 57]. In QCD, the majority of the binding comes from the confining interaction.

[6] From the perturbative point of view, this should be canceled by a similar contribution in the cross ladder diagram, which is absent from our Fock space.

Table 2.1: The spinor matrix elements for the equal-mass case $m_f = m_q = m_{\bar{q}}$. We have also included the counterterm. Here, we use the complex representation for the transverse vectors, i.e., for $\boldsymbol{p}_\perp = p_x \boldsymbol{e}_x + p_y \boldsymbol{e}_y$, $k = k_x + ik_y$ and $k^* = k_x - ik_y$.

s	$\bar{s}$	s'	$\bar{s}'$	$\frac{1}{2} S_{s,\bar{s},s',\bar{s}'}(\boldsymbol{k}_\perp, x, \boldsymbol{k}'_\perp, x') / \big(x(1-x)x'(1-x')\big)^{\frac{1}{2}}$
$+$	$+$	$+$	$+$	$m_f^2 \left(\frac{1}{xx'} + \frac{1}{(1-x)(1-x')} \right) + \frac{kk'^*}{x(1-x)x'(1-x')}$
$-$	$-$	$-$	$-$	$m_f^2 \left(\frac{1}{xx'} + \frac{1}{(1-x)(1-x')} \right) + \frac{k^*k'}{x(1-x)x'(1-x')}$
$+$	$-$	$+$	$-$	$m_f^2 \left(\frac{1}{xx'} + \frac{1}{(1-x)(1-x')} \right) + \frac{kk'^*}{xx'} + \frac{k^*k'}{(1-x)(1-x')}$
$-$	$+$	$-$	$+$	$m_f^2 \left(\frac{1}{xx'} + \frac{1}{(1-x)(1-x')} \right) + \frac{k^*k'}{xx'} + \frac{kk'^*}{(1-x)(1-x')}$
$+$	$+$	$+$	$-$	$m_f \frac{x'}{(1-x)(1-x')} \left(\frac{k'}{x'} - \frac{k}{x} \right)$
$-$	$-$	$-$	$+$	$m_f \frac{x'}{(1-x)(1-x')} \left(\frac{k^*}{x} - \frac{k'^*}{x'} \right)$
$-$	$+$	$-$	$-$	$m_f \frac{x}{(1-x)(1-x')} \left(\frac{k'}{x'} - \frac{k}{x} \right)$
$+$	$-$	$+$	$+$	$m_f \frac{x}{(1-x)(1-x')} \left(\frac{k^*}{x} - \frac{k'^*}{x'} \right)$
$+$	$+$	$-$	$+$	$m_f \frac{1-x'}{xx'} \left(\frac{k}{1-x} - \frac{k'}{1-x'} \right)$
$-$	$-$	$+$	$-$	$m_f \frac{1-x'}{xx'} \left(\frac{k'^*}{1-x'} - \frac{k^*}{1-x} \right)$
$+$	$-$	$-$	$-$	$m_f \frac{1-x}{xx'} \left(\frac{k}{1-x} - \frac{k'}{1-x'} \right)$
$-$	$+$	$+$	$+$	$m_f \frac{1-x}{xx'} \left(\frac{k'^*}{1-x'} - \frac{k^*}{1-x} \right)$
$+$	$-$	$-$	$+$	$m_f^2 \frac{-(x-x')^2}{x(1-x)x'(1-x')}$
$-$	$+$	$+$	$-$	$m_f^2 \frac{-(x-x')^2}{x(1-x)x'(1-x')}$
$+$	$+$	$-$	$-$	0
$-$	$-$	$+$	$+$	0

principle, this divergence can be handled by a proper renormalization [35, 68, 117, 118, 119]. However, a systematic non-perturbative renormalization is a challenging task in its own right. We will dedicate Chapter 3 to study one of the renormalization schemes. For the present work, we adopt a simple counterterm *ansatz* [56, 57, 93, 115, 116],

$$\text{c.t.} = \begin{cases} -2\left(\frac{\boldsymbol{k}_\perp^2}{x(1-x)} + \frac{\boldsymbol{k}_\perp'^2}{x'(1-x')}\right), & s, \bar{s}, s', \bar{s}' = +, -, +, - \\ -2\left(\frac{\boldsymbol{k}_\perp^2}{x(1-x)} + \frac{\boldsymbol{k}_\perp'^2}{x'(1-x')}\right), & s, \bar{s}, s', \bar{s}' = -, +, -, + \\ 0 & \text{others.} \end{cases} \tag{2.17}$$

This counterterm exactly removes the troubling $\boldsymbol{k}_\perp^2$ and $\boldsymbol{k}_\perp'^2$ terms in the spinor matrix elements hence removing the UV divergence.

2.2.2 Positronium

As mentioned, the above one-gluon exchange interaction is identical to the one-photon exchange, except for a color factor 4/3. The one-photon exchange has been applied to the positronium system in QED in the basis function approach by Wiecki *et al.* [56, 57].

In this study, Wiecki *et al.* adopted the harmonic oscillator basis functions in the transverse direction (see Eq. (2.5)) and discretized momentum basis in the longitudinal direction (see Sect. 1.6.2). However, the harmonic oscillator scale b is kept a free parameter as there is no confining potential in the positronium case. The longitudinal basis is finite-dimensional for a finite longitudinal resolution K. The transverse harmonic oscillator basis is truncated according to,

$$\sum_i (2n_i + |m_i| + 1) \leq N_{\max}, \tag{2.18}$$

where i sums over Fock space partons (i.e. the electron and the positron). Wiecki *et al.* also implemented one of the symmetries of the light-front Hamiltonian by imposing,

$$\sum_i (m_i + s_i) = m_j \tag{2.19}$$

where s_i is the spin projection of the i-th parton.

With the basis setup, the Hamiltonian matrix was constructed and diagonalized numerically. The obtained mass eigenvalues were extrapolated to the continuum limit: $K \to \infty$, $N_{\max} \to \infty$,

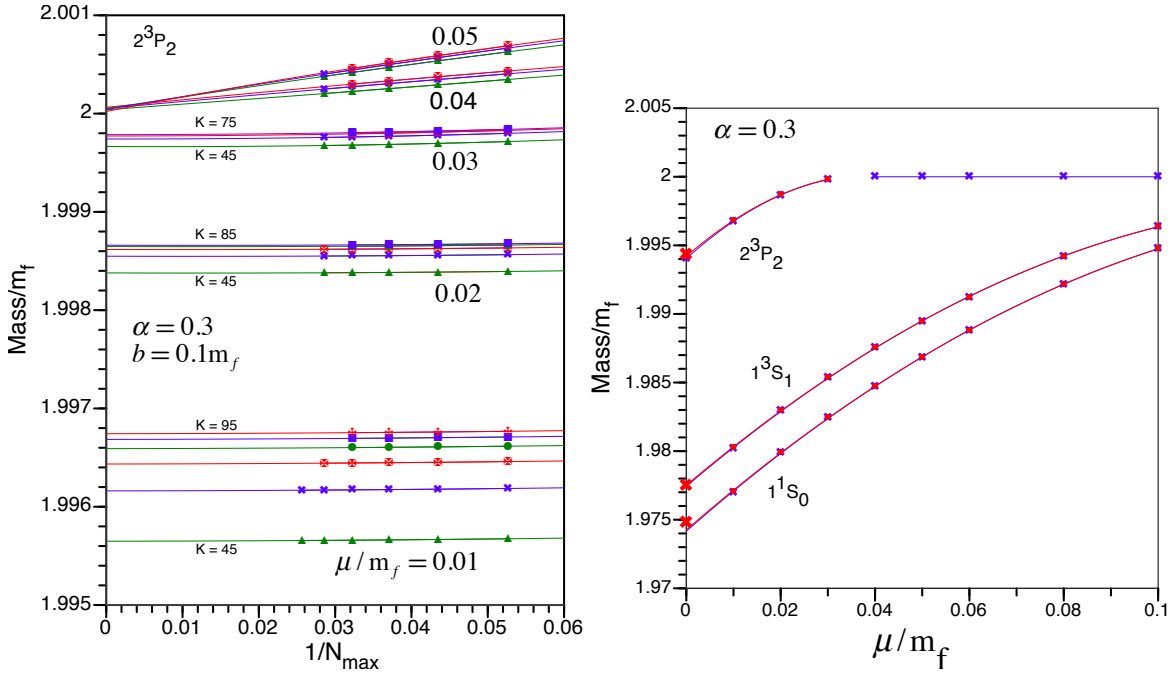

Figure 2.2: (*Left*) The extrapolation of $N_{\max}$ for positronium state $2\,^3P_2$ using second order polynomials. Results for different K (in increments of 10) and μ are presented. b is the scale parameter of the harmonic oscillator basis functions. (*Right*) The extrapolation of μ for positronium states $1\,^1S_0$, $1\,^3S_1$, and $2\,^3P_2$ using second order polynomials. Each red dot are the results of the extrapolation $K \to \infty$ and $N_{\max} \to \infty$. The blue crosses are results with only $N_{\max} \to \infty$ extrapolation but with sufficiently large K. The red crosses are the predictions from the non-relativistic quantum mechanics with $\mathcal{O}(\alpha^4)$ perturbative QED correction. For these calculations, an artificially large $\alpha = 0.3$ is used. m_f and μ are the electron (positron) and photon masses, respectively. Figures are taken from Ref. [56].

$\mu \to 0$ (μ is the photon mass), shown in Fig. 2.2. Finally the extrapolated spectrum was compared with the non-relativistic quantum mechanical results (including perturbative QED correction up to $\mathcal{O}(\alpha^4)$), and turned out in excellent agreement with the latter[7], without using any phenomenological parameters.

One particular feature of the positronium calculation is the use of the single-particle coordinates. The calculation demonstrates the exact treatment of the center-of-mass excitation from the low-lying spectrum. Another noteworthy aspect of the calculation is that the positronium is a particularly challenging test case for BLFQ using the harmonic oscillator basis, as the Coulomb force is long-range whereas the harmonic oscillator basis is a short-range. Nevertheless, this mismatch is overcome through extensive numerical efforts.

Positronium is a prototypical bound-state system for the low-lying heavy quarkonia. One would naïvely expect that the harmonic oscillator basis works better for QCD with confinement. Therefore, the positronium calculation serves as a valuable benchmark for studying the heavy quarkonium in the BLFQ approach.

2.3 Basis Representation of Heavy Quarkonium

In previous sections, we introduced the effective light-cone Hamiltonian for quarkonium,

$$H_{\text{eff}} = \frac{\boldsymbol{k}_\perp^2 + m_q^2}{x} + \frac{\boldsymbol{k}_\perp^2 + m_{\bar{q}}^2}{1-x} + \kappa^4 x(1-x)\boldsymbol{r}_\perp^2 - \frac{\kappa^4}{4m_f^2}\partial_x\big(x(1-x)\partial_x\big) + V_{\text{OGE}}. \tag{2.20}$$

In this section, we focus on solving the eigenvalue equation,

$$H_{\text{eff}}\,|\psi_{h/q\bar{q}}\rangle = M_h^2\,|\psi_{h/q\bar{q}}\rangle, \tag{2.21}$$

in the Basis Light-Front Quantization approach. In the momentum basis,

$$|\psi_{h/q\bar{q}}\rangle = \sum_{s,\bar{s}}\int_0^1 \frac{\mathrm{d}x}{2x(1-x)}\int\frac{\mathrm{d}^2k_\perp}{(2\pi)^3}\psi_{h/q\bar{q}}(\boldsymbol{k}_\perp, x, s, \bar{s})\frac{1}{\sqrt{N_c}}\sum_{i=1}^{N_c} b_{is}^\dagger(\boldsymbol{k}_\perp, x)d_{i\bar{s}}^\dagger(-\boldsymbol{k}_\perp, 1-x)|0\rangle, \tag{2.22}$$

where $\psi_{h/q\bar{q}}(\boldsymbol{k}_\perp, x, s, \bar{s})$ is the LFWF, and is normalized to unity,

$$\int_0^1 \frac{\mathrm{d}x}{2x(1-x)}\int\frac{\mathrm{d}^2k_\perp}{(2\pi)^3}\Big|\psi_{h/q\bar{q}}(\boldsymbol{k}_\perp, x, s, \bar{s})\Big|^2 = 1. \tag{2.23}$$

[7] For example, the ground state binding energy differs only by 2%, despite that an artificially large $\alpha = 0.3$ is used in the calculation for both results.

2.3.1 Basis expansion

The basis states can be obtained from the momentum states by the basis transformation[8],

$$a^\dagger_{n,m,l,s,\bar{s}} = \int_0^1 \frac{\mathrm{d}x}{2x(1-x)} \int \frac{\mathrm{d}^2k_\perp}{(2\pi)^3} \phi_{nm}(\boldsymbol{k}_\perp/\sqrt{x(1-x)})\chi_l(x) \frac{1}{\sqrt{N_c}} \sum_{i=1}^{N_c} b^\dagger_{is}(\boldsymbol{k}_\perp, x) d^\dagger_{i\bar{s}}(-\boldsymbol{k}_\perp, 1-x). \tag{2.24}$$

The state vector expressed in terms of the basis states is,

$$|\psi_{h/q\bar{q}}\rangle = \sum_{n,m,l,s,\bar{s}} \Psi_{n,m,l,s,\bar{s}}\, a^\dagger_{n,m,l,s,\bar{s}}|0\rangle \equiv \sum_\alpha \Psi_\alpha\, a^\dagger_\alpha|0\rangle, \tag{2.25}$$

where coefficients $\Psi_{n,m,l,s,\bar{s}}$ are the basis LFWFs. We have also collected the indices into a single index: $\alpha \equiv (n,m,l,s,\bar{s})$. The LFWFs expressed in terms of the basis LFWFs are,

$$\psi_{h/q\bar{q}}(\boldsymbol{k}_\perp, x, s, \bar{s}) = \sum_{n,m,l} \Psi_{n,m,l,s,\bar{s}}\, \phi_{nm}(\boldsymbol{k}_\perp/\sqrt{x(1-x)})\chi_l(x). \tag{2.26}$$

The harmonic oscillator basis is diagonal with m_j, thus we can fix m_j:

$$m_j = m + s + \bar{s}. \tag{2.27}$$

Our basis is discretized but infinite-dimensional. For practical calculations, we restrict the basis quanta:

$$2n + |m| + 1 \le N_{\max}, \quad l \le L_{\max}, \tag{2.28}$$

with the basis regulators $N_{\max}$ and $L_{\max}$. For the harmonic oscillator basis, $N_{\max}$ is related to a UV regulator $\Omega_{\mathrm{UV}} = \sqrt{N_{\max}}b$, and an IR regulator $\Omega_{\mathrm{IR}} = b/\sqrt{N_{\max}}$ [120], where b is the basis scale parameter and we have taken $b = \kappa$, unless otherwise stated. $L_{\max}$ controls the basis resolution in the longitudinal direction.

The matrix elements of the Hamiltonian operator read,

$$\begin{aligned}
&\langle 0|a_{n',m',l',s',\bar{s}'}\, H_{\mathrm{eff}}\, a^\dagger_{n,m,l,s,\bar{s}}|0\rangle = \\
&\quad \Big(4m_f^2 + 2\kappa^2(2n + |m| + l + \tfrac{3}{2}) + \frac{\kappa^4}{4m_f^2} l(l+1)\Big)\delta_{nn'}\delta_{mm'}\delta_{ll'}\delta_{ss'}\delta_{\bar{s}\bar{s}'} \\
&\quad -\frac{1}{3\pi}\int_0^1 \mathrm{d}x \int_0^1 \mathrm{d}x'\, \chi_{l'}(x')\chi_l(x) \int \frac{\mathrm{d}^2q_\perp}{(2\pi)^2} \int \frac{\mathrm{d}^2q'_\perp}{(2\pi)^2}\, \phi^*_{n'm'}(\boldsymbol{q}'_\perp)\phi_{nm}(\boldsymbol{q}_\perp) \times \frac{\alpha_s}{Q^2} \\
&\quad \times S_{s,\bar{s},s',\bar{s}'}(\sqrt{x(1-x)}\boldsymbol{q}_\perp, x, \sqrt{x'(1-x')}\boldsymbol{q}'_\perp, x').
\end{aligned} \tag{2.29}$$

[8] Note the awkwardness of defining the basis transformation in the relative coordinates. This is a major motivation for switching to the single-particle coordinates (see Sect. 2.2.2) when the number of particles is large ($\gtrsim 4$).

with $Q^2 = \frac{1}{2}\big(\sqrt{x'(1-x)}\boldsymbol{q}_\perp - \sqrt{x(1-x')}\boldsymbol{q}'_\perp\big)^2 + \frac{1}{2}\big(\sqrt{x'(1-x)}\boldsymbol{q}'_\perp - \sqrt{x(1-x')}\boldsymbol{q}_\perp\big)^2 + \frac{1}{2}(x-x')^2\big[\frac{1}{xx'} + \frac{1}{(1-x)(1-x')}\big]m_f^2 + \mu_{\rm g}^2 > 0$. Here the kinetic and the confining part of the Hamiltonian is automatically diagonal, and the one-gluon exchange part is expressed in terms of the basis function integrals.

2.3.2 Quantum number identification

Quarkonia are identified with three discrete quantum numbers j^{PC}: the total angular momentum j, parity $P = \pm 1$ and charge parity $C = \pm 1$. States with different magnetic projection m_j represent the same particle (see Sect. 1.2).

Of the three, only the charge conjugation is kinematical in light-front dynamics, and it can be obtained from the basis LFWFs,

$$C = \langle\psi_{h/q\bar{q}}|\hat{C}|\psi_{h/q\bar{q}}\rangle = \sum_{n,m,l,s,\bar{s}} (-1)^{m+l+1}\Psi^*_{n,m,l,s,\bar{s}}\Psi_{n,m,l,\bar{s},s}. \tag{2.30}$$

Note that s and $\bar{s}$ are swapped.

The parity transformation is dynamical, and therefore, the parity symmetry is generally violated by the Fock sector truncation and the basis truncation. Fortunately, there exists another kinematic discrete symmetry, called the mirror parity symmetry [121, 122]. Mirror parity flips one of the transverse spatial coordinates, say, x^1:

$$(x^0, x^1, x^2, x^3) \xrightarrow{P_x} (x^0, -x^1, x^2, x^3) \;\Leftrightarrow\; (x^+, x^-, x^1, x^2) \xrightarrow{P_x} (x^+, x^-, -x^1, x^2). \tag{2.31}$$

It can be formally defined as $\hat{P}_x = \hat{R}_x(\pi)\hat{P}$ where $\hat{R}_x(\pi)$ is a rotation around the x-axis by an angle of π. Its eigenvalue is related to parity P and the spin j [121],

$$\hat{P}_x|\psi_{h/q\bar{q}}(j, +m_j)\rangle = (-1)^j P|\psi_{h/q\bar{q}}(j, -m_j)\rangle. \tag{2.32}$$

Here we have included j and m_j in the Dirac ket, because mirror parity flips the sign of m_j. Then P can be extracted from the basis LFWFs by,

$$\begin{aligned}(-1)^j P =& \langle\psi_{h/q\bar{q}}(j, -m_j)|\hat{R}_x(\pi)\hat{P}|\psi_{h/q\bar{q}}(j, +m_j)\rangle \\ =& \sum_{n,m,l,s,\bar{s}} (-1)^m\, \Psi^*_{n,-m,l,-s,-\bar{s}}\Psi_{n,m,l,s,\bar{s}}.\end{aligned} \tag{2.33}$$

The total spin operator $\boldsymbol{\mathcal{J}}^2$ is also dynamical in light-front dynamics. As a result, j is no longer an exact quantum number within the truncated basis space and the mass degeneracy for different magnetic projections m_j is lifted. Nevertheless, in a non-relativistic system, such as the heavy quarkonium, the discrepancy is mild and we can still extract j by counting the multiplicity of the nearly-degenerate mass eigenstates.

It is also instructive to assign states the set of non-relativistic quantum numbers $n\,^{2S+1}L_j$, where n, S and L are the radial quantum number, the total constituent spin[9] and the orbital angular momentum, respectively.

The total constituent spin S, though not an exact quantum number, can be extracted from the expectation value of the total constituent spin operator $\boldsymbol{S}^2 \equiv (\boldsymbol{S}_q + \boldsymbol{S}_{\bar{q}})^2$,

$$\langle \psi_{h/q\bar{q}} | \hat{\boldsymbol{S}}^2 | \psi_{h/q\bar{q}} \rangle = S(S+1), \tag{2.34}$$

where $\boldsymbol{S}_q$ ($\boldsymbol{S}_{\bar{q}}$) is the spin operator of the quark (anti-quark). This expression can be obtained using the standard method of raising and lowering operators in quantum mechanics. Then, the total constituent spin S expressed in terms of the basis LFWFs is,

$$S(S+1) = \sum_{n,m,l,s,\bar{s},s',\bar{s}'} \langle s', \bar{s}' | \hat{\boldsymbol{S}}^2 | s, \bar{s} \rangle \Psi^*_{n,m,l,s',\bar{s}'} \Psi_{n,m,l,s,\bar{s}}, \tag{2.35}$$

where the matrix elements $\langle s', \bar{s}' | \hat{\boldsymbol{S}}^2 | s, \bar{s} \rangle$ are listed in Table 2.2. The obtained values of S are close to 0 or 1 within $\sim 10^{-2}$, sufficient for identifying S.

L and S are related to j, P and C by

$$P = (-1)^{L+1}, \quad C = (-1)^{L+S}, \quad |L-S| \leq j \leq L+S. \tag{2.36}$$

For the coupled-channels, the value of L is determined from the mass hierarchy. For example, for $S = 1$ and $m_j = 0$, there are two states with $C = +1$ and $(-1)^j P = +1$, corresponding to the $j = 0$ ($^3P_0$) and the $j = 2$ ($^3P_2$) states. We identify the state with lower mass as the $j = 0$ state and the state with higher mass as the $j = 2$ state. This assignment can be verified by the near degeneracy of masses from $m_j = 1$ and $m_j = 2$ sector, as well as the study of the wavefunction.

n can be also deduced from the mass hierarchy of the spectrum.

[9] Not be confused with the total spin of the composite particle, j, also known as the intrinsic total angular momentum. Here the total constituent spin S sums over only the spin of the constituents.

Table 2.2: The matrix elements of the total constituent spin operator.

$s', \bar{s}', s, \bar{s}$	$\langle s', \bar{s}' \lvert \hat{\boldsymbol{S}}^2 \rvert s, \bar{s} \rangle$
$+,+,+,+$ $-,-,-,-$	2
$+,-,+,-$ $-,+,-,+$ $+,+,-,-$ $-,-,+,+$	1
others	0

Reconstructing these quantum numbers allows us to identify the states and to compare with experimental data and with other methods.

2.4 Numerical Results

The Hamiltonian matrix elements Eq. (2.29) involve a six-dimensional integral (two in the transverse radial direction, two in the transverse angular direction, two in the longitudinal direction). The angular integrations can be evaluated analytically as detailed in Appendix C (cf. Appendix D of Ref. [56]). The residual radial integrations are evaluated using Gauss-Legendre quadratures with the radial coordinates mapped to the interval $(0, 1)$. The longitudinal integrations are evaluated using the Gauss-Jacobi quadratures. The number of quadrature points in the transverse radial direction N_{rad} (longitudinal direction N_{lfx}) is taken to be *at least* twice $N_{\max}$ ($L_{\max}$). The obtained Hamiltonian matrix is diagonalized using LAPACK software [123].

In practice, we choose $\alpha_s = 0.25$, $\mu_{\text{g}} = 0.02\,\text{GeV} \ll \kappa$, and fit the confining strength κ and the constituent quark mass m_f (m_c for charm, m_b for bottom) by minimizing the root-mean-squared (r.m.s.) deviation between our spectrum, in the $m_j = 0$ sector, and the Particle Data Group (PDG) spectrum [124], for the experimentally measured states (8 states for charmonium, 14 states for bottomonium) below the $D\overline{D}$ or $B\overline{B}$ threshold. The detail of these parameters are summarized in Table 2.3. The convergence of the matrix elements with respect to N_{rad} and N_{lfx} is rapid as long as $N_{\text{rad}} > N_{\max}, N_{\text{lfx}} > L_{\max}$. For the calculations listed in Table 2.3, $N_{\max} = L_{\max} = 8, 16, 24$, we choose $N_{\text{rad}} = N_{\text{lfx}} = 64$ for these calculations. Table 2.3 also

Table 2.3: Summary of the model parameters and the posterior r.m.s. derivations. The coupling α_s and the gluon mass μ_g are fixed. The confining strength κ and the quark/anti-quark mass $m_f = m_q = m_{\bar{q}}$ are fitted with $m_j = 0$ using the experimental data below the $D\overline{D}$ or $B\overline{B}$ threshold. The posterior r.m.s. deviations for the $m_j = 0$ spectrum, $\delta M_{m_j=0}$, and the posterior r.m.s. average-m_j spectrum, $\delta\overline{M}$, are computed for states below the threshold.

		α_s	μ_g (GeV)	κ (GeV)	m_f (GeV)	$\delta M_{m_j=0}$(MeV)	$\delta\overline{M}$(MeV)	$\Omega_{\max}$
I	$c\bar{c}$	0.25	0.02	0.952	1.540	48 (8 states)	44 (8 states)	8
	$b\bar{b}$			1.291	4.956	33 (14 states)	33 (14 states)	
II	$c\bar{c}$	0.25	0.02	0.952	1.549	42 (8 states)	37 (8 states)	16
	$b\bar{b}$			1.249	4.980	23 (14 states)	28 (14 states)	
III	$c\bar{c}$	0.25	0.02	0.950	1.553	39 (8 states)	35 (8 states)	24
	$b\bar{b}$			1.224	4.991	23 (14 states)	30 (14 states)	

includes the posterior r.m.s. derivation for the m_j sector, and for the mean masses $\overline{M}$ that will be defined later in Eq. (2.37).

The previous BLFQ study of positronium [56, 57] (see also Sect. 2.2.2) shows that the continuum limit $N_{\max} \to \infty$, $L_{\max} \to \infty$, $\mu_g \to 0$ can be reached through successive extrapolations. However, the numerical effort involved is quite extensive, and the presence of the fitted parameters also leads to ambiguities in the extrapolation. For these reasons, we shall not pursue the numerical extrapolation for this initial work. Instead, we present calculations using three sets of parameters (see Table 2.3), corresponding to $\Omega_{\max} = 8, 16, 24$, respectively, where we have tied together the basis regulators $N_{\max} = L_{\max} \equiv \Omega_{\max}$. Note that κ and m_f are refitted for each set of new basis regulators $\Omega_{\max}$, and show only weak dependence on the basis space limits. For example, for $\Omega_{\max} = 16$ and $\Omega_{\max} = 24$, the change in κ and m_f is only about 2%. The r.m.s. deviations are also comparable, and are consistent with a converging trend.

2.4.1 Spectroscopy

A representative spectrum of bottomonium, classified by m_j, is shown in Fig. 2.3. Degeneracy among different magnetic projections m_j are lifted, due to the violation of the rotational symmetry by the basis space truncation. However, a residual symmetry, the mirror parity, exists, and states with *opposite* magnetic projection m_j still have the same mass. The spectrum

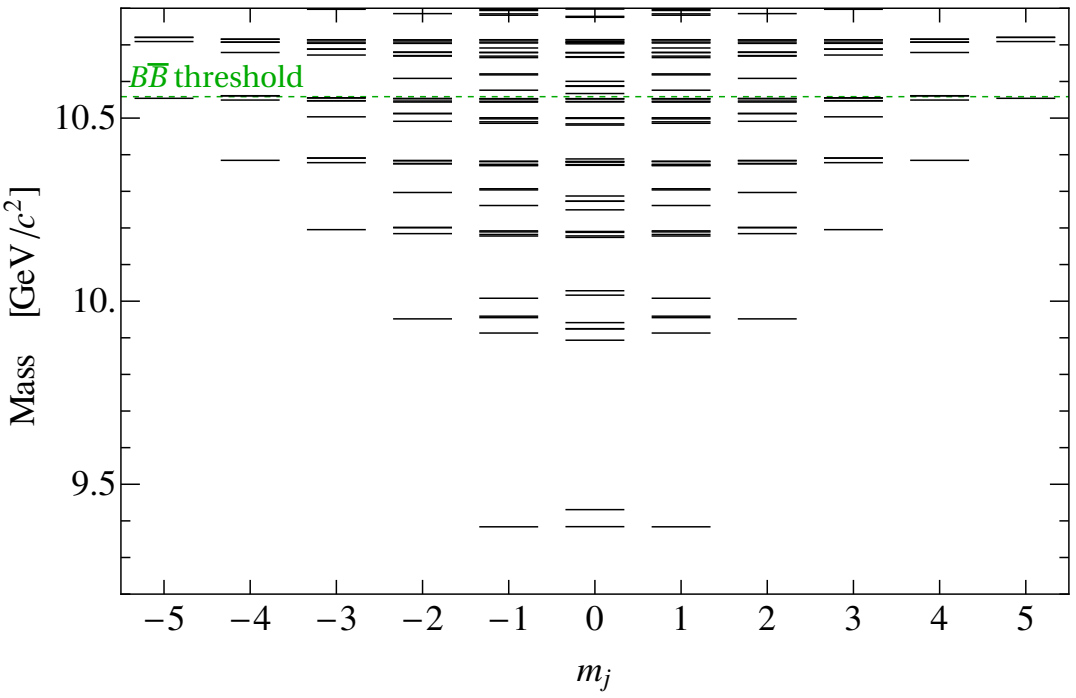

Figure 2.3: Representative spectrum of bottomonium at $N_{\max} = L_{\max} = 24$. Model parameters are given in Table 2.3.

can be further classified by discrete quantum numbers, mirror parity $(-1)^j P$, charge parity C, and total constituent spin S. We use these quantum numbers, together with the approximate degeneracy, as well as the mass hierarchy to identify states.

The identified charmonium and bottomonium spectra for $N_{\max} = L_{\max} = 24$ are shown in Fig. 2.4 and Fig. 2.5. As mentioned, the mass degeneracy for m_j is lifted due to the violation of the rotational symmetry by the Fock sector truncation. We use a box to indicate the spread of masses M_{m_j} from different m_j. The r.m.s. value [116]

$$\overline{M} = [(M_{-j}^2 + M_{1-j}^2 + \cdots + M_{+j}^2)/(2j+1)]^{\frac{1}{2}} \tag{2.37}$$

are shown as dashed bars. We compare our results with the experimental data from the particle data group (PDG, [124], cf. [125]). The r.m.s. deviations between theory and experiment (with $\overline{M}$ used for the theory) are computed for charmonium (bottomonium) below the $D\overline{D}$ ($B\overline{B}$) threshold, and listed as $\delta\overline{M}$ in Table. 2.3.

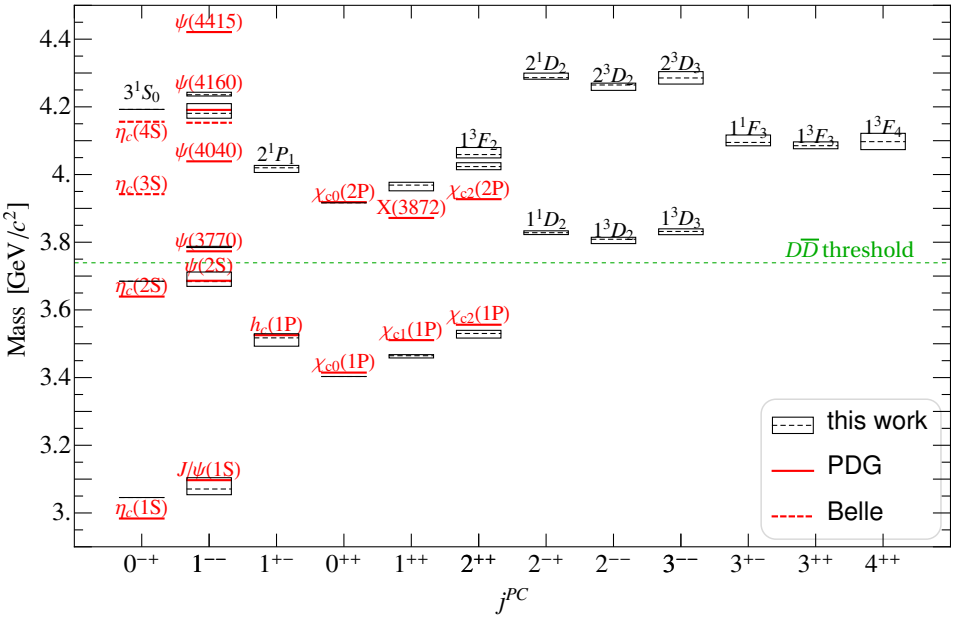

Figure 2.4: The charmonium spectrum at $N_{\max} = L_{\max} = 24$. The known states are labeled by their PDG symbols in red. The unknown states are labeled by the non-relativistic symbols in black. The spread of M_{m_j} is indicated by a box and $\overline{M}$ is shown as dashed lines. Model parameters are given in Table 2.3.

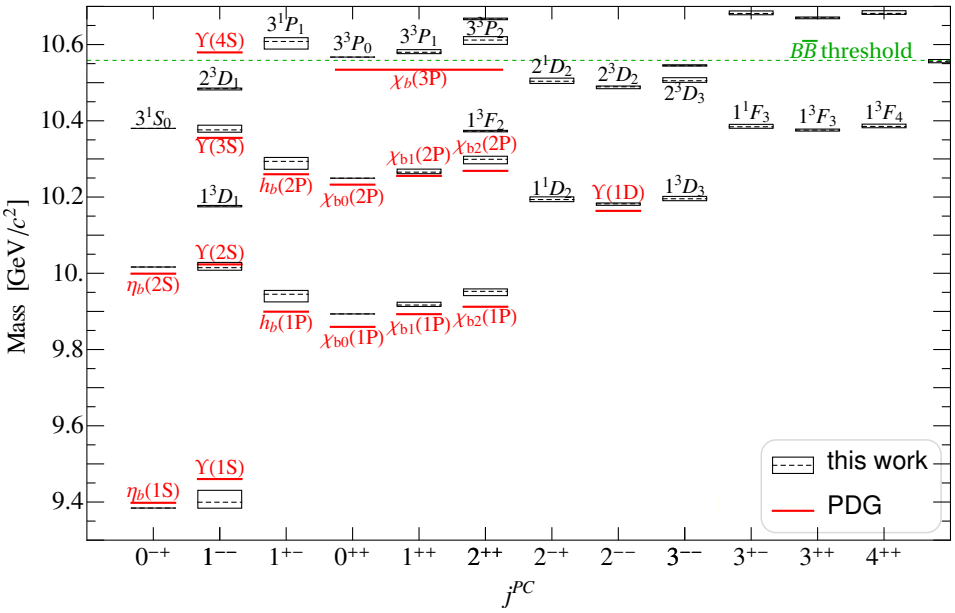

Figure 2.5: The bottomonium spectrum at $N_{\max} = L_{\max} = 24$. The known states are labeled by their PDG symbols in red. The unknown states are labeled by the non-relativistic symbols in black. The spread of M_{m_j} is indicated by a box and $\overline{M}$ is shown as dashed lines. Model parameters are given in Table 2.3.

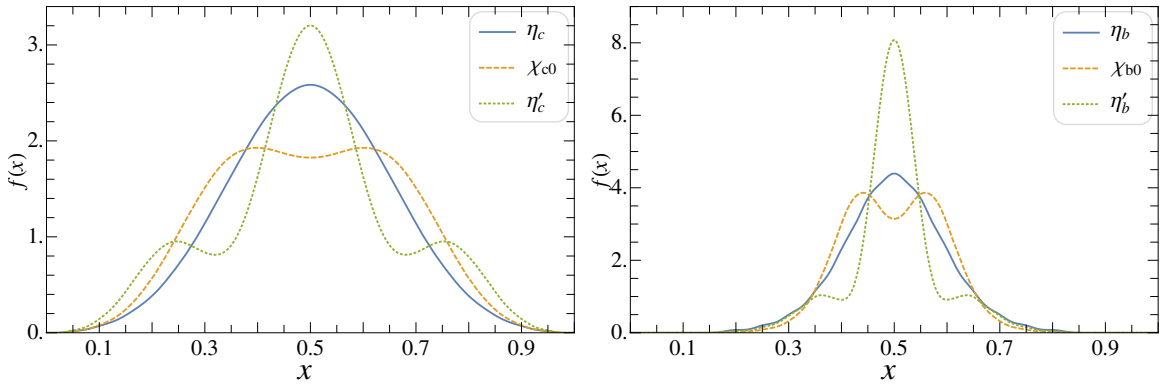

Figure 2.6: The quark distributions of selected charmonium (*left*) and bottomonium (*right*) states at $N_{\max} = L_{\max} = 24$.

2.4.2 Parton distributions

The non-perturbative approach produces not only the mass eigenvalues, but also provides the LFWFs. The LFWFs encode rich information on the structure of the system, e.g. the quark probability distributions [126, 127, 128, 129]. One of the frequently discussed distributions is the parton distribution for quarks, also known as the distribution amplitude [10], which is defined as,

$$\begin{aligned} f(x) =& \frac{1}{2x(1-x)} \sum_{s,\bar{s}} \int \frac{\mathrm{d}^2 k_\perp}{(2\pi)^3} \psi^*_{h/q\bar{q}}(\boldsymbol{k}_\perp, x, s, \bar{s}) \psi_{h/q\bar{q}}(\boldsymbol{k}_\perp, x, s, \bar{s}) \\ =& \frac{1}{4\pi} \sum_{n,m,l,l',s,\bar{s}} \Psi^*_{n,m,l',s,\bar{s}} \Psi_{n,m,l,s,\bar{s}}\ \chi_{l'}(x) \chi_l(x). \end{aligned} \tag{2.38}$$

For our simple two-body system, the parton distribution of the anti-quark is simply $f(1-x)$. The parton distribution $f(x)$ admits a probabilistic interpretation, and it represents the probability density of finding a quark carrying fraction x of the total momentum P^+. Therefore, it satisfies the following sum rules:

$$\int_0^1 \mathrm{d}x\, f(x) = 1, \quad \int_0^1 \mathrm{d}x\, x f(x) + \int_0^1 \mathrm{d}x\, (1-x) f(1-x) = 1. \tag{2.39}$$

The second sum rule comes from the longitudinal momentum conservation.

The quark distributions of selected charmonium and bottomonium states are shown in the left and right panels of Fig. 2.6, respectively. In both charmonium and bottomonium cases, the excited states exhibit features consistent with the angular and/or radial excitation of the

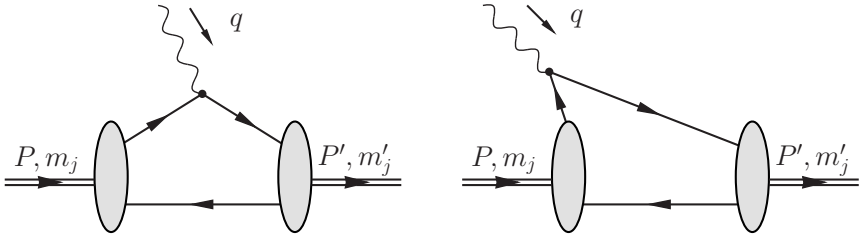

Figure 2.7: The diagonal (*left*) and off-diagonal (*right*) contributions to the elastic electromagnetic form factors within the impulse approximation. The off-diagonal contribution (*right*) is suppressed in the Drell-Yan frame $q^+ = 0$ due to the longitudinal momentum conservation.

states. In general, the bottomonium distributions are very similar to the charmonium ones, except narrower in x (note the scale difference of the vertical axis). This is consistent with the non-relativistic depiction of the heavy quarkonium, and the fact that c quark is lighter than b quark.

2.4.3 Elastic form factors

The LFWFs provide direct access to hadronic observables. Here we study the elastic form factor. In QFT, form factors are defined from the Lorentz decomposition of the matrix elements of the electromagnetic current operator:

$$\langle \psi_{h/q\bar{q}}(P'; j, m'_j) | \hat{J}^\mu(x) | \psi_{h/q\bar{q}}(P; j, m_j) \rangle \equiv 2P^+ I^\mu_{m_j, m'_j}(Q^2) e^{iq\cdot x}, \tag{2.40}$$

where $q \equiv P' - P$, and $Q^2 \equiv -q^2$, j is the spin of the particle and m_j is the magnetic projection. Assuming parity and time-reversal symmetry, there are in total $(2j+1)$ independent Lorentz scalars for each given q^2, known as the elastic form factors [130].

Of course, for heavy quarkonium, the elastic form factors are exactly zero due to the charge conjugation symmetry. Therefore, for our illustration purpose here we artificially couple the probing photon only to the quark. The resulting form factors are not physical observables, but they do provide us with valuable insight to the system. In particular, the r.m.s. radius arises from the charge form factor $G_0(Q^2)$ at small momentum transfer [130, 131],

$$\langle r_h^2 \rangle = -6 \lim_{Q^2 \to 0} \frac{\partial}{\partial Q^2} G_0(Q^2), \tag{2.41}$$

which characterizes the size of the bound state.

In light-front dynamics, the current matrix elements can be obtained using the "good current" — the "+" component of the current operator — in the Drell-Yan frame $q^+ = 0$ (see Fig. 2.7). The resulting expression is known as the the Drell-Yan-West formula [132, 133]:

$$I^+_{m_j,m'_j}(Q^2) = \sum_{s,\bar{s}} \int_0^1 \frac{\mathrm{d}x}{2x(1-x)} \int \frac{\mathrm{d}^2k_\perp}{(2\pi)^3} \psi^{jm'_j *}_{h/q\bar{q}}(\boldsymbol{k}_\perp + (1-x)\boldsymbol{q}_\perp, x, s, \bar{s}) \psi^{jm_j}_{h/q\bar{q}}(\boldsymbol{k}_\perp, x, s, \bar{s}), \quad (2.42)$$

where $Q^2 = -q^2 = \boldsymbol{q}^2_\perp$. We have specified the spin j and the magnetic projections m_j in the LFWFs.

As mentioned above, in light-front dynamics, parity is a dynamical symmetry and the degeneracy due to parity is usually lifted due to basis space truncation. Applying the mirror parity and time-reversal symmetry, the number of independent "good current" matrix elements are reduced to $(j+1)^2$ for integer spins and $(j+\frac{1}{2})(j+\frac{3}{2})$ for half-integer spins [134]. The number of independent "good current" matrix elements for the few lowest spins are summarized in Table 2.4. As evident for particles with spin $j \geq 1$, there are generally more independent "good current" matrix elements than the number of form factors. In principle, if rotational symmetry[10] is preserved, the "good current" matrix elements are constrained by additional conditions. For example, for $j = 1$ particle, the four "good current" matrix elements, $I^+_{0,0}$, $I^+_{1,1}$, $I^+_{1,0}$, and $I^+_{1,-1}$, are related by [131],

$$\Delta(Q^2) \equiv (1+2\eta) I^+_{1,1} + I^+_{1,-1} - \sqrt{8\eta} I^+_{1,0} - I^+_{0,0} = 0, \quad (2.43)$$

where $\eta = Q^2/(4m_h^2)$, and $m_h^2 = P^2$ is the squared mass of the particle. If the rotational symmetry is violated, then $\Delta \neq 0$ and there exists ambiguity for extracting the form factors from the "good current" matrix elements $I^+_{m_j,m'_j}$ [131, 135, 136].

We consider the form factor for the first few (pseudo-)scalar and (axial-)vector mesons. For (pseudo-)scalars, the charge form factor is the only "good current" matrix element: $G_0(Q^2) = I^+_{0,0}(Q^2)$. For (axial-)vector mesons, we adopt the prescription of Grach and Kondratyuk [135], which has been shown to be free of zero-mode contributions[11] in some analytical models [131,

[10] Parity and mirror parity can be related by rotations.

[11] Zero-Mode contributions refer to the non-vanishing off-diagonal contributions (see Fig. 2.7) within the limit $q^+ \to 0$.

Table 2.4: The number of "good current" matrix elements $I^+_{m_j,m'_j}$.

spin	total	independent (LF)	form factors (covariant)
j	$(2j+1)^2$	$(j+1)^2$	$2j+1$
0	1	1	1
1	9	4	3
2	25	9	5
j	$(2j+1)^2$	$(j+\frac{3}{2})(j+\frac{1}{2})$	$2j+1$
1/2	4	2	2
3/2	16	6	4
5/2	36	12	6

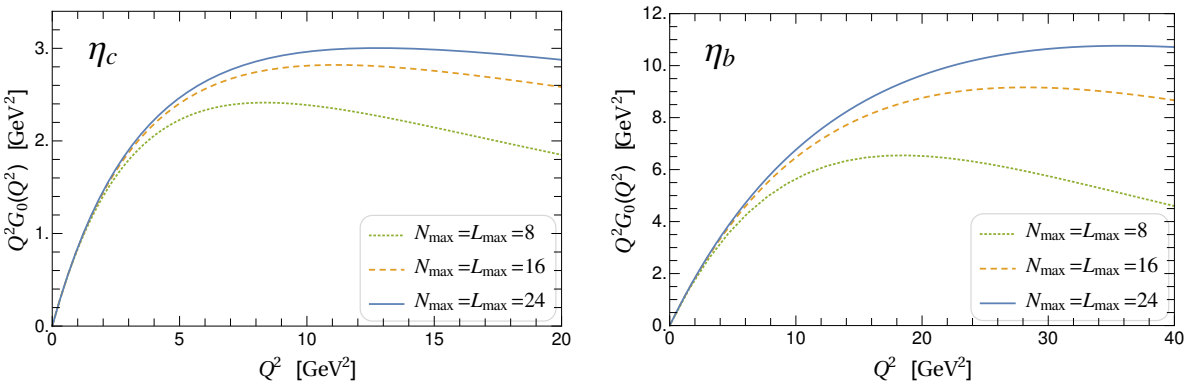

Figure 2.8: The basis-regulator dependence of the charge form factor of η_c and η_b.

136]. The three form factors according to this prescription read,

$$G_0 = \frac{1}{3}\Big[(3-2\eta)I^+_{1,1} + 2\sqrt{2\eta}I^+_{1,0} + I^+_{1,-1}\Big], \qquad \text{[charge]} \tag{2.44}$$

$$G_1 = 2\Big[I^+_{1,1} - \frac{1}{\sqrt{2\eta}}I^+_{1,0}\Big], \qquad \text{[magnetic]} \tag{2.45}$$

$$G_2 = \frac{2\sqrt{2}}{3}\Big[-\eta I^+_{1,1} + \sqrt{2\eta}I^+_{1,0} - I^+_{1,-1}\Big] \qquad \text{[quadrupole]} \tag{2.46}$$

where $\eta = Q^2/(4m_h^2)$.

Figure 2.8 shows the charge form factors for the ground-state charmonium (η_c) and bottomonium (η_b) evaluated at different basis regulators $N_{\max} = L_{\max} = 8, 16, 24$. The form factors show a good trend towards convergence for the range of momentum transfer depicted. Fig. 2.9 shows the charge, magnetic and quadrupole form factors for the lowest vector charmonium (J/ψ) and bottomonium (Υ) using the Grach-Kondratyuk prescription. The magnetic form factor G_1 at the origin gives a zero anomalous magnetic moment, due to the lack of

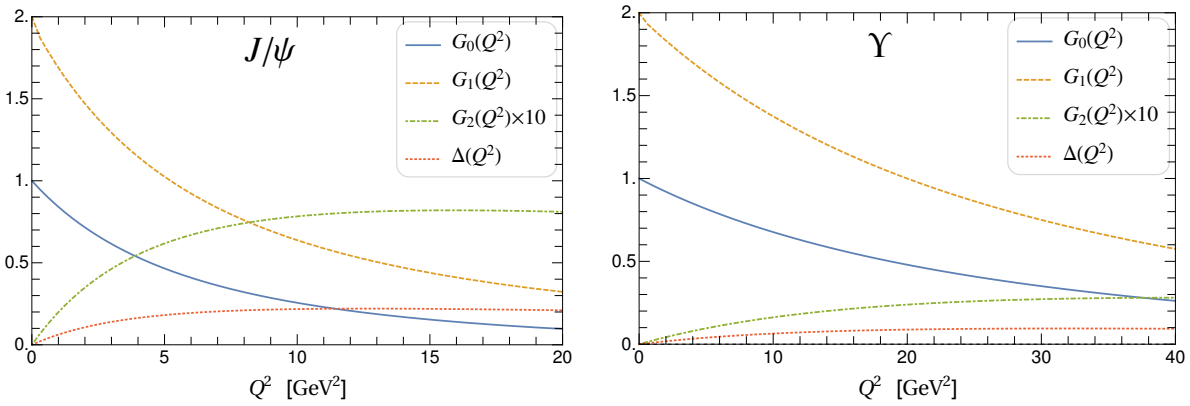

Figure 2.9: The charge, magnetic and quadrupole form factors of J/ψ (*left*) and Υ (*right*), along with the measure ($\Delta(Q^2)$, Eq. (2.43)) of rotational symmetry violation at $N_{\max} = L_{\max} = 24$.

Table 2.5: The heavy quarkonium mean-square radii (in fm^2) at $N_{\max} = L_{\max} = 24$.

	$\langle r^2_{\eta_c}\rangle$	$\langle r^2_{J/\psi}\rangle$	$\langle r^2_{\chi_{c0}}\rangle$	$\langle r^2_{\eta'_c}\rangle$	$\langle r^2_{\eta_b}\rangle$	$\langle r^2_{\Upsilon}\rangle$	$\langle r^2_{\chi_{b0}}\rangle$	$\langle r^2_{\eta'_b}\rangle$
This work	0.040	0.042	0.072	0.127	0.010	0.010	0.028	0.053
Lattice [137]	0.063(1)	0.066(2)	0.095(6)					
DSE [138]	0.048(4)	0.052(3)						

dynamical gluon sector.

Figure 2.10 presents the charge form factors for the first few charmonia (η_c, J/ψ, χ_{c0}) and bottomonia (η_b, Υ, and χ_{b0}). We extract r.m.s. radii from the charge form factors and list them in Table 2.5. Our results are compared with those from the Lattice QCD approach (Lattice) [137] and the Dyson-Schwinger Equation approach (DSE) [138]. From our results, the radius of J/ψ is close to, but slightly larger than, that of η_c. This is consistent with the Lattice and DSE results and can be understood from the non-relativistic point of view. Bottomonia are in general smaller than their counterpart charmonium, a result, again, that can be drawn from the non-relativistic argument. The comparison of the first few available results shows that radii from our approach are in qualitative agreement with those of other approaches, though ours are systematically smaller than the Lattice and DSE results.

In the bottom panels of Fig. 2.10, we compare the pseudo scalar charge form factor with the asymptotic leading order (LO) pQCD predictions [139] in terms of the decay constants $f_{\eta_c} \approx 330\,\text{MeV}$, $f_{\eta_b} \approx 748\,\text{MeV}$ (see Sect. 2.4.4). Here we have used the PDG value for η_c and

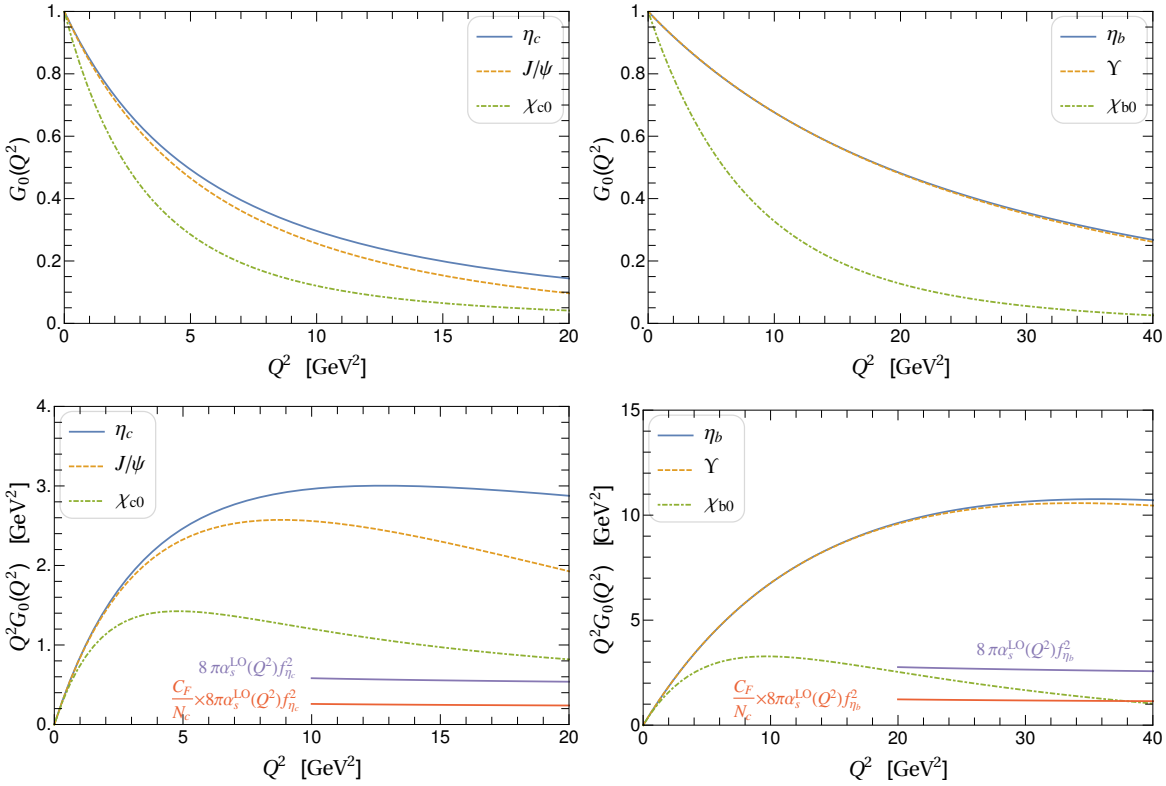

Figure 2.10: The charge form factors for the lowest few charmonium (*left*) and bottomonium (*right*) states at $N_{\rm max} = L_{\rm max} = 24$. We compare the pseudo scalar charge form factor with the asymptotic leading order pQCD predictions [139] in terms of the decay constants $f_{\eta_c} \approx 330\,\text{MeV}$, $f_{\eta_b} \approx 748\,\text{MeV}$. The two sets of pQCD values correspond to the distribution amplitude $\phi_{\rm P}(x) = 6x(1-x)$ and $\phi_{\rm P}(x) = \delta(x - 1/2)$, respectively.

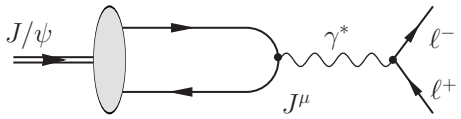

Figure 2.11: The Feynman diagram of the dilepton decay of J/ψ through a virtual photon. J^μ is the electromagnetic current. This process can be parametrized by the decay constant $f_{J/\psi}$.

our value (at $N_{\max} = L_{\max} = 24$) for η_b, as the latter is currently not available from PDG. The asymptotic behavior of the form factor is related to the decay constant by [139],

$$Q^2 F_{\rm P}(Q^2) \sim \frac{f_{\rm P}^2}{8N_c} \int_0^1 {\rm d}x \int_0^1 {\rm d}y\, \phi_{\rm P}(x) \frac{16\pi C_F \alpha_s(Q^2)}{xyQ^2} \phi_{\rm P}(y), \tag{2.47}$$

where $C_F = \frac{N_c^2-1}{2N_c}$, and $\phi_{\rm P}(x)$ is the parton distribution of the pseudo scalar meson P. The pQCD asymptotic predictions for two well studied parton distributions [139] are shown in Fig. 2.10,

$$Q^2 F_{\rm P}(Q^2) \overset{Q\to\infty}{\longrightarrow} 8\pi\alpha_s(Q) f_{\rm P}^2 \begin{cases} 1 & \big(\phi_{\rm P}(x) = 6x(1-x)\big) \\ \frac{C_F}{N_c} = \frac{4}{9} & \big(\phi_{\rm P}(x) = \delta(x-\frac{1}{2})\big). \end{cases} \tag{2.48}$$

For the parton distributions from our results, Sect. 2.4.2, the corresponding pQCD asymptotic predictions are similar,

$$Q^2 F_{\eta_c}(Q^2) \overset{Q\to\infty}{\longrightarrow} 0.57 \times 8\pi\alpha_s(Q) f_{\eta_c}^2, \quad Q^2 F_{\eta_b}(Q^2) \overset{Q\to\infty}{\longrightarrow} 0.48 \times 8\pi\alpha_s(Q) f_{\eta_b}^2. \tag{2.49}$$

2.4.4 Decay constants

The LFWFs are readily used to study hadron reactions. Here we consider the decay constants. These quantities are useful for computing the decay and transition widths (see Fig. 2.11), and constraining the Standard Model parameters [74]. In the non-relativistic limit, they are proportional to the wavefunctions at the origin [140], and therefore, test the short-distance physics of the model. The decay constants for scalar S (0^+), pseudo-scalar P (0^-), axial-vector A (1^+), and vector V (1^-) mesons are defined as [76, 141, 142],

$$\langle 0|\overline{\psi}\gamma^\mu\gamma^5\psi|{\rm P}(p)\rangle = ip^\mu f_{\rm P}, \tag{2.50}$$

$$\langle 0|\overline{\psi}\gamma^\mu\psi|{\rm V}(p,\lambda)\rangle = e_\lambda^\mu(p) m_{\rm V} f_{\rm V}\,, \qquad (\lambda = 0, \pm 1) \tag{2.51}$$

$$\langle 0|\overline{\psi}\gamma^\mu\psi|{\rm S}(p)\rangle = p^\mu f_{\rm S}, \tag{2.52}$$

$$\langle 0|\overline{\psi}\gamma^\mu\gamma^5\psi|{\rm A}(p,\lambda)\rangle = e_\lambda^\mu(p) m_{\rm A} f_{\rm A}\,, \qquad (\lambda = 0, \pm 1) \tag{2.53}$$

respectively, where m_h are the masses, and $e^\mu_\lambda(p)$ is the spin vector for the vector boson. Note that due to the charge conjugation symmetry, the decay constants of mesons with quantum numbers 0^{++} (non-exotic scalars, e.g., χ_{c0}, χ_{b0}) and 1^{+-} (e.g., h_c, h_b) vanish. In light-front dynamics, the decay constants can be computed from the "+" component of the current matrix elements (see Fig. 2.11). The resultant expressions are [139],

$$\begin{aligned} f_{\rm P,A} =& \frac{\sqrt{N_c}}{P^+}\sum_{s,\bar{s}}\int_0^1 \frac{{\rm d}x}{2x(1-x)}\int\frac{{\rm d}^2k_\perp}{(2\pi)^3}\,\psi_{h/q\bar{q}}(\boldsymbol{k}_\perp,x,s,\bar{s})\,\bar{v}_{\bar{s}}(\bar{k})\gamma^+\gamma^5 u_s(k) \\ =& 2\sqrt{N_c}\int_0^1\frac{{\rm d}x}{2\sqrt{x(1-x)}}\int\frac{{\rm d}^2k_\perp}{(2\pi)^3}\left[\psi_{h/q\bar{q}}(\boldsymbol{k}_\perp,x,\uparrow,\downarrow)-\psi_{h/q\bar{q}}(\boldsymbol{k}_\perp,x,\downarrow,\uparrow)\right], \end{aligned} \tag{2.54}$$

$$\begin{aligned} f_{\rm S,V} =& \frac{\sqrt{N_c}}{P^+}\sum_{s,\bar{s}}\int_0^1 \frac{{\rm d}x}{2x(1-x)}\int\frac{{\rm d}^2k_\perp}{(2\pi)^3}\,\psi_{h/q\bar{q}}(\boldsymbol{k}_\perp,x,s,\bar{s})\,\bar{v}_{\bar{s}}(\bar{k})\gamma^+ u_s(k) \\ =& 2\sqrt{N_c}\int_0^1\frac{{\rm d}x}{2\sqrt{x(1-x)}}\int\frac{{\rm d}^2k_\perp}{(2\pi)^3}\left[\psi_{h/q\bar{q}}(\boldsymbol{k}_\perp,x,\uparrow,\downarrow)+\psi_{h/q\bar{q}}(\boldsymbol{k}_\perp,x,\downarrow,\uparrow)\right], \end{aligned} \tag{2.55}$$

where $k^+ = xP^+$, $\bar{\boldsymbol{k}}^+ = (1-x)P^+$, and $\bar{k}_\perp = -\boldsymbol{k}_\perp$. P^+ is the longitudinal momentum of the meson. The definition and identities of the Dirac spinors are collected in Appendix A. In the non-relativistic limit, the above expressions yield the well-known formula of Van Royen and Weisskopf [140]:

$$f_h \approx 2\sqrt{\frac{N_c}{m_h}}\int\frac{{\rm d}^3k}{(2\pi)^3}\psi^{\rm NR}_{h/q\bar{q}}(\boldsymbol{k}) = 2\sqrt{\frac{N_c}{m_h}}\widetilde{\psi}^{\rm NR}_{h/q\bar{q}}(\boldsymbol{r}=0). \tag{2.56}$$

where

$$\psi^{\rm NR}_{h/q\bar{q}}(\boldsymbol{k}) \approx \frac{1}{\sqrt{2}}\left[\psi_{h/q\bar{q}}(\boldsymbol{k}_\perp,x,\uparrow,\downarrow)\pm\psi_{h/q\bar{q}}(\boldsymbol{k}_\perp,x,\downarrow,\uparrow)\right]\times\frac{1}{\sqrt{2m_h}} \tag{2.57}$$

is the non-relativistic wavefunction and $\widetilde{\psi}^{\rm NR}_{h/q\bar{q}}(\boldsymbol{r})$ is its Fourier transformation.

The decay constants from this work are plotted in Fig. 2.12. We also list the PDG data [124], as well as results from Lattice QCD (Lattice, [143, 144, 145, 146]), and the Dyson-Schwinger equation (DSE, [80]). The PDG data are extracted from the dilepton decay widths Γ_{ee} (for vectors, see also Fig. 2.11) and diphoton decay widths $\Gamma_{\gamma\gamma}$ (for pseudo-scalars) [76, 141, 142, 143],

$$\begin{aligned} \Gamma_{{\rm V}\to e^+e^-} =& \frac{4\pi}{3}e_Q^2\alpha_{\rm em}^2\frac{f_{\rm V}^2}{m_{\rm V}}, \\ \Gamma_{{\rm P}\to\gamma\gamma} =& 4\pi e_Q^4\alpha_{\rm em}^2\frac{f_{\rm P}^2}{m_{\rm P}}, \end{aligned} \tag{2.58}$$

where e_Q is the charge of the constituent quark ($e_Q = 2/3$ for charm quark and $e_Q = -1/3$ for bottom quark), $m_{\rm P}$ ($m_{\rm V}$) is the mass of the pseudo scalar (vector) meson, $\alpha_{\rm em}$ is the QED

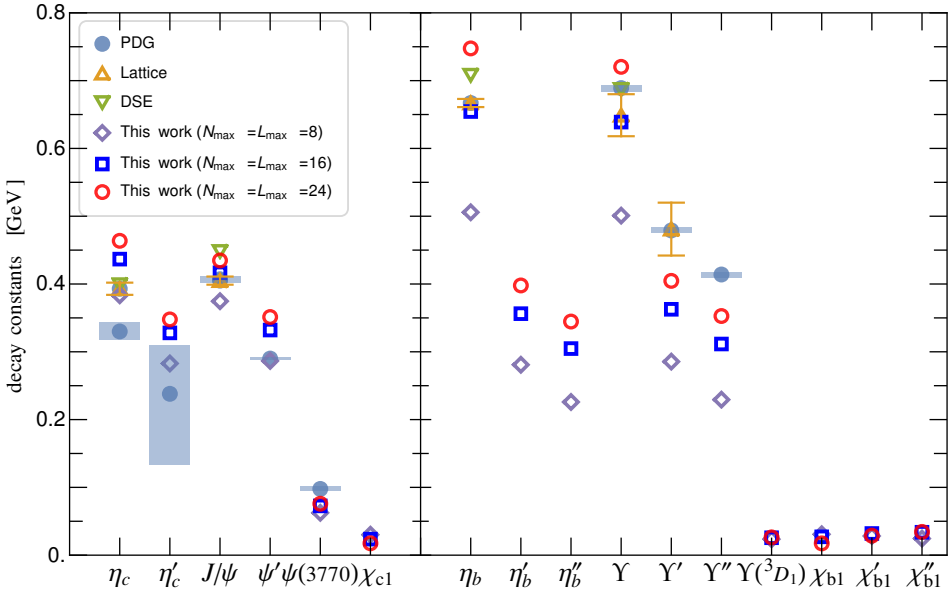

Figure 2.12: The decay constants of scalar and vector quarkonia as compared with PDG data [124] as well as Lattice QCD (Lattice) [143, 144, 145, 146] and Dyson-Schwinger (DSE) [80] approaches. Model parameters κ and m_q are fitted to the PDG masses separately for three regulators $N_{\rm max} = L_{\rm max} = 8, 16, 24$, while $\alpha = 0.25$ and $\mu_{\rm g} = 0.02\,{\rm GeV}$ are kept fixed.

coupling counstant[12]. The higher order pQCD correction is assumed to be included in the non-perturbative dynamics of the bound states.

We present results for three successive sets of basis regulators, $N_{\rm max} = L_{\rm max} = 8, 16, 24$. For these three regulators, the parameters κ and m_q are fitted to the mass spectrum separately, and $\alpha = 0.25$, $\mu_{\rm g} = 0.02\,{\rm GeV}$ are kept fixed. While the resultant masses are close as we mentioned, the decay constants show noticeable changes, indicating some residual regulator dependence. This may not be a surprise as the decay constant probes the short-distance physics. We therefore expect slower convergence for the decay constants than the masses.

From Fig 2.12, our calculated decay constants are in reasonable agreement with the known experimental measurements as well as Lattice and DSE results, in particular. Considering the simplicity of our Hamiltonian, this is encouraging. However, compared to Lattice and DSE results, our results show larger deviations from the PDG data. The deviations are even larger after an extrapolation. This is likely due to the systematic errors[13] of our model and can be

[12] For heavy quarkonium, the running of the QED coupling is noticeable [147]. Consequently, for charmonium, we take $\alpha_{\rm em}(3.5\,{\rm GeV}) \simeq 1/134$; for bottomonium, we take $\alpha_{\rm em}(9.5\,{\rm GeV}) \simeq 1/132$.

[13] Two notable sources are: (1) the evolution of the QCD coupling; (2) the wavefunction renormalization Z_2

improved by a more consistent renormalization, by including more QCD contributions to the LF Hamiltonian and/or by including higher Fock sectors.

Figure 2.12 also includes decay constants for the D-wave states. In the non-relativistic limit, these quantities should vanish. The small but non-vanishing D-wave decay constants in our results indicate the mixing of the S-wave component, as expected from our relativistic treatment.

of the quark field.

CHAPTER 3. NON-PERTURBATIVE RENORMALIZATION

The term renormalization applies to mathematical procedures that either eliminate divergences or install other desired properties in a calculation based on an initial statement of the theory. A desired property could be, for example, that a physical theory, having constants that are not known in advance, properly reproduces a known physical mass and/or a known physical cross section. All other results from the physical theory are then testable predictions.

Renormalization is a vital part of the *ab initio* approaches to quantum field theories. For example, in the BLFQ application to heavy quarkonium in Sect. 2, even though we ignored the self energies, the vertex corrections and the vacuum polarizations, we still encountered a UV divergence. There, an *ad hoc* scheme was used to regularize the theory. Despite the initial success, in principle, a proper systematic renormalization is required, which is also somewhat reflected from the mass spectrum and the decay constants results.

However, performing a systematic non-perturbative renormalization in the Hamiltonian formalism is a major challenge. Perturbative renormalization is not sufficient in the non-perturbative regime, as we need to sum over an infinite number of perturbative diagrams. The non-perturbative approaches usually involve numerical methods, as we have seen in the preceding chapters. Therefore, a non-perturbative renormalization has to be analytically tractable and numerically robust in order to be used in practical numerical calculations. Above all, a successive non-perturbative renormalization scheme has to guarantee the exact cancellation of the divergences.

Within the light-front dynamics, a number of non-perturbative renormalization schemes have been proposed, including notably, the similarity renormalization group procedure [68, 69, 148], the sector dependent renormalization [36, 35, 119, 149, 150] and the Taylor-Lagrange renormalization [151]. A partial list with brief introductions can be found in Ref. [17] and the

references therein. In this chapter, we investigate a very promising non-perturbative renormalization scheme, the Fock Sector Dependent Renormalization (FSDR). This renormalization scheme was first introduced by Perry, Harindranath and Wilson [36], subsequently employed by Hiller and Brodsky [119], and developed into a systematic approach by Karmanov, Mathiot and Smirnov [35, 149, 150].

Fock Sector Dependent Renormalization possesses several advantages. First, it is based on the Fock sector truncation (aka. the Light-Front Tamm-Dancoff). As mentioned in Sect. 1.6, Fock sector truncation is a natural truncation scheme within light-front dynamics and many non-perturbative methods are based on it. As such, FSDR can be widely applied. Second, it is a systematic renormalization scheme that works for general truncated Fock sectors. In this way, the non-perturbative calculation can be systematically improved by including higher Fock sectors. Third, FSDR ensures the exact cancellation of the divergences in the non-perturbative regime. Fourth, FSDR is also consistent with the perturbative renormalization scheme.

FSDR has been successively applied to the Yukawa model [150] and QED [35, 119] up to three-body (one fermion plus two bosons) truncation in the non-perturbative regime. Then, a natural question to ask is whether the light-front Tamm-Dancoff approach equipped with FSDR converges as the number of Fock sectors increases. If so, it constitutes a genuine *ab initio* approach to quantum field theories in Minkowski space. This question, however, is not easy to address analytically. In practice, we can compare results from successive Fock sector truncations and check numerically whether they converge.

In this chapter, we demonstrate this procedure in a non-perturbative scalar Yukawa model. The main results of this chapter are based on research work done by the author and collaborators [152, 153]. In this simple but non-trivial model, we apply the FSDR up to four-body (one complex scalar and three real scalars) truncation and compare the electromagnetic form factors obtained from successive truncations. As we will see, numerical convergence is observed in the non-perturbative regime. Similar investigations for the Fock sector convergence can be found in Refs. [154, 155] in the context of the Wick-Cutkosky model [156, 157].

3.1 Scalar Yukawa Model

The Lagrangian of the scalar Yukawa model reads,

$$\mathscr{L}_{\rm Y} = \partial_\mu \chi^\dagger \partial^\mu \chi - m^2|\chi|^2 + \tfrac{1}{2}\partial_\mu\varphi\partial^\mu\varphi - \tfrac{1}{2}\mu^2\varphi^2 + g_{\rm B}|\chi|^2\varphi + \delta m^2|\chi|^2 + \delta\mu^2\varphi^2, \tag{3.1}$$

where $g_{\rm B}$ is the bare coupling. The physical coupling is denoted as g. m and μ are the physical masses of particles associated with the charged and neutral scalar field χ and φ, respectively. For the present study, we tentatively assign them values $m = 0.94\,\text{GeV}$ and $\mu = 0.14\,\text{GeV}$, corresponding to the masses of the nucleon and the pion, respectively. For convenience, we shall call the Fock space constituent particles "chion" (particle associated with χ) and "phion" (particle associated with φ), respectively. $\delta m^2 = m^2 - m_{\rm B}^2$ is the mass counterterm of the chion. $\delta\mu = \mu^2 - \mu_{\rm B}^2$ is the mass counterterm of the phion. It is convenient to introduce a dimensionless coupling constant[1],

$$\alpha = \frac{g^2}{16\pi m^2}. \tag{3.2}$$

This theory in super-renormalizable[2] in the (3+1) dimensions. However, it still contains ultraviolet (UV) divergences in the self energy. We introduce a Pauli-Villars (PV) phion field with mass $\mu_{\rm PV}$ to regularize the UV divergence [158].

The cubic interaction is known to exhibit vacuum instability [159]. Without introducing additional parameters (such as quartic terms), we suppress the anti-chion degrees-of-freedom [160], which is sometimes known as the "quenched theory" or "quenched approximation", as this procedure excludes all chion loops[3]. It should be emphasized, though, the FSDR is fully capable of dealing with anti-particle degrees of freedom [150]. Then the bare mass of the phion equals its physical mass $\mu_{\rm B} = \mu$.

[1] The dimensionless coupling constant α is related to the Yukawa potential between two chions (tree-level) by,

$$\phi(r) = -\alpha\frac{e^{-\mu r}}{r}.$$

[2] A super-renormalizable theory is a theory with only a finite number of Feynman diagrams superficially diverge [18]. In the case of the scalar Yukawa model, the only divergence occurs in the 1-loop correction, and vertex corrections are finite.

[3] In addition to chion loops, this procedure also excludes the Z-diagrams and more. Therefore, it is not exactly the same as the usual "quenched theory" defined from the Path Integral approach.

We adopt the Light-Front Tamm-Dancoff coupled integral equation approach to solve the non-perturbative dynamics (see Sect. 1.6.1). The coupled integral equations come from the Fock space representation of the eigenvalue equation Eq. (1.19). We solve the eigenvalue equation for the ground state in the one-chion (charge-one) sector, which involves the renormalization of the physical particle (denoted as $\mathcal{X}$). The solution produces the non-perturbative vertex functions $\Gamma_{\mathcal{X}/\chi}, \Gamma_{\mathcal{X}/\chi\varphi}, \Gamma_{\mathcal{X}/\chi\varphi\varphi}, \cdots, \Gamma_{\mathcal{X}/\chi\varphi^n}$, whose relation with the LFWFs is,

$$\Gamma^{j_1 j_2 \cdots j_n}_{\mathcal{X}/\chi\varphi^n}(p, k_1, k_2, \cdots, k_n; P, j, m_j) \equiv (s_{n+1} - M^2)\psi^{j_1 j_2 \cdots j_n}_{\mathcal{X}/\chi\varphi^n}(p, k_1, k_2, \cdots, k_n; P, j, m_j), \quad (3.3)$$

where $M^2 = P^2$ is the mass of the physical particle $\mathcal{X}$, and j_a $(a = 1, 2, \cdots n)$ are the indices denoting the normal phions ($j_a = 0$) or the Pauli-Villars phions ($j_a = 1$). j and m_j are the spin and spin projection of the physical particle, respectively. The Fock state invariant mass squared is,

$$s_{n+1} \equiv (p + k_1 + k_2 + \cdots + k_n)^2 = \frac{\boldsymbol{p}_\perp^2 + m^2}{x} + \sum_{i=1}^{n} \frac{\boldsymbol{k}_{i\perp}^2 + \mu_{j_i}^2}{x_i} - \boldsymbol{P}_\perp^2. \quad (3.4)$$

The momenta are constrained by the longitudinal and transverse momentum conservations:

$$\boldsymbol{p}^\perp + \boldsymbol{k}_1^\perp + \cdots + \boldsymbol{k}_n^\perp = \boldsymbol{P}^\perp, \quad p^+ + k_1^+ + \cdots + k_n^+ = P^+. \quad (3.5)$$

In the Hamiltonian formulation, there is no light-front energy conservation[4], but each momentum is on its mass shell: $p^2 = m^2$, $k_i^2 = \mu_{j_i}^2$, where we define $\mu_0 \equiv \mu$ and $\mu_1 \equiv \mu_{\rm PV}$ for convenience.

For this particular problem, the renormalization of the physical chion $\mathcal{X}$, the expression can be simplified: $M \to m, j \to 0, m_j \to 0$, and it is useful to use more specific notations rather than the most general ones. We shall denote,

$$\begin{aligned} \Gamma^{j_1 j_2 \cdots j_n}_{n+1}(\boldsymbol{k}_1^\perp, x_1, \boldsymbol{k}_2^\perp, x_2, \cdots, \boldsymbol{k}_n^\perp, x_n) &\equiv \Gamma^{j_1 j_2 \cdots j_n}_{\mathcal{X}/\chi\varphi^n}(p, k_1, k_2, \cdots, k_n; P, j, m_j) \\ \psi^{j_1 j_2 \cdots j_n}_{n+1}(\boldsymbol{k}_1^\perp, x_1, \boldsymbol{k}_2^\perp, x_2, \cdots, \boldsymbol{k}_n^\perp, x_n) &\equiv \psi^{j_1 j_2 \cdots j_n}_{\mathcal{X}/\chi\varphi^n}(p, k_1, k_2, \cdots, k_n; P, j, m_j). \end{aligned} \quad (3.6)$$

Here P $(P^2 = m^2)$, $j = 0$ and $m_j = 0$ are dropped. The momentum of the constituent chion, $(\boldsymbol{p}_\perp, x)$, has been suppressed, as it can be obtained from the momentum conservation Eq. (3.5).

[4]The Hamiltonian is defined for fixed light-front time. According to uncertainty principle, the light-front energy fluctuates.

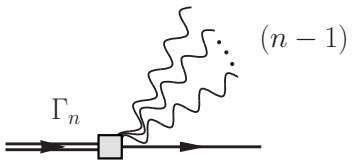

Figure 3.1: The diagrammatic representation of the n-body vertex function Γ_n.

We have also taken $\boldsymbol{P}_\perp = 0$ and $P^+ = 1$ by virtue of light-front boost invariance, and the Fock state invariant mass squared becomes,

$$s_{n+1} = \sum_{i=1}^{n} \frac{\boldsymbol{k}_{i\perp}^2 + \mu_{j_i}^2}{x_i} + \frac{(\boldsymbol{k}_1^\perp + \cdots + \boldsymbol{k}_n^\perp)^2 + m^2}{1 - x_1 \cdots - x_n}. \tag{3.7}$$

Occasionally, it is useful to study the P^2 dependence of the LFWFs and the vertex functions[5]. In those cases, we will add the P^2 back as,

$$\Gamma_{n+1}^{j_1 j_2 \cdots j_n}(\boldsymbol{k}_1^\perp, x_1, \boldsymbol{k}_2^\perp, x_2, \cdots, \boldsymbol{k}_n^\perp, x_n; P^2), \quad \psi_{n+1}^{j_1 j_2 \cdots j_n}(\boldsymbol{k}_1^\perp, x_1, \boldsymbol{k}_2^\perp, x_2, \cdots, \boldsymbol{k}_n^\perp, x_n; P^2). \tag{3.8}$$

We will also rely on the diagrammatic representation of the coupled integral equations for vertex functions. The diagram for the n-body vertex function is shown in Fig. (3.1). The solid line represents the constituent chion and the doubled solid line the physical chion. The wavy lines stand for the constituent phions. We use the shaded square to symbolize the non-perturbative vertex function. For a review of the diagrammatic representation, see Ref. [34].

3.2 Fock Sector Dependent Renormalization

3.2.1 Counterterms

Renormalization usually starts with the identification of counterterms. In FSDR, such an identification is based on the covariant formulation of light-front dynamics [34]. The result is similar with that of the light-front Hamiltonian renormalization group approach [66, 68, 117]. A distinguished feature of FSDR is that it allows the counterterms to be dependent on the truncation of the Fock sector and the spectators within the Fock sector in which the counterterms reside[6]. As we will see, the use of sector-dependent counterterms ensures the exact

[5] These off-mass-shell amplitudes typically appear as sub-diagrams of a larger diagram.

[6] One might be concerned that the explicit Fock-sector dependence of counterterms violates locality. Perry *et al.* argues that the sector dependence is needed to compensate for the non-localities introduced by the Fock sector truncation [36].

cancellation of the sub-divergences. This is also in direct analogy with the Forest Formula in perturbation theory [161], where the counterterms depend on the order of the coupling of the sub-diagrams.

Consider the non-perturbative self energies and their respective counterterms that appear in an N-body ($N-1$ "phions" plus 1 "chion") truncation, shown in Figs. 3.2a–3.2c. Γ_{a-c} are the non-perturbative vertex functions that sum all contributions allowed by the Fock sector truncation. As such the non-perturbative self-energy diagram in Figs. 3.2a contains all 1-loop diagrams as well as 2-loop diagrams, whereas the self-energy diagram in Figs. 3.2b does not contain any 2-loop diagrams. Therefore, the two corresponding mass counterterms δm_a^2 and δm_b^2 must be different to cancel the two different divergence structures. When the Fock sector truncation is lifted to four-body as shown in Fig. 3.2c, 2-loop diagrams appear in the self-energy diagram even with the presence of the spectator. Then, we conclude that $\delta m_a^2 = \delta m_c^2$, as the divergence structure is exactly the same. Most importantly, the difference between these non-perturbative self energies are completely determined by the Fock sector truncation and the residence of the spectators. It is in this regards that the counterterms must depend on the Fock sector truncation and the residence of the spectators.

Following the spirit of the above analysis, we introduce the general sector dependent counterterms (see Fig. 3.3). In the $(\chi + n\varphi)$ truncation, the mass counterterm associated with l phion spectators is defined as δm^2_{n-l+1}. Similarly, the bare coupling associated with l phion spectators before (for the emission vertex) or after (for the absorption vertex) the vertex, is defined as $g_{\mathrm{B}(n-l+1)}$. Note that the number of spectators $0 \leq l \leq n$. Hence, there are $(n+1)$ possible mass counterterms, δm_1^2, δm_2^2, ..., δm^2_{n+1}. The first n mass counterterms also appear in the $(\chi+(n-1)\varphi)$ truncation. If $l = n$, there is no phion available to dress the chion, so $\delta m_1^2 = 0$. By induction, therefore, all but δm^2_{n+1} needs to be determined from the $(\chi + n\varphi)$ truncation. Similarly, there are $(n+1)$ bare couplings involved in the $(\chi+n\varphi)$ truncation, $g_{\mathrm{B}1} = 0$, and only $g_{\mathrm{B}(n+1)}$ needs to be determined in this truncation. Therefore, we have developed a recursive program for calculating the sector-dependent counterterms.

Another renormalization parameter is I_1, the one-body norm[7] (also known as the wavefunc-

[7] In the Hamiltonian approach, we do not normalize the one-body component to unity, unlike that in pertur-

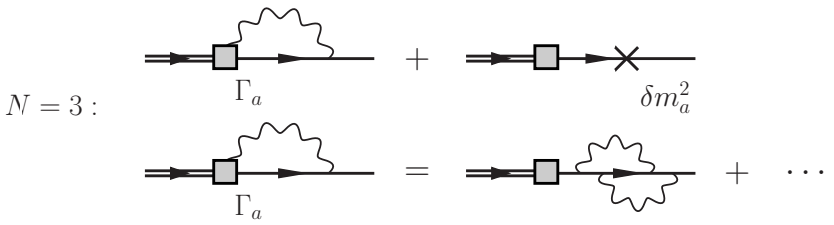

(a) A non-perturbative self-energy diagram and its mass counterterm appearing in the three-body ($N = 3$, two "phions" plus one "chion") Fock sector truncation. A typical 2-loop diagram contributing to this self-energy is shown in the bottom panel.

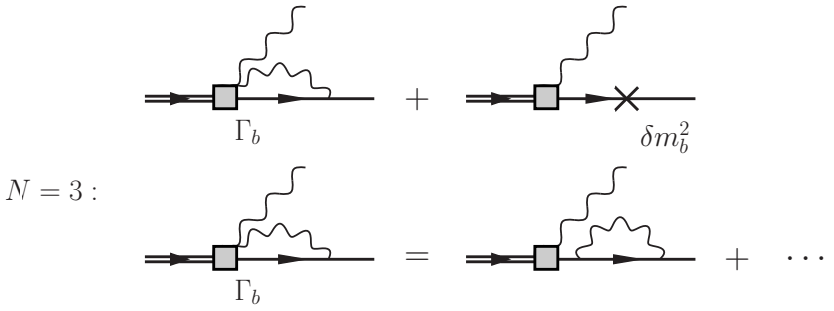

(b) Similar to (a), but with a spectator phion. Now this self-energy does not include any 2-loop diagrams, as they violate the Fock sector truncation.

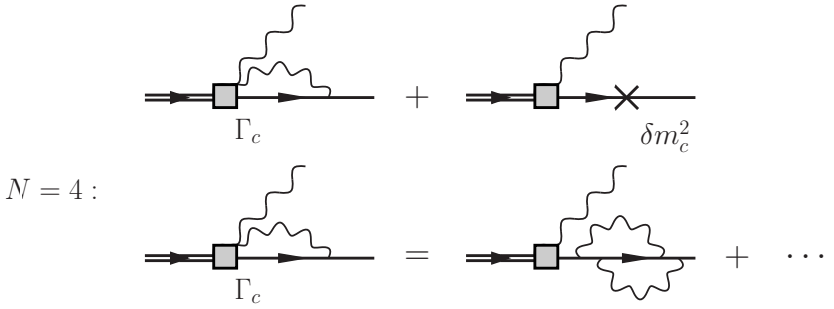

(c) Similar to (b), but in the four-body ($N = 4$, three "phions" plus one "chion") truncation. This self-energy does include 2-loop diagrams, as allowed by the Fock sector truncation.

Figure 3.2: A perturbative interpretation of the Fock sector dependence for mass counterterms.

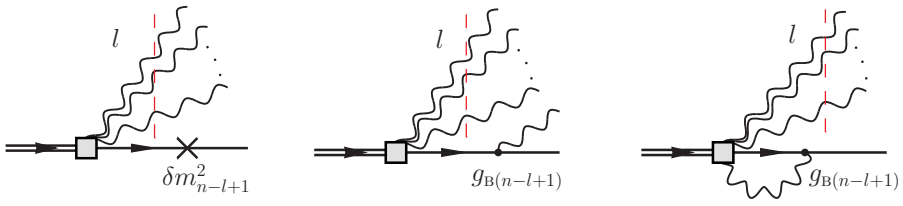

Figure 3.3: The general Fock sector dependent counterterms. n is the maximum number of dressing bosons allowed by the truncation. The spectator phions are intersected by the dashed lines. The number of spectators is l.

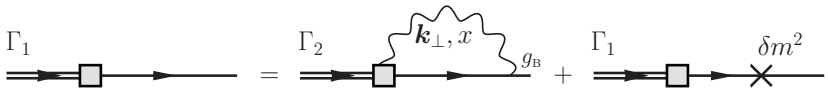

Figure 3.4: The one-body component of the eigenvalue equation.

tion renormalization constant, the field strength renormalization constant). It also depends on the Fock sector truncation, $I_1 \to I_1^{(N)}$ for the N-body truncation, and $I_1^{(1)} = 1$. A closely related quantity is the residue of the dressed propagator,

$$Z_\chi = \frac{\partial}{\partial p^2}\Sigma(p^2)\big|_{p^2\to m^2}, \tag{3.9}$$

where $\Sigma(p^2)$ is the self-energy function. This quantity acquires sector dependence, $Z_\chi \to Z_\chi^{(N)}$ for the N-body truncation, through the self-energy function (see below Eq. (3.13)). In perturbation theory, $Z_\chi = I_1$ up to higher order of the coupling. However, this may not be true, in general, within a truncated Fock space in non-perturbative approaches. It has been proven that if rotational symmetry is properly restored by renormalization,

$$Z_\chi^{(N)} \equiv I_1^{(N)}, \tag{3.10}$$

still holds in the non-perturbative regime [149]. This condition can be used to test non-perturbative renormalization methods.

3.2.2 Renormalization conditions

The mass renormalization condition follows from the one-body component of the eigenvalue equation (see Fig. 3.4),

$$\Gamma_1 = \sum_{j=0}^{1}(-1)^j \int_0^1 \frac{\mathrm{d}x}{2x(1-x)} \int \frac{\mathrm{d}^2k_\perp}{(2\pi)^3}\, g_{\rm B}\, \psi_2^j(\boldsymbol{k}_\perp, x) + \delta m^2 \psi_1. \tag{3.11}$$

Eq. (3.11) holds true for any truncation. So we have suppressed the index indicating the truncation for now. From Eq. (3.3), the one-body vertex function $\Gamma_1 = (m^2 - M^2)\psi_1 \to 0$ as we put $M \to m$. The one-body LFWF is a constant and is related to the one-body normalization constant: $I_1 = \psi_1^2$. Then, Eq. (3.11) becomes,

$$\delta m^2 = -\psi_1^{-1} \sum_{j=0}^{1}(-1)^j \int_0^1 \frac{\mathrm{d}x}{2x(1-x)} \int \frac{\mathrm{d}^2k_\perp}{(2\pi)^3}\, g_{\rm B}\, \psi_2^j(\boldsymbol{k}_\perp, x). \tag{3.12}$$

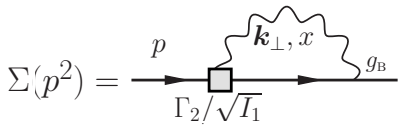

Figure 3.5: The non-perturbative self-energy $\Sigma(p^2)$.

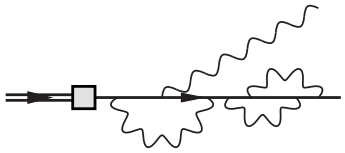

Figure 3.6: A typical diagram contributing to the two-body vertex Γ_2.

This can be generalized to the off-shell self energy (see Fig. 3.5),

$$\Sigma(p^2) = -\psi_1^{-1}(p^2)\sum_{j=0}^{1}(-1)^j\int\frac{\mathrm{d}^2k_\perp}{(2\pi)^3}\int_0^1\frac{\mathrm{d}x}{2x(1-x)}\,g_{\rm B}\,\psi_2^j(\boldsymbol{k}_\perp,x;p^2), \tag{3.13}$$

where $\psi_1(p^2)$ and $\psi_2(\boldsymbol{k}_\perp,x;p^2)$ are the off-shell LFWFs, and $\psi_1(p^2=m^2)=\psi_1$, $\psi_2(\boldsymbol{k}_\perp,x;p^2=m^2)=\psi_2(\boldsymbol{k}_\perp,x)$. So $\Sigma(m^2)=\delta m^2$.

The coupling constant renormalization condition[8] can be obtained from analyzing the structure of the two-body vertex function Γ_2 [149] (see Fig. 3.6). The resultant (on-shell) coupling constant renormalization condition is,

$$\Gamma^{j=0}_{\mathcal{X}/\chi\varphi}(p^\star,k^\star;P,j,m_j) = g\sqrt{Z_\chi}, \qquad \Big((p^\star+k^\star)^2=m^2, P^2=m^2\Big) \tag{3.14}$$

$$\Gamma_2^{j=0}(\boldsymbol{k}_\perp^\star,x^\star) = g\sqrt{Z_\chi}, \qquad \Big(\frac{\boldsymbol{k}_\perp^{\star\,2}+\mu^2}{x^\star}+\frac{\boldsymbol{k}_\perp^{\star\,2}+m^2}{1-x^\star}=m^2\Big). \tag{3.15}$$

Here, $(p^\star+k^\star)^2=m^2$, or equivalently, $\frac{\boldsymbol{k}_\perp^{\star\,2}+\mu^2}{x^\star}+\frac{\boldsymbol{k}_\perp^{\star\,2}+m^2}{1-x^\star}=m^2$ is the so-called renormalization point, at which the renormalization condition is imposed. The factor Z_χ came from the self-energy correction on the chion leg (see Fig. 3.6). Note that the renormalization point cannot be achieved by a physical value of the momentum: $\boldsymbol{k}_\perp^{\star\,2}=-x^{\star 2}m^2-(1-x^\star)\mu^2<0$. We therefore have to approach the renormalization point through analytic continuation in $k_\perp^\star$. Moreover, due to the violation of Lorentz symmetry, the kinematic condition $\frac{\boldsymbol{k}_\perp^{\star\,2}+\mu^2}{x^\star}+\frac{\boldsymbol{k}_\perp^{\star\,2}+m^2}{1-x^\star}=m^2$ does not uniquely determine the renormalization point $(\boldsymbol{k}_\perp^\star,x^\star)$. Following [35, 149, 150], we

bation theory. Instead, we normalize the physical state vector to one.

[8] This is also known as the charge renormalization. But, in QED the term "charge renormalization" is often exclusively associated with the vacuum polarization, because the contributions from the self-energy and vertex corrections are canceled out due to the Ward-Takahashi Identity. The net effect, there, is vacuum polarization.

impose the renormalization condition on $(\boldsymbol{k}_\perp^\star, x)$ *for all physical* x $(0 \le x \le 1)$ that satisfies the kinematic condition $\frac{\boldsymbol{k}_\perp^{\star\,2}+\mu^2}{x} + \frac{\boldsymbol{k}_\perp^{\star\,2}+m^2}{1-x} = m^2$.

Within the N-body $(\chi + n\varphi,\, N = 1+n)$ truncated Fock space, the renormalization conditions shall be written as,

$$\delta m_{n+1}^2 = -1/\psi_1^{(n+1)} \sum_{j=0}^{1} (-1)^j \int_0^1 \frac{\mathrm{d}x}{2x(1-x)} \int \frac{\mathrm{d}k_\perp}{(2\pi)^3}\, g_{\mathrm{B}(n+1)}\, \psi_2^{j(n+1)}(\boldsymbol{k}_\perp, x), \tag{3.16}$$

$$\Gamma_2^{0(n+1)}(\boldsymbol{k}_\perp^\star, x) = g\sqrt{I_1^{(n)}}, \qquad \Big(\frac{\boldsymbol{k}^{\star 2}}{x} + \frac{\boldsymbol{k}^{\star 2}+\mu^2}{1-x} = m^2, \forall x \in (0,1)\Big). \tag{3.17}$$

Here we have replaced Z_χ by I_1 as they are identical, as mentioned. Note also that the sector-dependence in I_1 is n instead of $(n+1)$, due to the presence of the phion spectator (see Fig. 3.6). Finally, the wavefunction renormalization can be obtained from the normalization of wavefunctions within the truncated space:

$$\sum_{l=1}^{n+1} I_l^{(n+1)} \equiv \sum_{l=1}^{n+1} \sum_{j_1,\cdots,j_l} (-1)^{j_1+\cdots+j_l} \int D_l \left|\psi_l^{j_1\cdots j_l (n+1)}(\boldsymbol{k}_1^\perp, x_1, \cdots, \boldsymbol{k}_{l-1}^\perp, x_{l-1})\right|^2 = 1, \tag{3.18}$$

where D_l is the l-body Fock space volume element:

$$\int D_l = \frac{1}{l!} \int \frac{\mathrm{d}x_1}{2x_1} \int \frac{\mathrm{d}k_{1\perp}}{(2\pi)^3} \cdots \int \frac{\mathrm{d}x_l}{2x_l} \int \frac{\mathrm{d}k_{l\perp}}{(2\pi)^3} 4\pi\delta(x_1+\cdots+x_l-1)(2\pi)^2\delta^2(\boldsymbol{k}_1^\perp+\cdots+\boldsymbol{k}_l^\perp). \tag{3.19}$$

3.3 Truncation up to Two-Body $(\chi + \varphi)$

Now we are ready to solve the scalar Yukawa model within the truncated Fock space. Recall the sector-dependent counterterms are determined recursively. Therefore, even though our goal is to solve the four-body $(\chi + 3\varphi)$ problem, we would have to start with the lower sector truncations. Luckily, the amount of work required for the lower sector truncations is much smaller than the higher Fock sector truncations. We spend this section for solving the problem within the Fock sector truncation up to two- $(\chi + \varphi)$ and three-body $(\chi + 2\varphi)$. Previously, these problems was solved in Ref. [35] without using the FSDR method (but these previous approaches closely resemble the FSDR). Previously, systematic solutions with FSDR for the two- and three-body truncation is obtained in [162, 163].

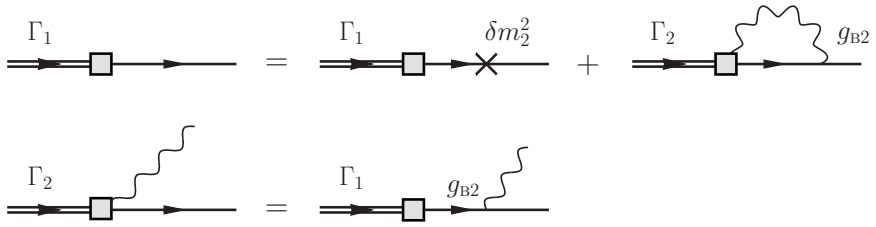

Figure 3.7: The diagrammatic representation of the eigenvalue equation within the two-body truncation.

The diagrams for the eigenvalue equation within the two-body truncation are shown in Fig. 3.7. The coupled integral equations are,

$$0 = \Gamma_1^{(2)} = \delta m_2^2 \psi_1^{(2)} + g_{\rm B2} \sum_{j=0}^{1} (-1)^j \int_0^1 \frac{\mathrm{d}x}{2x(1-x)} \int \frac{\mathrm{d}^2 k_\perp}{(2\pi)^3} \psi_2^{j(2)}(\boldsymbol{k}_\perp, x), \tag{3.20}$$

$$\Gamma_2^{j(2)}(\boldsymbol{k}_\perp, x) = g_{\rm B2}\, \psi_1^{(2)}. \tag{3.21}$$

Note that the second equation implies that $\Gamma_2^{0(2)}(\boldsymbol{k}_\perp, x) = \Gamma_2^{1(2)}(\boldsymbol{k}_\perp, x)$ is in fact a constant. Apply the coupling constant renormalization condition Eq. (3.17), noting $I_1^{(1)} = 1$,

$$\Gamma_2^{j(2)}(\boldsymbol{k}_\perp, x) = g, \tag{3.22}$$

$$\Longrightarrow \quad \psi_2^{j(2)}(\boldsymbol{k}_\perp, x) = \frac{g}{\frac{\boldsymbol{k}_\perp^2 + \mu_j^2}{x} + \frac{\boldsymbol{k}_\perp^2 + m^2}{1-x} - m^2}. \tag{3.23}$$

Apply the wavefunction normalization,

$$\left|\psi_1^{(2)}\right|^2 + \sum_{j=0}^{1} (-1)^j \int_0^1 \frac{\mathrm{d}x}{2x(1-x)} \int \frac{\mathrm{d}^2 k_\perp}{(2\pi)^3} \left|\psi_2^j(\boldsymbol{k}_\perp, x)\right|^2 = 1. \tag{3.24}$$

Then, the one-body LFWF reads[9],

$$\begin{aligned} I_1^{(2)} = \left|\psi_1^{(2)}\right|^2 =& 1 - \sum_{j=0}^{1} (-1)^j \int_0^1 \frac{\mathrm{d}x}{2x(1-x)} \int \frac{\mathrm{d}^2 k_\perp}{(2\pi)^3} \frac{g^2}{\left[\frac{\boldsymbol{k}_\perp^2 + \mu_j^2}{x} + \frac{\boldsymbol{k}_\perp^2 + m^2}{1-x} - m^2\right]^2} \\ =& 1 - \frac{\alpha}{\pi} \int_0^1 \mathrm{d}x \left[\frac{x(1-x)}{(1-x)\frac{\mu^2}{m^2} + x^2} - \frac{x(1-x)}{(1-x)\frac{\mu_{\rm PV}^2}{m^2} + x^2}\right] = 1 - I_2^{(2)}, \end{aligned} \tag{3.25}$$

where $\alpha = g^2/(16\pi m^2)$ is the dimensionless coupling constant. The integration in the second line can be expressed in terms of analytic functions.

[9] ψ_1 is only determined up to a relative phase. For here, we will fix the phase factor such that ψ_1 is real and positive.

Substitute Eq. (3.22–3.23) to Eq. (3.21–3.20), the bare coupling and the mass counterterm read,

$$g_{\text{B2}} = g/\sqrt{I_1^{(2)}} \tag{3.26}$$

$$\delta m_2^2 = \frac{\alpha}{\pi}\int_0^1 \mathrm{d}x\, \ln\left[\frac{(1-x)\mu_{\text{PV}}^2 + x^2m^2}{(1-x)\mu^2 + x^2m^2}\right] \times \frac{m^2}{I_1^{(2)}}. \tag{3.27}$$

Substituting the bare coupling and the mass counterterm back to the eigenvalue equation, we can obtain the off-shell amplitudes. In the two-body case, the eigenvalue does not change. As such the off-shell vertex function is identical to the on-shell one,

$$\Gamma_2^{j(2)}(\boldsymbol{k}_\perp, x; p^2) = g, \tag{3.28}$$

$$\implies \quad \psi_2^{j(2)}(\boldsymbol{k}_\perp, x; p^2) = \frac{g}{\frac{\boldsymbol{k}_\perp^2+\mu_j^2}{x} + \frac{\boldsymbol{k}_\perp^2+m^2}{1-x} - p^2}. \tag{3.29}$$

Then, the self-energy function, according to Eq. (3.13) is,

$$\Sigma^{(2)}(p^2) = \frac{\alpha}{\pi}\int_0^1 \mathrm{d}x\, \ln\left[\frac{(1-x)\mu^2 + xm^2 - x(1-x)p^2}{(1-x)\mu_{\text{PV}}^2 + xm^2 - x(1-x)p^2}\right] \times \frac{m^2}{I_1^{(2)}}. \tag{3.30}$$

With the obtain self-energy function, we are ready to check Eq. (3.10) at the two-body level. The Z-factor,

$$Z_\chi^{(2)} = \left[1 - \frac{\partial}{\partial p^2}\Sigma^{(2)}(p^2)\right]^{-1}_{p^2\to m^2} = \left[1 - (I_1^{(2)} - 1)/I_1^{(2)}\right]^{-1} = I_1^{(2)}, \tag{3.31}$$

as promised.

The theory contains a Landau pole in the large coupling region. From Eq. (3.25), $I_{1\text{–}2}^{(2)}$ are linear in α. There exists a critical coupling,

$$\alpha_{\text{L}}^{-1} \equiv \frac{1}{\pi}\int_0^1 \mathrm{d}x\, \frac{x(1-x)m^2}{(1-x)\mu^2 + x^2m^2}, \tag{3.32}$$

such that if $\alpha > \alpha_{\text{L}}$, $I_1^{(2)}$ becomes negative for some UV regulator μ_{PV} (the Landau pole [18]). The bare coupling g_{B2} becomes singular at α_{L} and imaginary beyond α_{L}. For $\mu = 0.14\,\text{GeV}$, and $m = 0.94\,\text{GeV}$, $\alpha_{\text{L}} \approx 2.6296$.

It should be pointed out that the results in the two-body truncation are equivalent to the leading order perturbation theory.

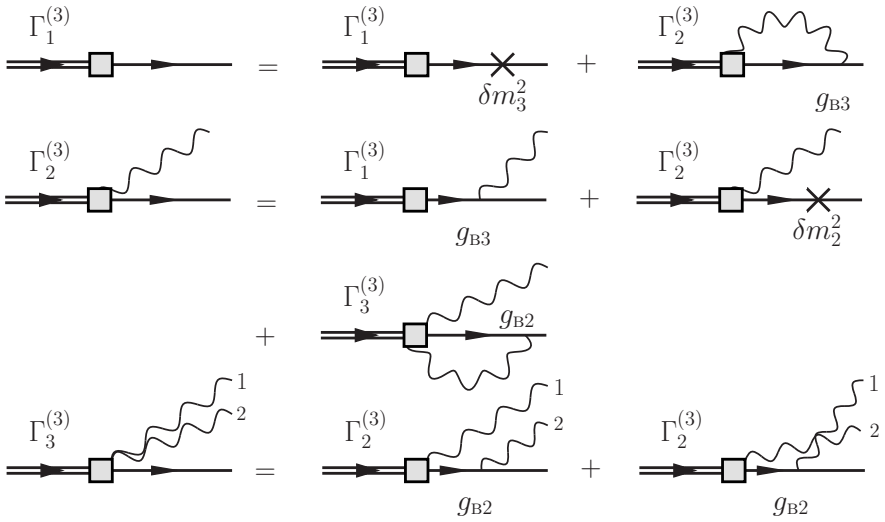

Figure 3.8: The diagrammatic representation of the eigenvalue equation within the three-body truncation.

3.4 Truncation up to Three-Body ($\chi + 2\varphi$)

3.4.1 Eigenvalue equation and renormalization

The diagrams for the eigenvalue equation within the three-body truncation are shown in Fig. 3.8. The coupled integral equations are,

$$\Gamma_1^{(3)} = \delta m_3^2 \psi_1^{(2)} + \sum_{j=0}^{1} (-1)^j \int_0^1 \frac{\mathrm{d}x}{2x(1-x)} \int \frac{\mathrm{d}^2 k_\perp}{(2\pi)^3}\, g_{B3}\, \psi_2^{j(3)}(\boldsymbol{k}_\perp, x) = 0, \tag{3.33}$$

$$\begin{aligned}\Gamma_2^{j(3)}(\boldsymbol{k}_\perp, x) &= g_{B3}\, \psi_1^{(3)} + \frac{\delta m_2^2}{1-x} \psi_2^{j(3)}(\boldsymbol{k}_\perp, x) \\ &\quad + g_{B2} \sum_{j'=0}^{1} (-1)^{j'} \int_0^{1-x} \frac{\mathrm{d}x'}{2x'(1-x-x')} \int \frac{\mathrm{d}^2 k'_\perp}{(2\pi)^3} \psi_3^{jj'(3)}(\boldsymbol{k}_\perp, x, \boldsymbol{k}'_\perp, x'),\end{aligned} \tag{3.34}$$

$$\Gamma_3^{jj'(3)}(\boldsymbol{k}_\perp, x, \boldsymbol{k}'_\perp, x') = \frac{g_{B2}}{1-x} \psi_2^{j(3)}(\boldsymbol{k}_\perp, x) + \frac{g_{B2}}{1-x'} \psi_2^{j'(3)}(\boldsymbol{k}'_\perp, x'). \tag{3.35}$$

Note that Γ_3 only depends on Γ_2. So, we can substitute Eq. (3.34) into Eq. (3.35), and get (see also Fig. (3.9)),

$$\begin{aligned}\left[1 - \frac{\Sigma^{(2)}(t) - \Sigma^{(2)}(m^2)}{t - m^2}\right] \Gamma_2^{j(3)}(\boldsymbol{k}_\perp, x) &= g_{B3}\, \psi_1^{(3)} \\ &\quad + g_{B2}^2 \sum_{j'=0}^{1} (-1)^{j'} \int_0^{1-x} \frac{\mathrm{d}x'}{2x'(1-x')(1-x-x')} \int \frac{\mathrm{d}^2 k'_\perp}{(2\pi)^3} \frac{1}{s_3 - m^2} \psi_2^{j'(3)}(\boldsymbol{k}'_\perp, x'),\end{aligned} \tag{3.36}$$

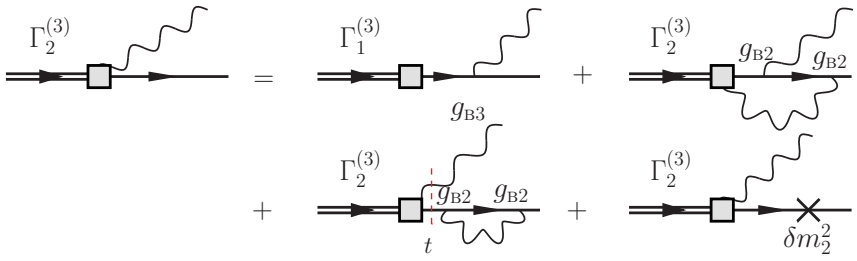

Figure 3.9: The diagrammatic representation of the system of equations for Γ_2 within the three-body truncation.

where $t = m^2 - (1-x)\Big(\frac{\boldsymbol{k}_\perp^2+\mu_j^2}{x} + \frac{\boldsymbol{k}_\perp^2+m^2}{1-x} - m^2\Big)$, $s_3 = \frac{\boldsymbol{k}_\perp^2+\mu_j^2}{x} + \frac{\boldsymbol{k}_\perp'^2+\mu_{j'}^2}{x'} + \frac{(\boldsymbol{k}_\perp+\boldsymbol{k}_\perp')^2+m^2}{1-x-x'}$.

Apply the renormalization condition Eq. (3.17) on both sides of Eq. (3.36) for $j=0$,

$$g_{\rm B2} = g_{\rm B3}\,\psi_1^{(3)} + g_{\rm B2}^2 \sum_{j'=0}^{1}(-1)^{j'} \int_0^{1-x} \frac{{\rm d}x'}{2x'(1-x')(1-x-x')} \int \frac{{\rm d}^2k'_\perp}{(2\pi)^3} \frac{1}{s_3^\star - m^2} \psi_2^{j'(3)}(\boldsymbol{k}'_\perp, x'), \tag{3.37}$$

where $s_3^\star = \frac{\boldsymbol{k}_\perp^{\star\,2}+\mu^2}{x} + \frac{\boldsymbol{k}_\perp'^2+\mu_{j'}^2}{x'} + \frac{(\boldsymbol{k}_\perp^\star+\boldsymbol{k}'_\perp)^2+m^2}{1-x-x'}$. Here we have used the facts $t \overset{k_\perp\to k_\perp^\star}{\longrightarrow} m^2$ and $Z_\chi^{(2)} = I_1^{(2)}$, and $g_{\rm B2} = g/\sqrt{I_1^{(2)}}$.

We use Eq. (3.37) to cancel out $g_{\rm B3}\,\psi_1^{(3)}$ in Eq. (3.36), and get an integral equation for $\Gamma_2^{(3)}$:

$$\Big[1 - \frac{\Sigma^{(2)}(t) - \Sigma^{(2)}(m^2)}{t-m^2}\Big]\Gamma_2^{j(3)}(\boldsymbol{k}_\perp, x) = g_{\rm B2} +$$
$$g_{\rm B2}^2 \sum_{j'=0}^{1}(-1)^{j'} \int_0^{1-x} \frac{{\rm d}x'}{2x'(1-x')(1-x-x')} \int \frac{{\rm d}^2k'_\perp}{(2\pi)^3} \Big[\frac{1}{s_3 - m^2} - \frac{1}{s_3^\star - m^2}\Big] \frac{\Gamma_2^{j'(3)}(\boldsymbol{k}'_\perp, x')}{s_2' - m^2}, \tag{3.38}$$

where $t = m^2 - (1-x)\Big(\frac{\boldsymbol{k}_\perp^2+\mu_j^2}{x} + \frac{\boldsymbol{k}_\perp^2+m^2}{1-x} - m^2\Big)$, $s_3 = \frac{\boldsymbol{k}_\perp^2+\mu_j^2}{x} + \frac{\boldsymbol{k}_\perp'^2+\mu_{j'}^2}{x'} + \frac{(\boldsymbol{k}_\perp+\boldsymbol{k}_\perp')^2+m^2}{1-x-x'}$, and $s_3^\star = \frac{\boldsymbol{k}_\perp^{\star\,2}+\mu^2}{x} + \frac{\boldsymbol{k}_\perp'^2+\mu_{j'}^2}{x'} + \frac{(\boldsymbol{k}_\perp^\star+\boldsymbol{k}'_\perp)^2+m^2}{1-x-x'}$ are defined as before, and $s_2' = \frac{\boldsymbol{k}_\perp'^2+\mu_{j'}^2}{x} + \frac{\boldsymbol{k}_\perp'^2+m^2}{1-x}$.

3.4.2 Numerical results

Equation (3.38) is an inhomogeneous linear coupled integral equation for Γ_2. We adopt an iterative method to solve this equation. First note that Γ_2 does not depend on the angle $\arg \boldsymbol{k}_\perp$, due to rotational symmetry. Therefore, the integrals can be reduced to two convolutions. We approximate the longitudinal and transverse radial integrals using Gauss-Legendre quadrature. More details on the numerical methods are presented in Sect. 3.5.

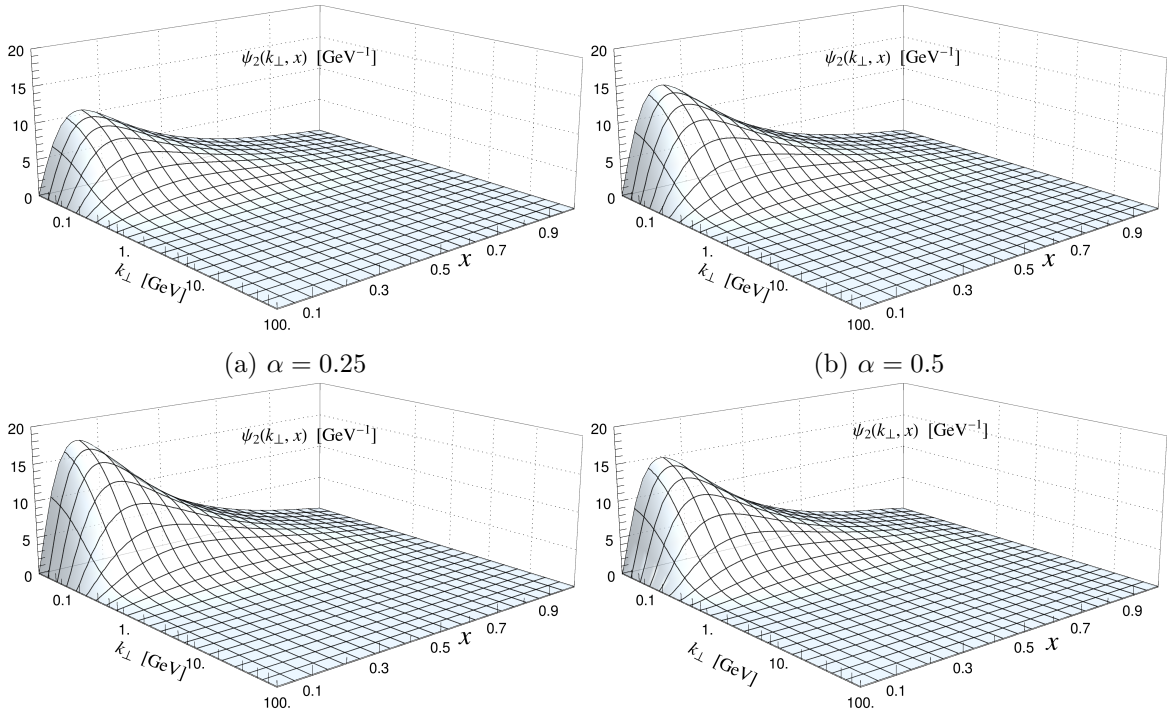

(a) $\alpha = 0.25$ (b) $\alpha = 0.5$

(c) $\alpha = 1.0$ (d) $\alpha = 2.0$

Figure 3.10: The physical ($j = 0$) two-body LFWF $\psi_2^{0(3)}(\boldsymbol{k}_\perp, x)$ at $\alpha = 0.25, 0.5, 1.0, 2.0$ from the three-body (χ+2φ) truncation. The Pauli-Villars mass has been taken to infinity, $\mu_{\rm PV} \to \infty$.

The obtained two-body LFWF $\psi_2^{j=0(3)}(\boldsymbol{k}_\perp, x)$ for selected coupling constants is shown in Fig. 3.10. To compare with the two-body (χ+φ) truncated results, we plot the physical ($j = 0$) vertex functions Γ_2 as a function of x in Fig. 3.11. In the two-body truncation, $\Gamma_2^{0(2)} = g$ is merely a constant (see Eq. (3.22)), represented by the horizontal lines in the figure. The plot shows that at small coupling, $\Gamma_2^{0(3)}(\boldsymbol{k}_\perp, x)$ is close to $\Gamma_2^{0(2)}(\boldsymbol{k}_\perp, x)$. As α increases, $\Gamma_2^{0(3)}(\boldsymbol{k}_\perp, x)$ developed non-trivial dependence on both x and $k_\perp$.

With the obtained two-body LFWF $\Gamma_2^{j(3)}(\boldsymbol{k}_\perp, x)$, the three-body LFWF $\Gamma_3^{jj'(3)}(\boldsymbol{k}_\perp, x, \boldsymbol{k}'_\perp, x')$ is given by Eq. (3.35). The one-body LFWF can be derived from the wavefunction normalization (see also Fig. 3.12),

$$\begin{aligned} 1 =& I_1^{(3)} + I_2^{(3)} + I_3^{(3)} \\ =& \left|\psi_1^{(3)}\right|^2 + \sum_{j=0}^{1}(-1)^j \int_0^1 \frac{\mathrm{d}x}{2x(1-x)} \int \frac{\mathrm{d}^2 k_\perp}{(2\pi)^3} \left|\psi_2^{j(3)}(\boldsymbol{k}_\perp, x)\right|^2 \\ &+ \frac{1}{2!}\sum_{j,j'=0}^{1}(-1)^{j+j'} \int_0^1 \frac{\mathrm{d}x}{2x} \int \frac{\mathrm{d}^2 k_\perp}{(2\pi)^3} \int_0^{1-x} \frac{\mathrm{d}x'}{2x'(1-x-x')} \int \frac{\mathrm{d}^2 k'_\perp}{(2\pi)^3} \left|\psi_3^{jj'(3)}(\boldsymbol{k}_\perp, x, \boldsymbol{k}'_\perp, x')\right|^2. \end{aligned} \tag{3.39}$$

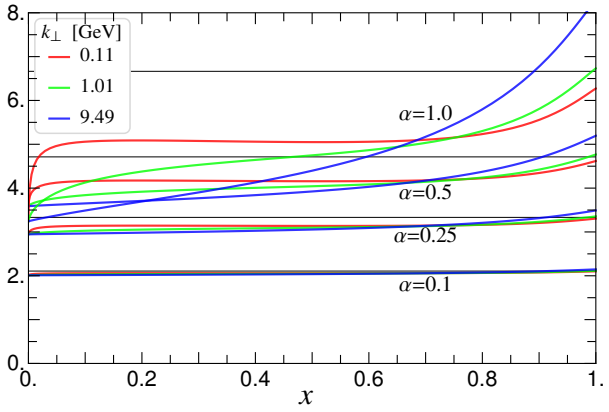

Figure 3.11: The physical ($j = 0$) two-body vertex function $\Gamma_2^{0(3)}(\boldsymbol{k}_\perp, x)$ at $\alpha = 0.1, 0.25, 0.5, 1.0$ from the three-body ($\chi + 2\varphi$) truncation. The Pauli-Villars mass has been taken to infinity, $\mu_{\rm PV} \to \infty$. The horizontal lines are the corresponding vertex functions at the two-body ($\chi + \varphi$) truncation $\Gamma_2^{0(2)}(\boldsymbol{k}_\perp, x) = g$, which are constant (see Eq. (3.22)).

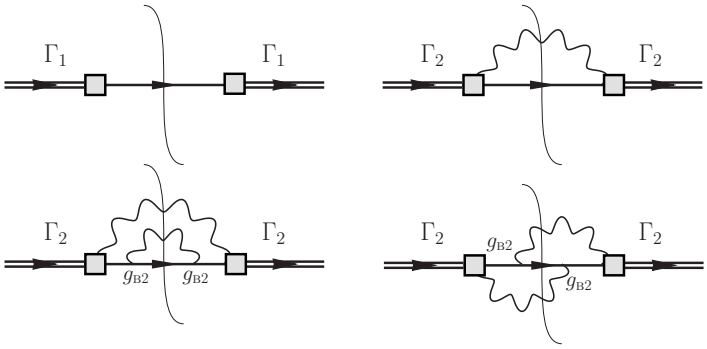

Figure 3.12: The diagrammatic representation of the normalization integrals Eq. (3.39). Here we have substituted Γ_3 with Γ_2 by Eq. (3.35).

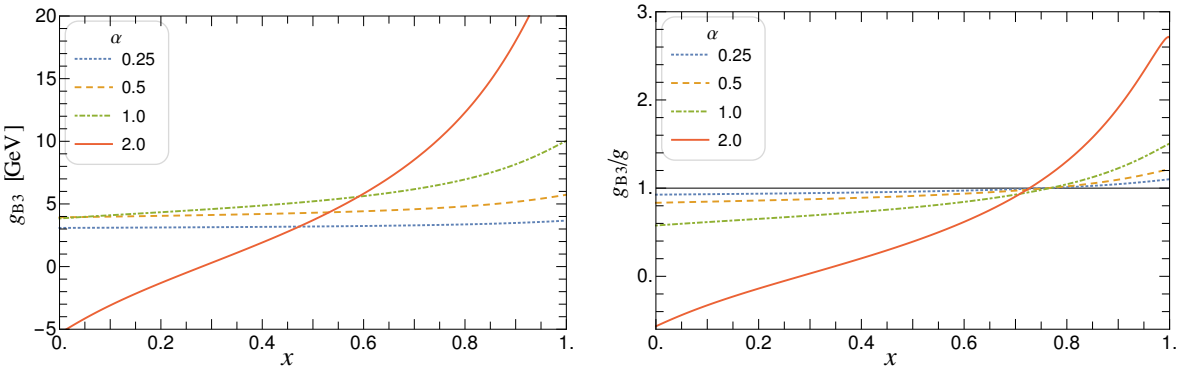

Figure 3.13: *Left*: The bare coupling g_{B3} as a function of x for $\alpha = 0.25, 0.5, 1.0, 2.0$. *Right*: The ratio g_{B3}/g as a function of x for $\alpha = 0.25, 0.5, 1.0, 2.0$. The Pauli-Villars mass has been taken to infinity, $\mu_{PV} \to \infty$.

Here the factor $\frac{1}{2!}$ accounts for the two identical particles (phions). Then the bare coupling g_{B3} is,

$$g_{B3}(x) = g_{B2}/\psi_1^{(3)} - g_{B2}^2/\psi_1^{(3)} \sum_{j'=0}^{1} (-1)^{j'} \int_0^{1-x} \frac{\mathrm{d}x'}{2x'(1-x')(1-x-x')} \int \frac{\mathrm{d}^2 k'_\perp}{(2\pi)^3} \frac{1}{s_3^\star - m^2} \psi_2^{j'(3)}(\boldsymbol{k}'_\perp, x'). \tag{3.40}$$

where $s_3^\star = \frac{\boldsymbol{k}_\perp^{\star\,2}+\mu_j^2}{x} + \frac{\boldsymbol{k}_\perp'^2+\mu_{j'}^2}{x'} + \frac{(\boldsymbol{k}_\perp^\star+\boldsymbol{k}'_\perp)^2+m^2}{1-x-x'}$. Note that the left-hand side expression depends on x. Therefore, the bare coupling g_{B3} has to be a function of x (see Fig. 3.13). Fig. 3.13 also reveals that the dependence grows as α increases. The x-dependence in the bare coupling is a consequence of the violation of the Lorentz symmetry by the Fock sector truncation. It has been shown[10] that including the anti-particle degree of freedom would dramatically reduce the x-dependence in the bare coupling [150].

The mass counterterm is given in Eq. (3.33), in terms of the obtained LFWFs,

$$\delta m_3^2 = -1/\psi_1^{(3)} \sum_{j=0}^{1} (-1)^j \int_0^1 \frac{\mathrm{d}x}{2x(1-x)} g_{B3}(x) \int \frac{\mathrm{d}^2 k_\perp}{(2\pi)^3} \psi_2^{j(3)}(\boldsymbol{k}_\perp, x). \tag{3.41}$$

3.4.3 Self-Energy function

We take the opportunity to introduce the three-body (χ+2φ) truncated self-energy function $\Sigma^{(3)}(p^2)$. With this self-energy function, we are able to evaluate the Z-factor and verify equality $I_1^{(n)} = Z_\chi^{(n)}$ at the three-body truncation level. This is a non-trivial task, as these two factors

[10] This conclusion can be easily seen from the perturbative perspective [163].

are obtained from different numerical procedures. As we will see in Sect. 3.5, the self-energy function is also useful for simplifying the problem in the four-body $(\chi + 3\varphi)$ truncation.

The self-energy function is defined as (Eq. (3.13)),

$$\begin{aligned}\Sigma^{(3)}(p^2) &= -1/\psi_1^{(3)}(p^2)\sum_{j=0}^{1}(-1)^j\int_0^1\frac{\mathrm{d}x}{2x(1-x)}g_{\mathrm{B}3}(x)\int\frac{\mathrm{d}^2k_\perp}{(2\pi)^3}\psi_2^{j(3)}(\boldsymbol{k}_\perp,x;p^2),\\ &\equiv -\sum_{j=0}^{1}(-1)^j\int_0^1\frac{\mathrm{d}x}{2x(1-x)}g_{\mathrm{B}3}(x)\int\frac{\mathrm{d}^2k_\perp}{(2\pi)^3}\overline{\psi}_2^{j(3)}(\boldsymbol{k}_\perp,x;p^2),\end{aligned}\tag{3.42}$$

where $\psi_1^{(3)}(p^2)$ and $\psi_2^{j(3)}(\boldsymbol{k}_\perp,x;p^2)$ are the off-the-mass shell LFWFs, and $\overline{\psi}_2^{j(3)}(\boldsymbol{k}_\perp,x;p^2)\equiv\psi_2^{j(3)}(\boldsymbol{k}_\perp,x;p^2)/\psi_1^{(3)}(p^2)$. It is also useful to define,

$$\overline{\Gamma}_2^{j(3)}(\boldsymbol{k}_\perp,x;p^2)\equiv\Gamma_2^{j(3)}(\boldsymbol{k}_\perp,x;p^2)/\psi_1^{(3)}(p^2)=(s_2-p^2)\overline{\psi}_2^{j(3)}(\boldsymbol{k}_\perp,x;p^2).\tag{3.43}$$

The off-shell LFWFs can be obtained from the eigenvalue equation Eq. (3.33–3.35) with the eigenvalue p^2.

$$\begin{aligned}\Gamma_2^{j(3)}(\boldsymbol{k}_\perp,x;p^2) &= g_{\mathrm{B}3}\,\psi_1^{(3)}(p^2)+\frac{\delta m_2^2}{1-x}\psi_2^{j(3)}(\boldsymbol{k}_\perp,x)\\ &\quad+g_{\mathrm{B}2}\sum_{j'=0}^{1}(-1)^{j'}\int_0^{1-x}\frac{\mathrm{d}x'}{2x'(1-x-x')}\int\frac{\mathrm{d}^2k'_\perp}{(2\pi)^3}\psi_3^{jj'(3)}(\boldsymbol{k}_\perp,x,\boldsymbol{k}'_\perp,x';p^2),\end{aligned}\tag{3.44}$$

$$\Gamma_3^{jj'(3)}(\boldsymbol{k}_\perp,x,\boldsymbol{k}'_\perp,x';p^2)=\frac{g_{\mathrm{B}2}}{1-x}\psi_2^{j(3)}(\boldsymbol{k}_\perp,x;p^2)+\frac{g_{\mathrm{B}2}}{1-x'}\psi_2^{j'(3)}(\boldsymbol{k}'_\perp,x';p^2).\tag{3.45}$$

Now in these equations, all bare couplings and mass counterterms are already known. Substitute Eq. (3.45) into Eq. (3.44),

$$\begin{aligned}&\Big[1-\frac{\Sigma^{(2)}(t)-\Sigma^{(2)}(m^2)}{t-m^2}\Big]\Gamma_2^{j(3)}(\boldsymbol{k}_\perp,x;p^2)=g_{\mathrm{B}3}\,\psi_1^{(3)}(p^2)\\ &\quad+g_{\mathrm{B}2}^2\sum_{j'=0}^{1}(-1)^{j'}\int_0^{1-x}\frac{\mathrm{d}x'}{2x'(1-x')(1-x-x')}\int\frac{\mathrm{d}^2k'_\perp}{(2\pi)^3}\frac{1}{s_3-p^2}\psi_2^{j'(3)}(\boldsymbol{k}'_\perp,x';p^2),\end{aligned}\tag{3.46a}$$

where $t=m^2-(1-x)\Big(\frac{\boldsymbol{k}_\perp^2+\mu_j^2}{x}+\frac{\boldsymbol{k}_\perp^2+m^2}{1-x}-p^2\Big)$, $s_3=\frac{\boldsymbol{k}_\perp^2+\mu_j^2}{x}+\frac{\boldsymbol{k}_\perp'^2+\mu_{j'}^2}{x'}+\frac{(\boldsymbol{k}_\perp+\boldsymbol{k}'_\perp)^2+m^2}{1-x-x'}$. Eq. (3.46) provides the off-shell amplitude $\overline{\psi}_2^{j(3)}(\boldsymbol{k}_\perp,x;p^2)$ needed for calculating the self-energy function Eq. (3.42).

$$\begin{aligned}&\Big[1-\frac{\Sigma^{(2)}(t)-\Sigma^{(2)}(m^2)}{t-m^2}\Big]\overline{\Gamma}_2^{j(3)}(\boldsymbol{k}_\perp,x;p^2)\\ &=g_{\mathrm{B}3}+g_{\mathrm{B}2}^2\sum_{j'=0}^{1}(-1)^{j'}\int_0^{1-x}\frac{\mathrm{d}x'}{2x'(1-x')(1-x-x')}\int\frac{\mathrm{d}^2k'_\perp}{(2\pi)^3}\frac{1}{s_3-p^2}\overline{\psi}_2^{j'(3)}(\boldsymbol{k}'_\perp,x';p^2).\end{aligned}\tag{3.46b}$$

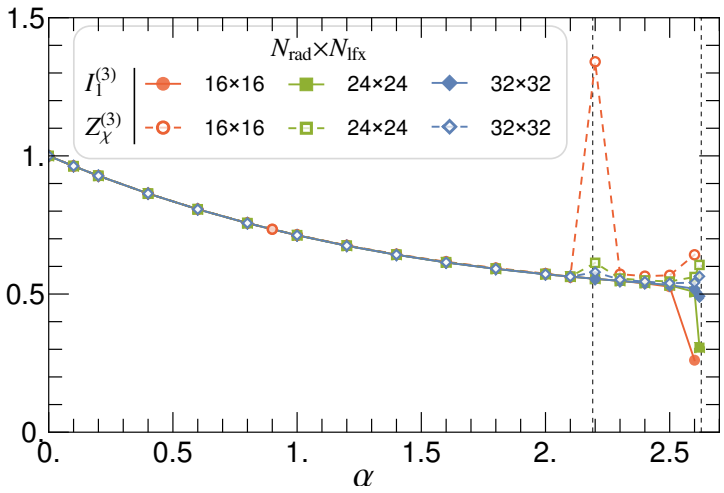

Figure 3.14: Numerical comparison of $I_1^{(3)}$ and $Z_\chi^{(3)}$ using various sizes of quadrature grid. The Pauli-Villars mass has been taken to infinity, $\mu_{\rm PV} \to \infty$. $N_{\rm rad}$ and $N_{\rm lfx}$ are the numbers of the quadrature points in the transverse radial and longitudinal directions, respectively. The two vertical lines indicate the locations of the Landau pole critical coupling $\alpha_{\rm L} \approx 2.63$ and a new critical coupling $\alpha_{\rm F} \approx 2.19$. The determinant of the kernel of the integral equation (3.46) crosses zero at $\alpha_{\rm F}$, which causes some numerical instability for small grids around this critical coupling.

In general, Eq.'s (3.46) may not have a solution for arbitrary p^2. For our purpose, as it will be seen, we only need the solution in the neighborhood of $p^2 = m^2$. The existence of the off-shell solution in this neighborhood can be assumed from the continuity of $\Sigma^{(3)}(p^2)$ at $p^2 = m^2$. To solve this equation, we first discretize it on a quadrature grid with $N_{\rm rad}$ transverse radial points and $N_{\rm lfx}$ longitudinal points. The integrals can be approximated by Gauss quadratures, and the integral equation becomes a linear equation problem. We then invert the matrix using standard numerical linear solver provided by the LAPACK software [123]. With the obtained solution, we calculate the Z-factor,

$$Z_\chi^{(3)} \equiv \left[1 - \frac{\partial \Sigma^{(3)}(p^2)}{\partial p^2}\right]^{-1}_{p^2=m^2.} \tag{3.47}$$

The resultant numerical results are plotted in Fig. 3.14 and compared with the numerical results of $I_1^{(3)}$. As is seen, these two quantities, evaluated from different numerical expression, agree with each other within the numerical precision.

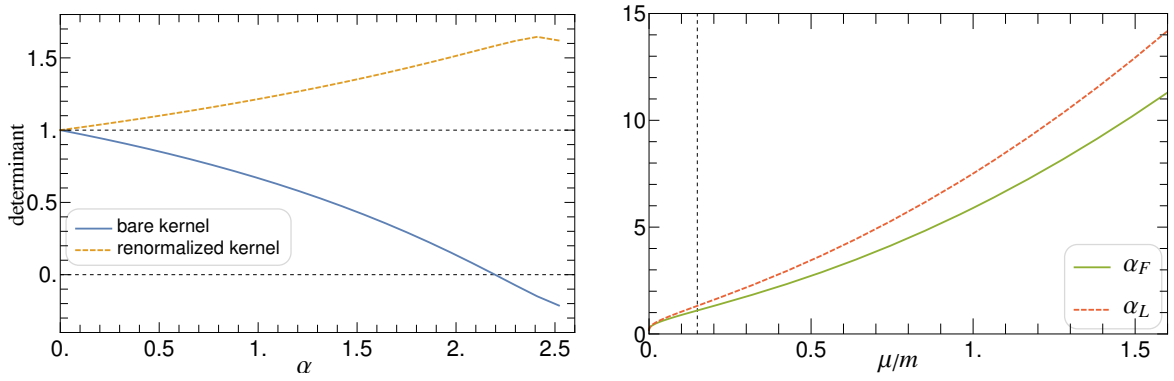

Figure 3.15: *Left*: The determinants of the bare (Eq. (3.36)) and the renormalized (Eq. (3.38)) kernels of the integral equations as a function of α for $\mu = 0.14\,\mathrm{GeV}$ and $m = 0.94\,\mathrm{GeV}$. The determinant of the bare kernel crosses zero at $\alpha_{\mathrm{F}} \approx 2.19$; *Right*: The critical couplings α_{F} and α_{L} for different mass ratios μ/m. The vertical dashed line on the right identifies $\mu/m = 0.14/0.94$, the value corresponding to many of the other results in this investigation, The results are evaluated on a quadrature grid with $N_{\mathrm{rad}} = 32$, $N_{\mathrm{lfx}} = 64\,(128)$.

3.4.4 Fredholm critical coupling

Equation (3.46), being an inhomogeneous linear coupled integral equation, can be solved using the iterative procedure similar to the one designed for solving Eq. (3.38). However, the determinant of the kernel of this integral equation[11] crosses zero at some coupling[12]. This is also true even for $p^2 \to m^2$, when Eq. (3.46) becomes Eq. (3.36) — the original eigenvalue equation. The determinants of Eq. (3.36) – the bare equation, and Eq. (3.38) – the renormalized equation – as a function of α are plotted in Fig. 3.15. It shows that the determinant of the kernel of Eq. (3.36) crosses zero at $\alpha_{\mathrm{F}} \approx 2.19$, for $\mu = 0.14\,\mathrm{GeV}$ and $m = 0.94\,\mathrm{GeV}$. Similar critical couplings exist for others mass parameters μ/m.

The difference of these two integral equations is that Eq. (3.36) explicitly depends on the bare parameter g_{B3} which are obtained from solving Eq. (3.38). One may naïvely expect that these two equations admit the same solution. It is true that each solution of Eq. (3.38) is also a solution of Eq. (3.36). However, at the Fredholm critical coupling α_{F}, Eq. (3.36) has more than one solutions, as a result of the vanishing determinant. A close inspection of the extra solutions reveals that the extra solutions are direct consequences of the x-dependence of g_{B3} [163].

[11] By the "determinant" of the kernel of an integral equation, we mean the determinant of the discretized matrix for the kernel. The determinant converges as the number of grid points increases.

[12] We shall called this critical coupling the Fredholm critical coupling, as the integral equations are the Fredholm integral equation of the second kind [164].

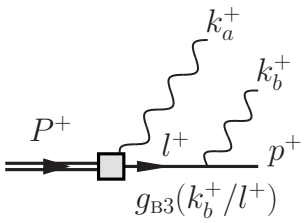

Figure 3.16: The three-body bare coupling $g_{\rm B3}$ depends only on the relative longitudinal momentum fraction $k_b^+/l^+ = x_b/(1-x_a)$, where $x_{a,b} = k_{a,b}^+/P^+$ is the longitudinal momentum fraction with respect to the whole system.

These are spurious solutions and do not satisfy the on-shell coupling constant renormalization condition Eq. (3.17). Therefore they are excluded from the solution of Eq. (3.38).

Similar analysis can be applied to the off-shell equation (3.46). But as we mentioned earlier, for the calculation of the Z-factor, we only need amplitudes around the mass shell. It can be derived that it involves the same kernel as Eq. (3.36). Fig. 3.14 also confirms that the critical coupling involved in the calculation of the Z-factor is at the same location as $\alpha_{\rm F} \approx 2.19$.

As we will see later that the Fredholm critical coupling also has impact on the solution of the four-body truncation. How to exclude the spurious solutions at the Fredholm critical coupling within the four-body truncation is still an open question.

3.5 Truncation up to Four-Body ($\chi + 3\varphi$)

3.5.1 Eigenvalue equation and renormalization

With the obtained bare couplings $g_{\rm B2}$, $g_{\rm B3}$ and mass counterterms δm_2^2, δm_3^2, we are ready to study the truncation up to four-body ($\chi+3\varphi$). A possible point of confusion is the x-dependent bare coupling $g_{\rm B3}$. Its argument should the *relative longitudinal momentum fraction*, i.e., the fraction of longitudinal momentum of the cluster where the emitting or absorbing phion is located (see Fig. 3.16).

The diagrammatic representation of the eigenvalue equation truncated up to four-body

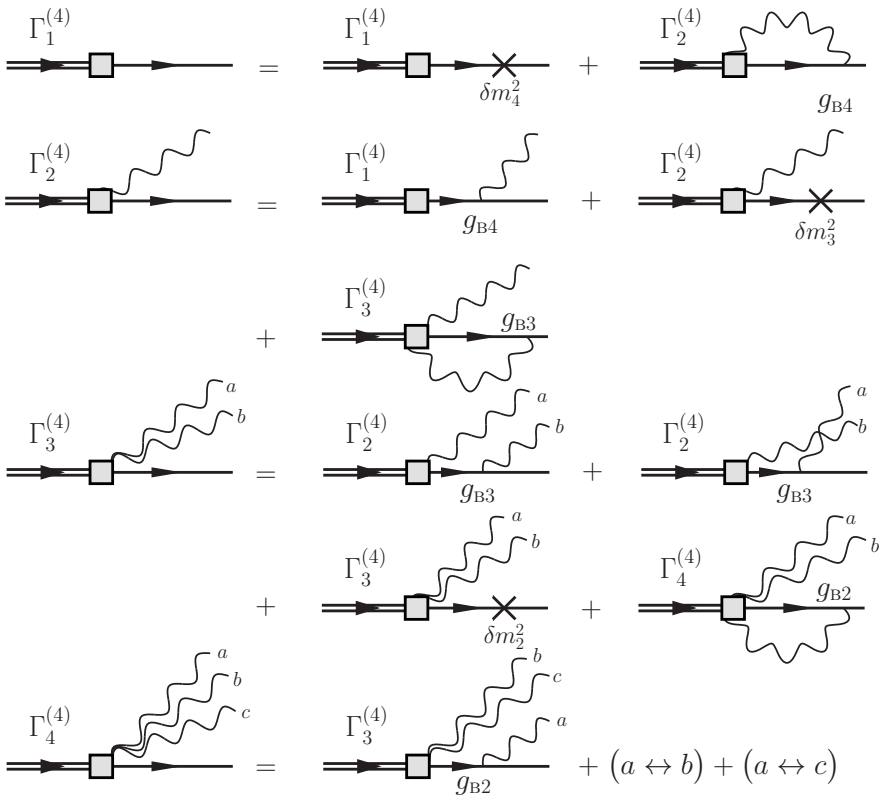

Figure 3.17: The diagrammatic representation of the eigenvalue equation within the four-body $(\chi + 3\varphi)$ truncation.

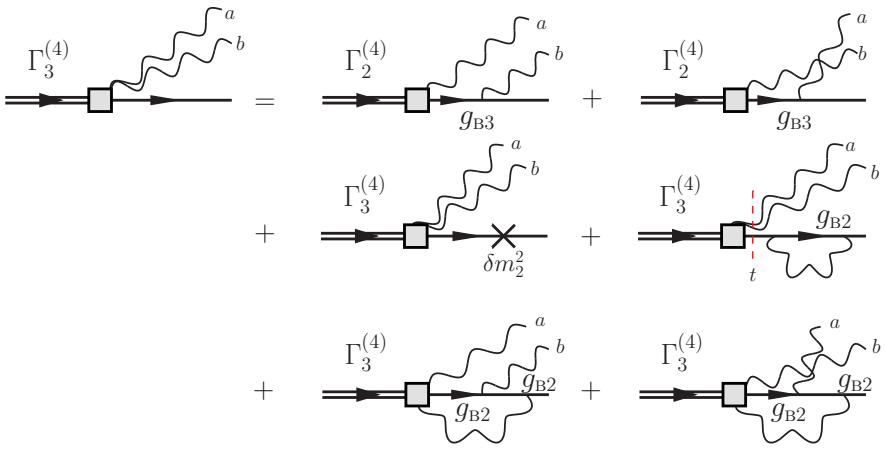

Figure 3.18: The diagrammatic representation of three-body component Γ_3, after substituting Eq. (3.51) into Eq. (3.50).

$(\chi + 3\varphi)$ is shown in Fig. 3.17. The coupled integral equations read,

$$\Gamma_1^{(4)} = \delta m_4^2\,\psi_1^{(4)} + \sum_{j=0}^{1}(-1)^j \int_0^1 \frac{\mathrm{d}x}{2x(1-x)} \int \frac{\mathrm{d}^2 k_\perp}{(2\pi)^3}\, g_{\rm B4}\, \psi_2^{j(4)}(\boldsymbol{k}_\perp, x) = 0, \tag{3.48}$$

$$\begin{aligned}\Gamma_2^{j(4)}(\boldsymbol{k}_\perp, x) &= g_{\rm B4}\,\psi_1^{(4)} + \frac{\delta m_3^2}{1-x}\psi_2^{j(4)}(\boldsymbol{k}_\perp, x) \\ &+ \sum_{j'=0}^{1}(-1)^{j'} \int_0^{1-x} \frac{\mathrm{d}x'}{2x'(1-x-x')} \int \frac{\mathrm{d}^2 k'_\perp}{(2\pi)^3}\, g_{\rm B3}\big(\tfrac{x'}{1-x}\big)\, \psi_3^{jj'(4)}(\boldsymbol{k}_\perp, x, \boldsymbol{k}'_\perp, x'),\end{aligned} \tag{3.49}$$

$$\begin{aligned}\Gamma_3^{j_a j_b(4)}(\boldsymbol{k}_{a\perp}, x_a, \boldsymbol{k}_{b\perp}, x_b) &= \frac{g_{\rm B3}\big(\frac{x_b}{1-x_a}\big)}{1-x_a}\psi_2^{j_a(4)}(\boldsymbol{k}_{a\perp}, x_a) \\ &+ \frac{g_{\rm B3}\big(\frac{x_a}{1-x_b}\big)}{1-x_b}\psi_2^{j_b(4)}(\boldsymbol{k}_{b\perp}, x_b) + \frac{\delta m_2^2}{1-x_a-x_b}\psi_3^{j_a j_b(4)}(\boldsymbol{k}_{a\perp}, x_a, \boldsymbol{k}_{b\perp}, x_b) \\ &+ g_{\rm B2}\sum_{j_a, j_b=0}^{1}(-1)^{j_a+j_b} \int_0^{1-x_a-x_b} \frac{\mathrm{d}x}{2x(1-x_a-x_b-x)} \int \frac{\mathrm{d}^2 k_\perp}{(2\pi)^3}\, \psi_4^{j_a j_b j(4)}(\boldsymbol{k}_{a\perp}, x_a, \boldsymbol{k}_{b\perp}, x_b, \boldsymbol{k}_\perp, x),\end{aligned} \tag{3.50}$$

$$\Gamma_4^{j_a j_b j_c(4)}(\boldsymbol{k}_{a\perp}, x_a, \boldsymbol{k}_{b\perp}, x_b, \boldsymbol{k}_{c\perp}, x_c) = g_{\rm B2}\frac{\psi_3^{j_b j_c(4)}(\boldsymbol{k}_{b\perp}, x_b, \boldsymbol{k}_{c\perp}, x_c)}{1-x_c-x_b} + (a \leftrightarrow b) + (a \leftrightarrow c). \tag{3.51}$$

$\Gamma_4^{(4)}$ depends only on $\Gamma_3^{(4)}$ via Eq. (3.51). Substitute Eq. (3.51) into Eq. (3.50),

$$\begin{aligned}\left(1 - \frac{\Sigma^{(2)}(t) - \Sigma^{(2)}(m^2)}{t-m^2}\right)\Gamma_3^{j_a j_b(4)}(\boldsymbol{k}_{a\perp}, x_a, \boldsymbol{k}_{b\perp}, x_b) &= \left[\frac{g_{\rm B3}\big(\frac{x_b}{1-x_a}\big)}{1-x_a}\psi_2^{j_a(4)}(\boldsymbol{k}_{a\perp}, x_a)\right. \\ \left. + g_{\rm B2}^2\sum_{j=0}^{1}(-1)^j \int_0^{1-x_a-x_b} \frac{\mathrm{d}x}{2x(1-x_a-x_b-x)(1-x_a-x)} \int \frac{\mathrm{d}^2 k_\perp}{(2\pi)^3}\, \frac{\psi_3^{j_a j(4)}(\boldsymbol{k}_{a\perp}, x_a, \boldsymbol{k}_\perp, x)}{s_4 - m^2}\right] &+ (a \leftrightarrow b),\end{aligned} \tag{3.52}$$

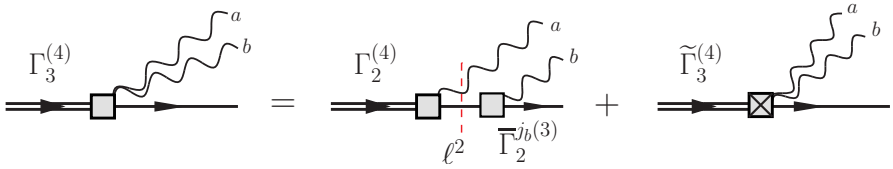

Figure 3.19: The diagrammatic representation of the decomposition Eq. (3.54). The first diagram sums over all diagrams with the mass pole $1/(s_2^\star - m^2)$ at $\boldsymbol{k}_{a\perp} \to \boldsymbol{k}_{a\perp}^\star$. The dashed vertical red line indicates the intermediate state with which the off-shell squared 4-momentum ℓ^2 is associated.

where $t = m^2 - (1-x_a-x_b)\Big(\frac{\boldsymbol{k}_{a\perp}^2+\mu_{ja}^2}{x_a} + \frac{\boldsymbol{k}_{b\perp}^2+\mu_{j_b}^2}{x_b} + \frac{(\boldsymbol{k}_{a\perp}+\boldsymbol{k}_{b\perp})^2+m^2}{1-x_a-x_b} - m^2\Big)$, and $s_4 = \frac{\boldsymbol{k}_{a\perp}^2+\mu_{ja}^2}{x_a} + \frac{\boldsymbol{k}_{b\perp}^2+\mu_{j_b}^2}{x_b} + \frac{\boldsymbol{k}_{\perp}^2+\mu_{j}^2}{x} + \frac{(\boldsymbol{k}_{a\perp}+\boldsymbol{k}_{b\perp}+\boldsymbol{k}_{\perp})^2+m^2}{1-x_a-x_b-x}$. The new bare coupling $g_{\rm B4}$ in Eq. (3.49) can be determined from the renormalization condition,

$$\Gamma_2^{0(4)}(\boldsymbol{k}_\perp^\star, x) = g\sqrt{I_1^{(3)}}, \qquad \Big(s_2^\star \equiv \frac{\boldsymbol{k}_\perp^{\star 2}+\mu^2}{x} + \frac{\boldsymbol{k}_\perp^{\star 2}+m^2}{1-x} = m^2\Big). \tag{3.53}$$

However, imposing Eq. (3.53) at the mass-shell to Eq. (3.49) gives two mass poles,

$$\psi_2^{0(4)}(\boldsymbol{k}_\perp^\star, x) = \frac{\Gamma_2^{0(4)}(\boldsymbol{k}_\perp^\star, x)}{s_2^\star - m^2} \sim \lim_{s_2^\star \to m^2} \frac{1}{s_2^\star - m^2}, \quad \psi_3^{0j'(4)}(\boldsymbol{k}_\perp^\star, x, \boldsymbol{k}'_\perp, x') \sim \lim_{s_2^\star \to m^2} \frac{1}{s_2^\star - m^2}.$$

These two singularities should cancel each other and produce a finite residue (the Z-factor), much like the three-body truncation case in Eq. (3.36–3.37). To facilitate the analytic cancellation, we introduce the following decomposition,

$$\Gamma_3^{j_a j_b(4)}(\boldsymbol{k}_{a\perp}, x_a, \boldsymbol{k}_{b\perp}, x_b) \equiv \frac{\overline{\Gamma}_2^{j_b(3)}(\boldsymbol{\kappa}_{b\perp}, \xi_b; \ell^2)}{1-x_a}\psi_2^{j_a(4)}(\boldsymbol{k}_{a\perp}, x_a) + \widetilde{\Gamma}_3^{j_a j_b(4)}(\boldsymbol{k}_{a\perp}, x_a, \boldsymbol{k}_{b\perp}, x_b), \tag{3.54}$$

$$\psi_3^{j_a j_b(4)}(\boldsymbol{k}_{a\perp}, x_a, \boldsymbol{k}_{b\perp}, x_b) \equiv \frac{\overline{\Gamma}_2^{j_b(3)}(\boldsymbol{\kappa}_{b\perp}, \xi_b; \ell^2)}{(1-x_a)(s_3-m^2)}\psi_2^{j_a(4)}(\boldsymbol{k}_{a\perp}, x_a) + \widetilde{\psi}_3^{j_a j_b(4)}(\boldsymbol{k}_{a\perp}, x_a, \boldsymbol{k}_{b\perp}, x_b) \tag{3.55}$$

where $\overline{\Gamma}_2^{j_b(3)}(\boldsymbol{\kappa}_{b\perp}, \xi_b; \ell^2) = \Gamma_2^{j_b(3)}(\boldsymbol{\kappa}_{b\perp}, \xi_b; \ell^2)/\psi_1^{(3)}(\ell^2)$ is defined in Eq. (3.43), and $\ell^2 = m^2 - (1-x_a)\big(\frac{\boldsymbol{k}_{a\perp}^2+\mu_{ja}^2}{x_a} + \frac{\boldsymbol{k}_{a\perp}^2+m^2}{1-x_a} - m^2\big)$, $\xi_b = x_b/(1-x_a)$, $\boldsymbol{\kappa}_{b\perp} = \boldsymbol{k}_{b\perp} + \xi_b \boldsymbol{k}_{a\perp}$, and $s_3 = \frac{\boldsymbol{k}_{a\perp}^2+\mu_{ja}^2}{x_a} + \frac{\boldsymbol{k}_{b\perp}^2+\mu_{j_b}^2}{x_b} + \frac{(\boldsymbol{k}_{a\perp}+\boldsymbol{k}_{b\perp})^2+m^2}{1-x_a-x_b}$. Note that $\overline{\Gamma}_2^{j_b(3)}(\boldsymbol{\kappa}_{b\perp}, \xi_b; \ell^2)$ is the off-shell vertex function in the three-body truncation, and is already known. The newly introduced pieces $\widetilde{\psi}_3^{0j_b(4)}(\boldsymbol{k}_{a\perp}, x_a, \boldsymbol{k}_{b\perp}, x_b)$ and $\widetilde{\Gamma}_3^{0j_b(4)}(\boldsymbol{k}_{a\perp}, x_a, \boldsymbol{k}_{b\perp}, x_b)$ will be regular when taking $\boldsymbol{k}_{a\perp} \to \boldsymbol{k}_{a\perp}^\star$ $\big(\frac{\boldsymbol{k}_{a\perp}^{\star 2}+\mu^2}{x} + \frac{\boldsymbol{k}_{a\perp}^{\star 2}+m^2}{1-x} = m^2\big)$. The decomposition is better understood from the diagrammatic representation in Fig. 3.19. The first term contains a non-perturbative vertex function $\Gamma_2^{(3)}$ that sums over all contributions

up to three-body. Then this term includes *all possible terms* that contain a mass pole at $\boldsymbol{k}_{a\perp} \to \boldsymbol{k}^\star_{a\perp}$.

Substitute Eq. (3.54) back into Eq.'s (3.49–3.52),

$$\left(1-\frac{\Sigma^{(3)}(\ell^2)-\Sigma^{(3)}(m^2)}{\ell^2-m^2}\right)\Gamma_2^{j(4)}(\boldsymbol{k}_\perp,x) = g_{\rm B4}\,\psi_1^{(4)} + \\ +\sum_{j'=0}^{1}(-1)^{j'}\int_0^{1-x}\frac{\mathrm{d}x'}{2x'(1-x-x')}\int\frac{\mathrm{d}^2k'_\perp}{(2\pi)^3}\,g_{\rm B3}(\tfrac{x'}{1-x})\,\widetilde{\psi}_3^{jj'(4)}(\boldsymbol{k}_\perp,x,\boldsymbol{k}'_\perp,x'), \tag{3.56}$$

$$\left(1-\frac{\Sigma^{(2)}(t)-\Sigma^{(2)}(m^2)}{t-m^2}\right)\widetilde{\Gamma}_3^{j_aj_b(4)}(\boldsymbol{k}_{a\perp},x_a,\boldsymbol{k}_{b\perp},x_b) = \frac{g_{\rm B3}(\frac{x_a}{1-x_b})}{1-x_b}\psi_2^{j_b(4)}(\boldsymbol{k}_{b\perp},x_b) \\ +g_{\rm B2}^2\sum_{j=0}^{1}(-1)^j\int_0^{1-x_a-x_b}\frac{\mathrm{d}x}{2x(1-x_a-x_b-x)(1-x_a-x)}\int\frac{\mathrm{d}^2k_\perp}{(2\pi)^3}\,\frac{1}{s_4-m^2} \\ \times\left[\widetilde{\psi}_3^{j_aj(4)}(\boldsymbol{k}_{a\perp},x_a,\boldsymbol{k}_\perp,x)+\psi_3^{j_bj(4)}(\boldsymbol{k}_{b\perp},x_b,\boldsymbol{k}_\perp,x)\right], \tag{3.57}$$

where $\ell^2 = m^2-(1-x)\big(\frac{\boldsymbol{k}_\perp^2+\mu_j^2}{x}+\frac{\boldsymbol{k}_\perp^2+m^2}{1-x}-m^2\big)$, $t = m^2-(1-x_a-x_b)\big(\frac{\boldsymbol{k}_{a\perp}^2+\mu_{ja}^2}{x_a}+\frac{\boldsymbol{k}_{b\perp}^2+\mu_{j_b}^2}{x_b}+\frac{(\boldsymbol{k}_{a\perp}+\boldsymbol{k}_{b\perp})^2+m^2}{1-x_a-x_b}-m^2\big)$, $s_4 = \frac{\boldsymbol{k}_{a\perp}^2+\mu_{ja}^2}{x_a}+\frac{\boldsymbol{k}_{b\perp}^2+\mu_{j_b}^2}{x_b}+\frac{\boldsymbol{k}_\perp^2+\mu_j^2}{x}+\frac{(\boldsymbol{k}_{a\perp}+\boldsymbol{k}_{b\perp}+\boldsymbol{k}_\perp)^2+m^2}{1-x_a-x_b-x}$ as defined before. Here, we have made use of the self-energy function introduced in Sect. 3.4.3. Applying the renormalization condition Eq. (3.53) for the $j=0$ component, Eq. (3.56) yields,

$$g/\sqrt{I_1^{(3)}} = g_{\rm B4}\psi_1^{(4)}+\sum_{j'=0}^{1}(-1)^{j'}\int_0^{1-x}\frac{\mathrm{d}x'}{2x'(1-x-x')}\int\frac{\mathrm{d}^2k'_\perp}{(2\pi)^3}g_{\rm B3}(\tfrac{x'}{1-x})\,\widetilde{\psi}_3^{0j'(4)}(\boldsymbol{k}^\star_\perp,x,\boldsymbol{k}'_\perp,x'). \tag{3.58}$$

Here $\boldsymbol{k}^{\star 2} = -x^2m^2-(1-x)\mu^2$. We have used the identity,

$$I_1^{(3)} = Z_\chi^{(3)} \equiv \lim_{\ell^2\to m^2}\left[1-\frac{\Sigma^{(3)}(\ell^2)-\Sigma^{(3)}(m^2)}{\ell^2-m^2}\right]^{-1}. \tag{3.59}$$

Equation (3.58) expresses $g_{\rm B4}$ in terms of the LFWF $\widetilde{\psi}_3^{0j'(4)}(\boldsymbol{k}^\star_\perp,x,\boldsymbol{k}'_\perp,x')$. However, the substitution $\boldsymbol{k}_\perp \to \boldsymbol{k}^\star_\perp$ is achieved through analytic continuation, and is unsuitable for numerical calculations. Instead, we treat $\widetilde{\psi}_3^{0j'(4)}(\boldsymbol{k}^\star_\perp,x,\boldsymbol{k}'_\perp,x')$ (and $\widetilde{\Gamma}_3^{0j'(4)}(\boldsymbol{k}^\star_\perp,x,\boldsymbol{k}'_\perp,x')$) as an auxiliary function and derive the equation for it by taking $\boldsymbol{k}_{a\perp} \to \boldsymbol{k}^\star_{a\perp} \equiv -x_a^2m^2-(1-x_a)\mu^2$ in Eq. (3.57)

for the $j_a = 0$ component,

$$\left(1 - \frac{\Sigma^{(2)}(t^\star) - \Sigma^{(2)}(m^2)}{t^\star - m^2}\right)\widetilde{\Gamma}_3^{0j_b(4)}(\boldsymbol{k}^\star_{a\perp}, x_a, \boldsymbol{k}_{b\perp}, x_b) = \frac{g_{\mathrm{B}3}(\frac{x_a}{1-x_b})}{1-x_b}\psi_2^{j_b(4)}(\boldsymbol{k}_{b\perp}, x_b)$$
$$+ g_{\mathrm{B}2}^2 \sum_{j=0}^{1}(-1)^j \int_0^{1-x_a-x_b} \frac{\mathrm{d}x}{2x(1-x_a-x_b-x)(1-x_a-x)} \int \frac{\mathrm{d}^2k_\perp}{(2\pi)^3} \frac{1}{s_4^\star - m^2}$$
$$\times \left[\widetilde{\psi}_3^{0j(4)}(\boldsymbol{k}^\star_{a\perp}, x_a, \boldsymbol{k}_\perp, x) + \psi_3^{j_b j(4)}(\boldsymbol{k}_{b\perp}, x_b, \boldsymbol{k}_\perp, x)\right], \quad (3.60)$$

where $t^\star = m^2 - (1-x_a-x_b)\left(\frac{\boldsymbol{k}^{\star 2}_{a\perp}+\mu^2}{x_a} + \frac{\boldsymbol{k}^2_{b\perp}+\mu^2_{j_b}}{x_b} + \frac{(\boldsymbol{k}^\star_{a\perp}+\boldsymbol{k}_{b\perp})^2+m^2}{1-x_a-x_b} - m^2\right)$, $s_4 = \frac{\boldsymbol{k}^{\star 2}_{a\perp}+\mu^2}{x_a} + \frac{\boldsymbol{k}^2_{b\perp}+\mu^2_{j_b}}{x_b} + \frac{\boldsymbol{k}^2_\perp+\mu^2_j}{x} + \frac{(\boldsymbol{k}^\star_{a\perp}+\boldsymbol{k}_{b\perp}+\boldsymbol{k}_\perp)^2+m^2}{1-x_a-x_b-x}$ are the same quantities defined above, except $\boldsymbol{k}_{a\perp}$ replaced by $\boldsymbol{k}^\star_{a\perp}$. It is important to note that $t^\star \neq m^2$, $s_4^\star \neq m^2$, so that there is no mass pole within this equation, confirming our previous claim that all singular terms are absorbed into the first term of Eq. (3.55).

Now, Eq.'s (3.49, 3.52, 3.58, 3.60) form a set of closed inhomogeneous linear coupled integral equations for $\psi_2^{j(4)}(\boldsymbol{k}_\perp, x), \psi_3^{j_a j_b(4)}(\boldsymbol{k}_{a\perp}, x_a, \boldsymbol{k}_{b\perp}, x_b), \widetilde{\psi}_3^{0j_b(4)}(\boldsymbol{k}^\star_{a\perp}, x_a, \boldsymbol{k}_{b\perp}, x_b)$, and $g_{\mathrm{B}4}\psi_1^{(4)}$. We can solve these equations to obtain the solution for the four-body truncation $(\chi + 3\varphi)$. Then, $\psi_1^{(4)}$ can be obtained from the normalization condition Eq. (3.18). Let us collect the coupled integral equations:

$$\Gamma_2^{j(4)}(\boldsymbol{k}_\perp, x) = g/\sqrt{I_1^{(3)}} + \frac{\delta m_3^2}{1-x}\psi_2^{j(4)}(\boldsymbol{k}_\perp, x) + \sum_{j'=0}^{1}(-1)^{j'} \int_0^{1-x} \frac{\mathrm{d}x'}{2x'(1-x-x')} \int \frac{\mathrm{d}^2k'_\perp}{(2\pi)^3}$$
$$\times g_{\mathrm{B}3}(\tfrac{x'}{1-x})\left[\psi_3^{jj'(4)}(\boldsymbol{k}_\perp, x, \boldsymbol{k}'_\perp, x') - \widetilde{\psi}_3^{0j'(4)}(\boldsymbol{k}^\star_\perp, x, \boldsymbol{k}'_\perp, x')\right], \quad (3.61)$$

$$\left(1 - \frac{\Sigma^{(2)}(t) - \Sigma^{(2)}(m^2)}{t - m^2}\right)\Gamma_3^{j_a j_b(4)}(\boldsymbol{k}_{a\perp}, x_a, \boldsymbol{k}_{b\perp}, x_b) = \left[\frac{g_{\mathrm{B}3}(\frac{x_b}{1-x_a})}{1-x_a}\psi_2^{j_a(4)}(\boldsymbol{k}_{a\perp}, x_a)\right.$$
$$\left. + g_{\mathrm{B}2}^2 \sum_{j=0}^{1}(-1)^j \int_0^{1-x_a-x_b} \frac{\mathrm{d}x}{2x(1-x_a-x)} \int \frac{\mathrm{d}^2k_\perp}{(2\pi)^3} \frac{\psi_3^{j_a j(4)}(\boldsymbol{k}_{a\perp}, x_a, \boldsymbol{k}_\perp, x)}{(1-x_a-x_b-x)(s_4 - m^2)}\right] + (a \leftrightarrow b), \quad (3.62)$$

$$\left(1 - \frac{\Sigma^{(2)}(t^\star) - \Sigma^{(2)}(m^2)}{t^\star - m^2}\right)\widetilde{\Gamma}_3^{0j_b(4)}(\boldsymbol{k}^\star_{a\perp}, x_a, \boldsymbol{k}_{b\perp}, x_b) = \frac{g_{\mathrm{B}3}(\frac{x_a}{1-x_b})}{1-x_b}\psi_2^{j_b(4)}(\boldsymbol{k}_{b\perp}, x_b)$$
$$+ g_{\mathrm{B}2}^2 \sum_{j=0}^{1}(-1)^j \int_0^{1-x_a-x_b} \frac{\mathrm{d}x}{2x(1-x_a-x)} \int \frac{\mathrm{d}^2k_\perp}{(2\pi)^3} \frac{1}{(1-x_a-x_b-x)(s_4^\star - m^2)}$$
$$\times \left[\widetilde{\psi}_3^{0j(4)}(\boldsymbol{k}^\star_{a\perp}, x_a, \boldsymbol{k}_\perp, x) + \psi_3^{j_b j(4)}(\boldsymbol{k}_{b\perp}, x_b, \boldsymbol{k}_\perp, x)\right], \quad (3.63)$$

where $t = m^2 - (1-x_a-x_b)\big(\frac{\boldsymbol{k}_{a\perp}^2+\mu_{ja}^2}{x_a} + \frac{\boldsymbol{k}_{b\perp}^2+\mu_{j_b}^2}{x_b} + \frac{(\boldsymbol{k}_{a\perp}+\boldsymbol{k}_{b\perp})^2+m^2}{1-x_a-x_b} - m^2\big)$, $s_4 = \frac{\boldsymbol{k}_{a\perp}^2+\mu_{ja}^2}{x_a} + \frac{\boldsymbol{k}_{b\perp}^2+\mu_{j_b}^2}{x_b} + \frac{\boldsymbol{k}_{\perp}^2+\mu_{j}^2}{x} + \frac{(\boldsymbol{k}_{a\perp}+\boldsymbol{k}_{b\perp}+\boldsymbol{k}_{\perp})^2+m^2}{1-x_a-x_b-x}$, $t^\star = m^2 - (1-x_a-x_b)\big(\frac{\boldsymbol{k}_{a\perp}^{\star 2}+\mu^2}{x_a} + \frac{\boldsymbol{k}_{b\perp}^2+\mu_{j_b}^2}{x_b} + \frac{(\boldsymbol{k}_{a\perp}^\star+\boldsymbol{k}_{b\perp})^2+m^2}{1-x_a-x_b} - m^2\big)$, $s_4 = \frac{\boldsymbol{k}_{a\perp}^{\star 2}+\mu^2}{x_a} + \frac{\boldsymbol{k}_{b\perp}^2+\mu_{j_b}^2}{x_b} + \frac{\boldsymbol{k}_{\perp}^2+\mu_{j}^2}{x} + \frac{(\boldsymbol{k}_{a\perp}^\star+\boldsymbol{k}_{b\perp}+\boldsymbol{k}_{\perp})^2+m^2}{1-x_a-x_b-x}$, are the same quantities introduced before. The relation between the vertex functions and the LFWFs is as usual.

Let us close this sub-section with two observations.

Our first observations is that Eq.'s (3.61–3.63) contain the bare mass $\delta m_3^2 = \Sigma^{(3)}(m^2)$ which diverges when taking the PV mass $\mu_{\rm PV} \to \infty$. But any physical observable should be independent of the UV regulator. We will solve the coupled integral equations with finite PV masses, and then study the UV-regulator sensitivity of the observables. It is possible to reformulate the integral equations in such a way that no bare mass appears explicitly in the integral equations. But we shall not pursue that route for the present.

The second observation is that Eq.'s (3.55–3.58, 3.60) also form a set of closed coupled integral equations. These equations do not depend explicitly on the bare mass[13], and the UV regulator can be removed (i.e. one can take $\mu_{\rm PV} \to \infty$). However, this formulation depends on the *off-shell* three-body truncated LFWF $\psi_2^{j_b(3)}(\boldsymbol{\kappa}_\perp, \xi; \ell^2)$ and the self-energy function $\Sigma^{(3)}(\ell)$. As we have warned in Sect. 3.4.3, these quantities may not exist for arbitrary ℓ^2. In contrast, our current formulation only depends on the *on-shell* three-body truncated LFWF and the self-energy function at the neighborhood of the mass shell $\ell^2 = m^2$. These quantities always exist up to $\alpha_{\rm L}$, as $I_1^{(3)}$ exists and it is related to the derivative $\partial/\partial p^2 \Sigma^{(3)}(p^2)_{p^2\to m^2}$. $= (1-\Sigma())^{-1}$.

3.5.2 Numerical results

To solve the coupled integral equations for the vertex functions, we first discretize them on a chosen 5-dimensional grid. The size of the grid is proportional to $N_{\rm lfx}^2 N_{\rm rad}^2 N_{\rm ang}$, where $N_{\rm rad}, N_{\rm ang}, N_{\rm lfx}$ are the number of grid points in the transverse radial, angular and the longitudinal directions, respectively. We approximate the integrals by the Gauss-Legendre quadrature method. For example,

$$\int \mathrm{d}x\, f(x) \approx \sum_i w_i f(x_i), \tag{3.64}$$

[13] This is one of the several possible reformulations that eliminate the bare mass.

where the quadrature abscissas x_i and weights w_i can be generated in advance (see Appendix D for more details).

For the integrals in the transverse radial direction, we perform a change of variable

$$k_\perp = a\frac{e^{bz}-1}{e-e^z}, \quad (z \in (0,1))$$

first for each transverse momentum $k_\perp$ before applying the quadrature method. Parameters a, b are adjusted[14] to achieve optimal convergence. For sufficiently fine grid, results should be independent of the choice of a and b. Integrals in the longitudinal direction often come with varying limits. For example,

$$\int_0^{1-x} \mathrm{d}x'\, f(x') = (1-x)\int_0^1 \mathrm{d}\xi\, f(\xi(1-x)) \approx (1-x)\sum_i w_i\, f(\xi_i(1-x)).$$

As is shown in the above example, we first scale the integration variable to a fixed interval, interpolating on the external grid points as necessary. The extracted factors like $(1-x)$ are often useful to cancel the same factors from the denominators such that no end-point singularity occurs within the longitudinal integrations. We make use of the properties of the trigonometric functions and reduce the angular integration from $(0, 2\pi)$ to $(0, \pi)$. In practice, we find that, in general, the integrations in the longitudinal direction require more grid points to obtain accuracy comparable to those in the transverse direction.

We employ an iterative method to solve the system of equations Eq.'s (3.61–3.63). We start with an educated initial guess[15] of the vertex functions and update them iteratively, until reaching a point-wise absolute tolerance,

$$\max\Big\{\big|\Gamma(\text{after update}) - \Gamma(\text{before update})\big|\Big\} < 10^{-4}. \tag{3.65}$$

Typically, we need $(50 \sim 100)$ iterations to reach numerical convergence (see Fig. 3.20). The iterative procedure diverges near the critical coupling $\alpha_{\mathrm{F}} \approx 2.19$. The coupled integral equations in the 3-body truncation are solved using the same method, though we also use the direct methods, e.g. LU factorization, to crosscheck the results there. Comparing the rate of convergence for the three- and four-body truncations, the former is much faster and there appears no divergence at or beyond the Fredholm critical coupling α_{F}.

[14] It is a common practice to tie a, b to the UV regulator(s). We choose not to do so in this calculation.

[15] For example, the solution of the three-body truncation at the same coupling. We also use the priorly obtained solutions at a slightly different coupling.

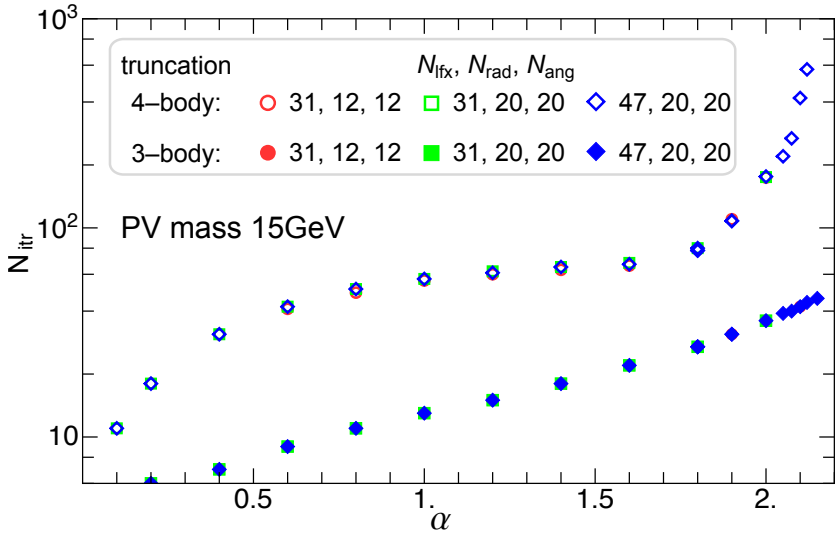

Figure 3.20: The number of iterations needed to achieve absolute convergence 10^{-4} (10^{-8}) for solving the coupled integral equations within the four-body (three-body) truncation. For the four-body truncation, the iterative procedure divergences at and beyond $\alpha_{\rm F} \approx 2.2$.

We solved the coupled integral equations at $m = 0.94\,\text{GeV}, \mu = 0.14\,\text{GeV}$. We developed a parallel code in Fortran with hybrid MPI/OpenMP for the numerical calculations. The numerical results are obtained using Cray XE6 Hopper at NERSC.

A representative LFWF and the vertex functions are shown in Fig. 3.21. With the obtained $\psi_2^{j(4)}$ and $\psi_3^{j_a j_b (4)}$, the normalization of the wavefunctions reads (Fig. 3.22),

$$
\begin{aligned}
1 = I_1 + I_2 + I_3 + I_4 \equiv \left|\psi_1^{(4)}\right|^2 &+ \sum_{j=0}^{1}(-1)^j \int_0^1 \frac{\mathrm{d}x}{2x(1-x)} \int \frac{\mathrm{d}^2 k_\perp}{(2\pi)^3} \left|\psi_2^{j(4)}(\boldsymbol{k}_\perp, x)\right|^2 \\
&+ \frac{1}{2!}\sum_{j_a,j_b=0}^{1}(-1)^{j_a+j_b} \int_0^1 \frac{\mathrm{d}x_a}{2x_a} \int \frac{\mathrm{d}^2 k_{a\perp}}{(2\pi)^3} \int_0^{1-x_a} \frac{\mathrm{d}x_b}{2x_b(1-x_a-x_b)} \int \frac{\mathrm{d}^2 k_{b\perp}}{(2\pi)^3} \left|\psi_3^{j_a j_b (4)}(\boldsymbol{k}_{a\perp}, x_a, \boldsymbol{k}_{b\perp}, x_b)\right|^2 \\
&+ \frac{1}{3!}\sum_{j_a,j_b,j_c=0}^{1}(-1)^{j_a+j_b+j_c} \int_0^1 \frac{\mathrm{d}x_a}{2x_a} \frac{\mathrm{d}^2 k_{a\perp}}{(2\pi)^3} \int_0^{1-x_a} \frac{\mathrm{d}x_b}{2x_b} \int \frac{\mathrm{d}^2 k_{b\perp}}{(2\pi)^3} \int_0^{1-x_a-x_b} \frac{\mathrm{d}x_c}{2x_c(1-x_a-x_b-x_c)} \int \frac{\mathrm{d}^2 k_{c\perp}}{(2\pi)^3} \\
&\times \left|\psi_4^{j_a j_b j_c (4)}(\boldsymbol{k}_{a\perp}, x_a, \boldsymbol{k}_{b\perp}, x_b, \boldsymbol{k}_{c\perp}, x_c)\right|^2. \quad (3.66)
\end{aligned}
$$

Figure 3.23 plots the Fock sector norms $I_{1\text{–}4}$ as a function of the UV regulator, the PV mass $\mu_{\rm PV}$, for two representative coupling constants. It shows that for sufficiently large grids, $I_{1\text{–}4}$ converge as $\mu_{\rm PV}$ increases. As our grid is independent of $\mu_{\rm PV}$, this is a good sign that our calculation is convergent with respect to the UV regulator. In practice, we work with a grid

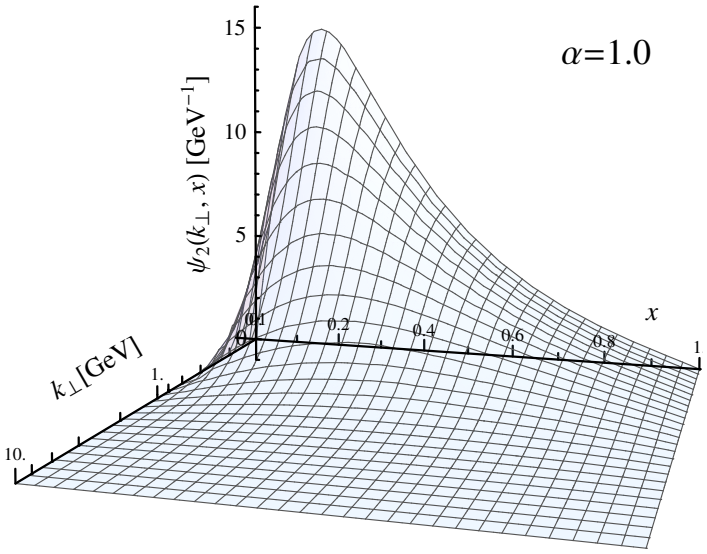

(a) A representative LFWF $\psi_2^{0(4)}(k_\perp, x)$ from the four-body truncation.

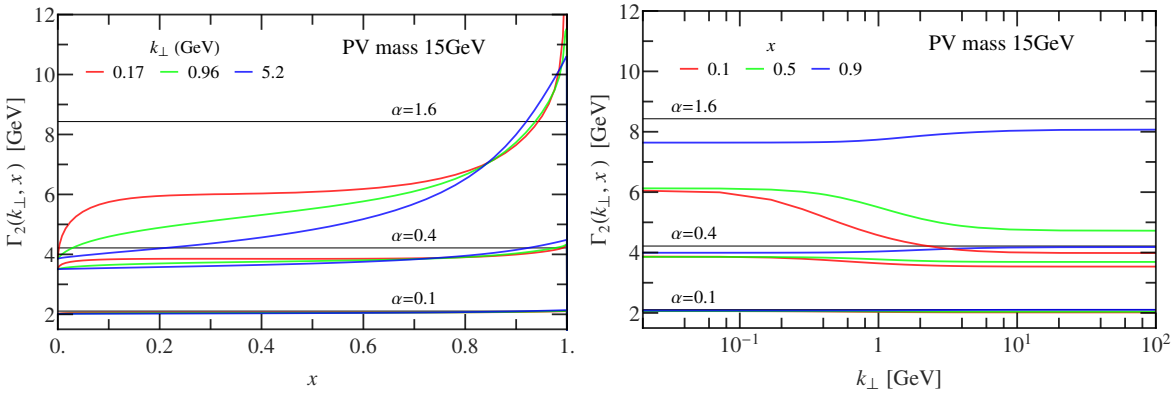

(b) A representative vertex function $\Gamma_2^{0(4)}(k_\perp, x)$ from the four-body truncation at three values of x (0.1, 0.5, 0.9) and three values of the coupling (0.1, 0.4, 1.6). At low x and low $k_\perp$, the lower the curve of a given color, the lower the value of the coupling. The horizontal lines represent the same vertex functions from the two-body truncation.

Figure 3.21: The two-body LFWF and the vertex function for selected couplings α.

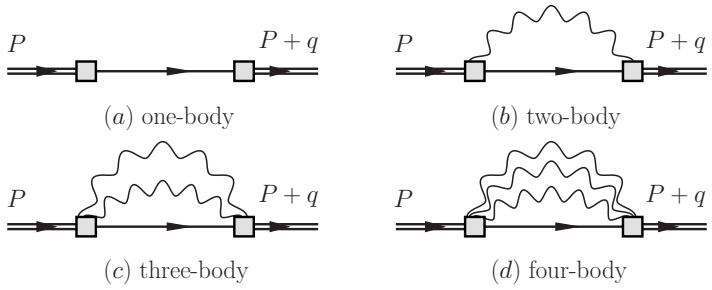

Figure 3.22: The diagrammatic representation of the normalization of the physical state in the four-body truncation.

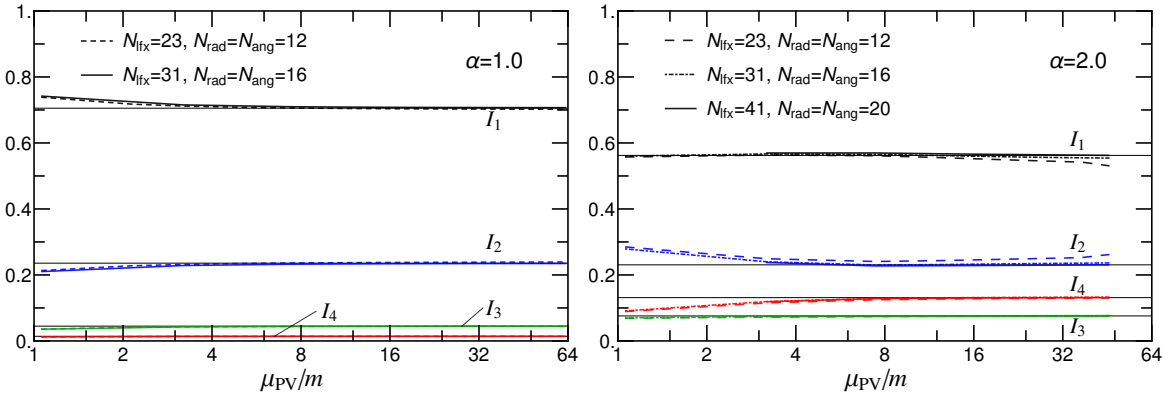

Figure 3.23: The normalization integrals as a function of the UV regulator $\mu_{\rm PV}/m$. The horizontal lines are the values from the finest grids with the largest PV mass.

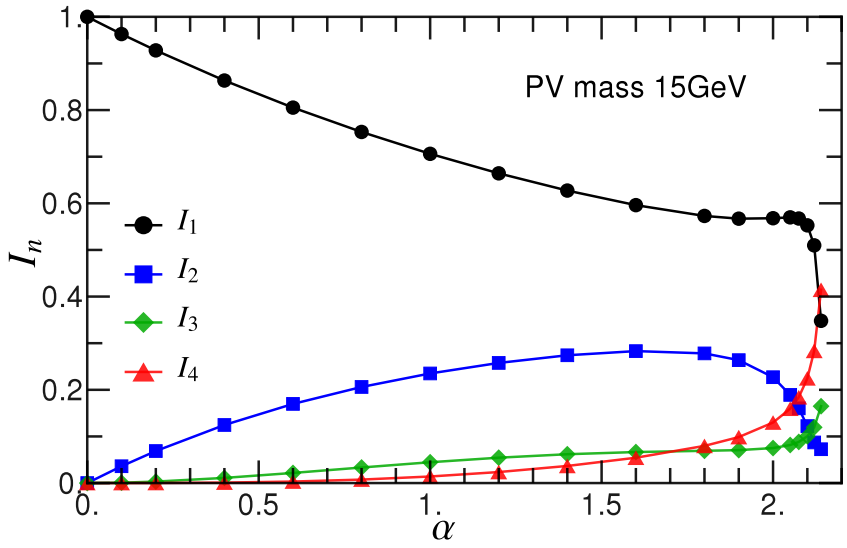

Figure 3.24: The Fock sector norms as a function of the coupling constant α.

$N_{\rm lfx} = 41\,(47)$, $N_{\rm rad} = N_{\rm ang} = 20$, and put $\mu_{\rm PV} = 15\,{\rm GeV} \gg m = 0.94\,{\rm GeV}$. The results are well converged for these parameters[16].

Figure 3.24 plots the Fock sector norms as a function of the coupling up to $\alpha = 2.12$. A natural Fock sector hierarchy $I_1 > I_2 > I_3 > I_4$ can be seen, up to $\alpha \approx 1.7$. Beyond that, the many-body sector I_3 and I_4 start increasing rapidly, overtaking I_2 at $\alpha \gtrsim 2.1$. The Fock sector norms in light-front dynamics admit a probabilistic interpretation. Therefore, the large contribution from the four-body sector beyond $\alpha \gtrsim 2.1$ representing the breakdown of the

[16]We do not attempt to extrapolate $\mu_{\rm PV} \to \infty$ on *fixed-size grids*, as larger $\mu_{\rm PV}$ requires more UV coverage to prevent introducing uncontrollable numerical errors.

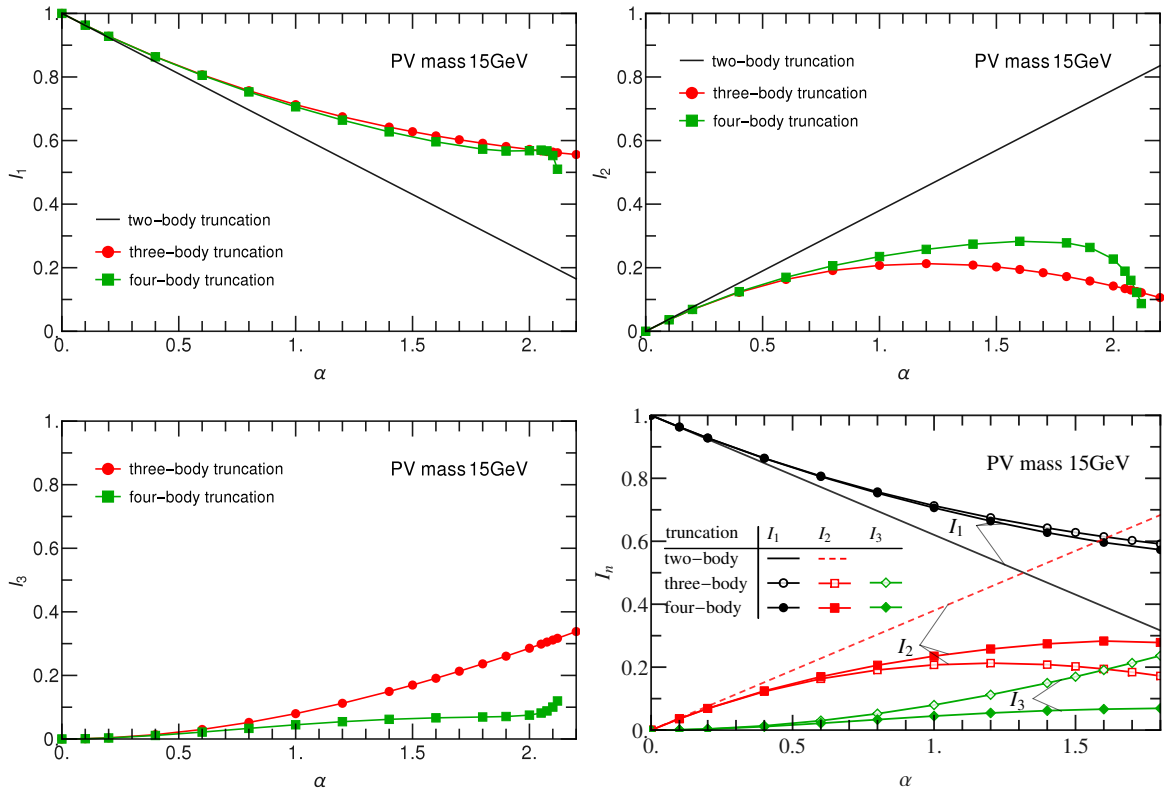

Figure 3.25: Comparison of Fock sector norms within the two-, three- and four-body truncations at different couplings.

Fock sector expansion as a valid approximation to the full problem, and higher Fock sector contributions are needed. Nevertheless, the lowest sectors, $|\chi\rangle + |\chi\varphi\rangle$, constitute more than 80% of the full norm up to $\alpha \approx 2.0$, validating the Fock sector expansion (aka. the Light-Front Tamm-Dancoff method) within the range of coupling accessible.

Figure 3.25 shows the Fock sector norms from the two-, three- and four-body truncations. The one- and two-body norms show a good trend of saturation as the Fock sector truncation is gradually lifted. In particular, I_1 changes little even in the large coupling regime. Another benchmark is the invalidation coupling α_{inv} of the Fock sector truncation, defined as the coupling at which the contribution of the highest Fock sector overtakes that of the next to highest sector. For the two-body truncation, $\alpha_{\text{inv}} \sim 1.3$; for the three-body truncation, $\alpha_{\text{inv}} \sim 1.6$, and for the four-body truncation, $\alpha_{\text{inv}} \sim 1.7$. The increasing α_{inv} suggests that the non-perturbative results can be systematically improved by including more Fock sectors.

3.6 Form Factor

The obtained LFWFs allow us to access a broad range of physical observables in the non-perturbative regime as shown in Chapter 2. In this section, we evaluate the elastic electromagnetic form factor by coupling the charged constituents (i.e., the chions) to an external electromagnetic field. As we mentioned in Sect. 2.4.3, form factors are defined in terms of the matrix element of the current operator. For the scalar particle $\mathcal{X}$ — the physical chion, the form factor $F(-q^2)$ is defined simply via the matrix element,

$$\langle P+q|J^{\mu}_{\rm em}(0)|P\rangle \equiv (P+P')^{\mu}F(-q^2), \tag{3.67}$$

where $|P\rangle$ is the state vector of the physical particle $\mathcal{X}$ carrying a 4-momentum P, and $P' = P+q$. The electromagnetic current is,

$$eJ^{\mu}_{\rm em} = i(D^{\mu}\chi)^{\dagger}\chi - i\chi^{\dagger}D^{\mu}\chi = e\Big[i\partial_{\mu}\chi^{\dagger}\chi - i\chi^{\dagger}\partial_{\mu}\chi - 2ieA^{\mu}\chi^{\dagger}\chi\Big], \tag{3.68}$$

where e is the charge of $\mathcal{X}$.

Within light-front dynamics, the form factor can be evaluated using the "+" component of the current operator within the Drell-Yan frame ($q^+ = 0$). The diagrammatic representation of the current matrix elements is shown in Fig. 3.26. The Fock sector contributions are obtained from the Drell-Yan-West formula [132],

$$F_l(Q^2) = \int D_l\, \psi_l(\boldsymbol{k}_{1\perp} - x_1\boldsymbol{q}_{\perp}, x_1, \boldsymbol{k}_{2\perp} - x_2\boldsymbol{q}_{\perp}, x_2, \cdots, \boldsymbol{k}_{(l-1)\perp} - x_{l-1}\boldsymbol{q}_{\perp}, x_{l-1}) \times \psi_l(\boldsymbol{k}_{1\perp}, x_1, \boldsymbol{k}_{2\perp}, x_2, \cdots, \boldsymbol{k}_{(l-1)\perp}, x_{l-1}), \tag{3.69}$$

where $Q^2 \equiv -q^2 = \boldsymbol{q}_{\perp}^2 > 0$,

$$\int D_l = \frac{1}{l!}\int \frac{{\rm d}x_1}{2x_1}\int \frac{{\rm d}^2k_{1\perp}}{(2\pi)^3}\cdots\int \frac{{\rm d}x_{l-1}}{2x_{l-1}}\int \frac{{\rm d}^2k_{(l-1)\perp}}{(2\pi)^3}, \tag{3.70}$$

is the Fock space volume element. Note that we have suppressed the relative momentum of the constituent chion in the expression. The form factor is the sum of the contributions from all sectors,

$$F(Q^2) = F_1(Q^2) + F_2(Q^2) + \cdots F_n(Q^2), \tag{3.71}$$

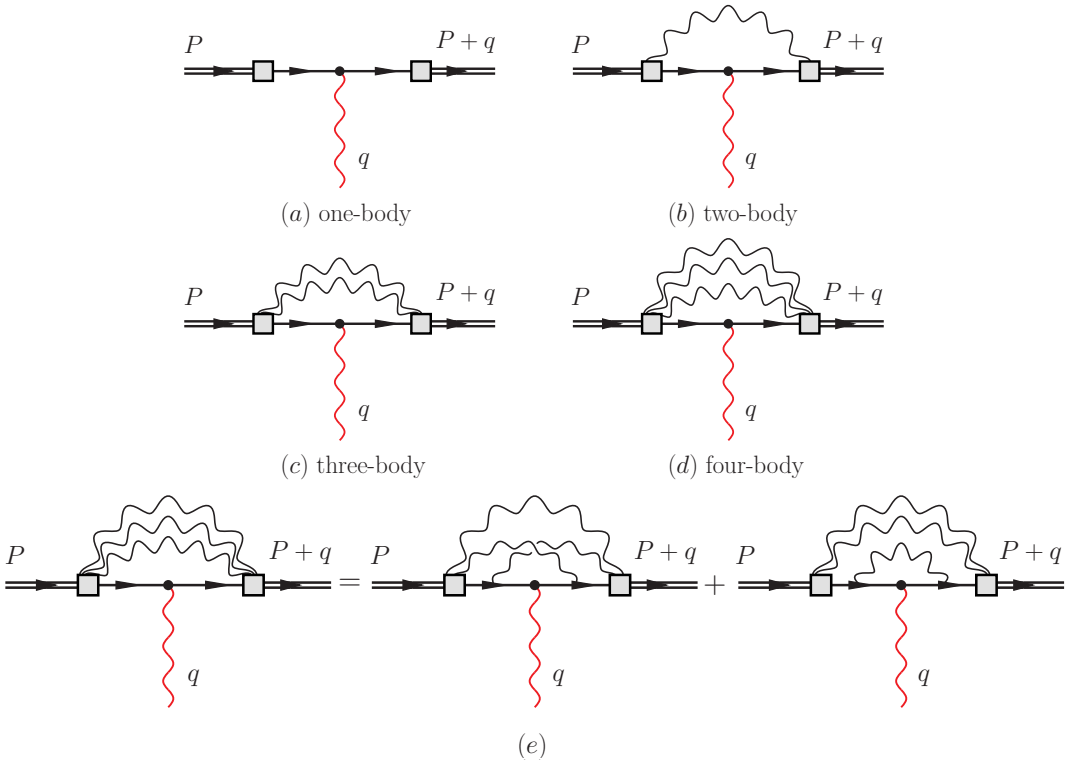

Figure 3.26: The diagrammatic representation of the form factor in the four-body truncation. (a–d): The one-, two-, three- and four-body Fock sector contributions to the form factor. The external photons are dyed red. (e): The four-body contribution is expressed in terms of the three-body contribution as a direct consequence of the four-body Fock sector truncation.

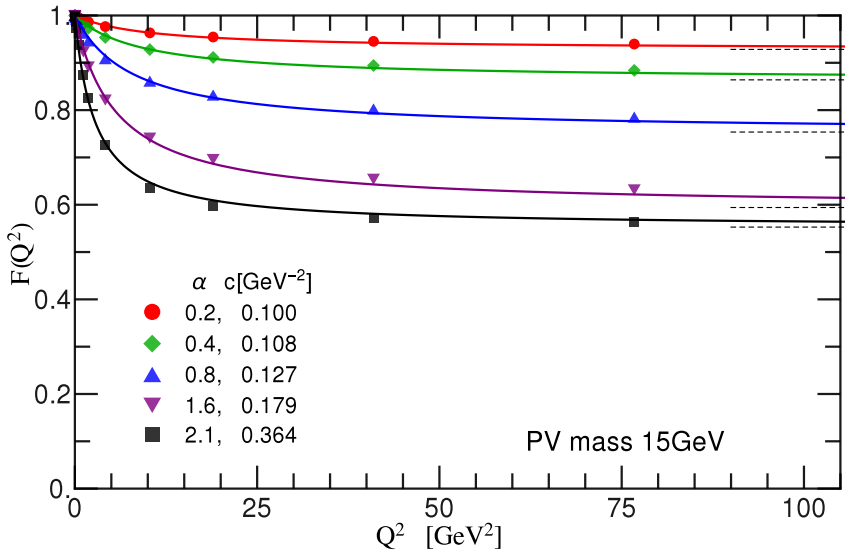

Figure 3.27: The elastic electromagnetic form factor $F(Q^2)$ in the four-body truncation for $\alpha = 0.2, 0.4, 0.8, 1.6$, and 2.1. The numerical results (symbols) are fitted by Eq. (3.74) (solid lines). The dashed lines indicate $I_1 = F(\infty)$ for each α.

for the n-body truncation $(\chi + (n-1)\varphi)$.

Comparing with the normalization of the physical state Eq. (3.66), at zero momentum transfer,

$$F_n(0) = I_n \quad \Longrightarrow \quad F(0) = 1, \tag{3.72}$$

consistent with the charge conservation. On the other hand, at large momentum transfer,

$$F_{n>1}(\infty) \to 0 \quad \Longrightarrow \quad F(\infty) \to I_1, \tag{3.73}$$

representing a point-like charge.

We evaluate Eq. (3.69) using the quadrature method in the same way as we solve the coupled integral equation, with extensive interpolations. The form factor within the four-body truncation at several selected couplings α are shown in Fig. 3.27. The form factors can be approximated by[17],

$$F(Q^2) \approx I_1 + \frac{1 - I_1}{1 + c\, Q^2}. \tag{3.74}$$

It is useful to study the dependence of the form factor on the Fock sector truncation. In particular, the comparison allows us to assess the convergence of the Fock sector expansion on an observable. Fig. 3.28 shows the form factors from different Fock sector truncations at two selected coupling constants. As is evident, the form factors from the three- and four-body truncation are quite close to each other, and the form factor saturates as we raise the Fock sector truncation even at non-perturbative couplings. The comparison of form factors suggests a reasonable convergence of the results with respect to the Fock sector expansion.

[17] Another useful fitting function is $F(Q^2) \approx I_1 + \frac{1-I_1}{(1+c_1\, Q^2)(1+c_2\, Q^2)}$ with $c_1 \geq c_2 > 0$.

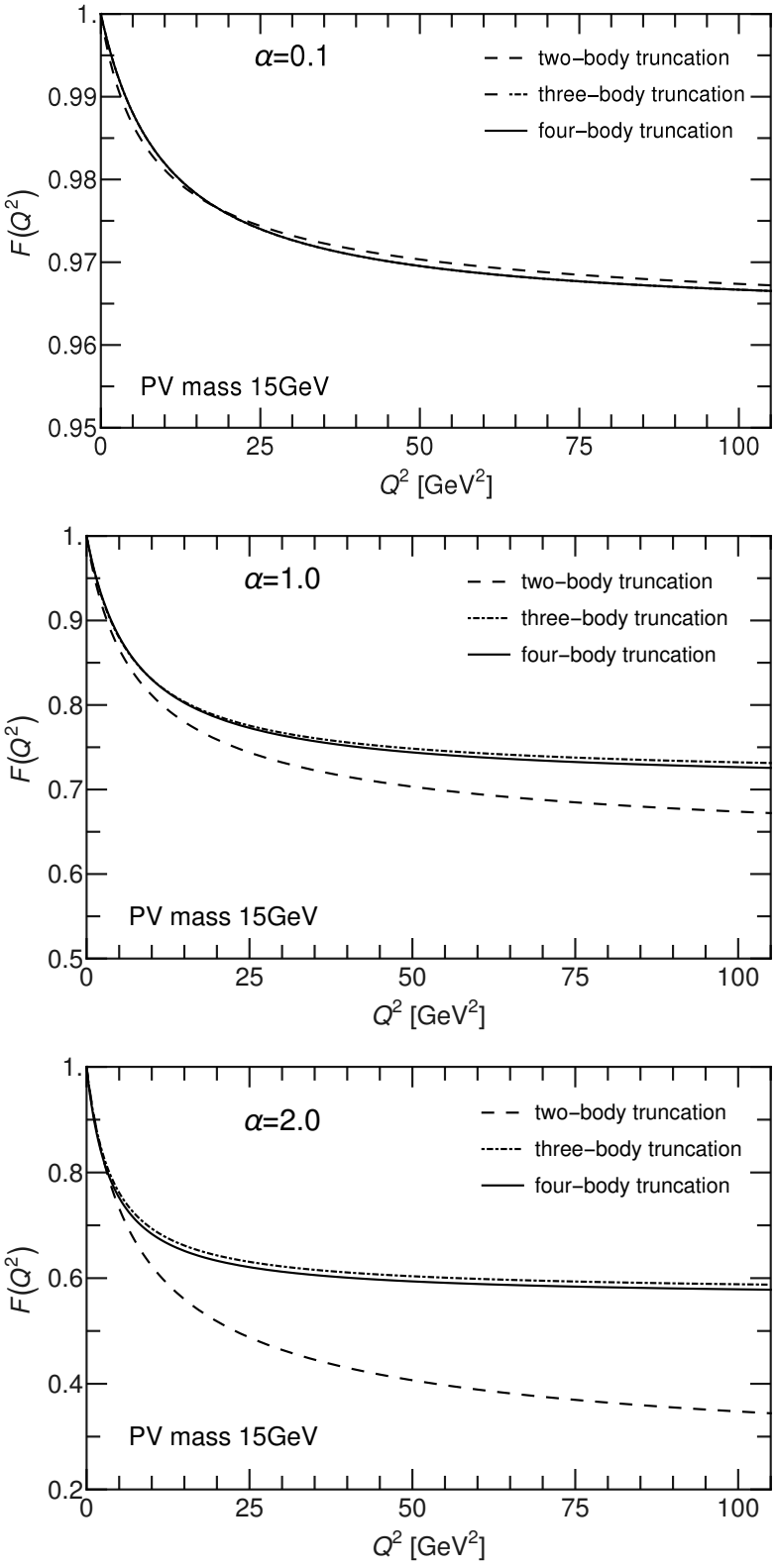

Figure 3.28: Comparison of the form factors calculated within the two-, three- and four-body truncations at $\alpha = 0.1$ (top), $\alpha = 1.0$ (middle) and $\alpha = 2.0$ (bottom). The three- and four-body form factors are fitted by Eq. (3.74) and the smooth curves represent the fitted results.

CHAPTER 4. CONCLUSIONS AND OUTLOOK

In this thesis, we developed and applied new techniques for solving non-perturbative light-front quantum field theory. As one feature, we adopted the Basis Light-Front Quantization approach and applied it to heavy quarkonium — QCD bound states. We also adopted a confining interaction from Light-Front Holographic QCD. We then extended Light-Front Holography by incorporating the quark mass and a novel longitudinal confinement. We also implemented an effective one-gluon exchange interaction in light-front dynamics. We diagonalized the Hamiltonian to obtain the mass spectrum and light-front wavefunctions. The resulting mass spectra for charmonium and bottomonium are close to experimental measurements. We also computed the decay constants and the elastic form factors. Our results are in good agreement with the available experimental data as well as with other established methods (e.g., Lattice QCD and Dyson-Schwinger Equation). This work improved the Light-Front Holography from its status as a first approximation to QCD. This work is also the first step towards a systematic *ab initio* computational framework to solve the QCD bound-state problems in the Basis Light-Front Quantization approach.

The current work can be extended to heavy-light, light-light and baryon systems. It can be extended to higher Fock sectors to incorporate sea-quark and gluon degrees of freedom. The treatment of the many-body dynamics is essential for obtaining realistic predictions for states above the thresholds or with exotic quantum numbers. The phenomenological confinement can be improved by a better understanding of the string/gauge duality [165] as well as a more complete derivation of the inter-quark potentials from various first-principle approaches to QCD [166]. Ultimately, the phenomenological confining interaction will be replaced by the QCD Hamiltonian, and the non-perturbative physics of the strong interaction should be directly generated from the many-body dynamics. These investigations must be accompanied

by innovations in both the theoretical and the computational fronts. For example, the treatment of the multi-gluon degrees of freedom is likely to require the study of symmetry breaking in light-front dynamics [167, 168], and the coherent basis is a natural choice [169].

In the meantime, the obtained light-front wavefunctions can be used to access additional hadronic observables, e.g., transition form factors [170], generalized parton distributions (GPDs) [126, 127, 129] and the transverse momentum distributions (TMDs) [171], which would provide crucial information for the ongoing and forthcoming experiments at experimental facilities such as the Thomas Jefferson Laboratory and the Large Hadron Collider (LHC).

Another topic we addressed in the thesis is the non-perturbative renormalization in light-front Hamiltonian quantum field theory, which represents one of the major theoretical challenges in this field. We focused on the Fock Sector Dependent Renormalization, and applied it to the scalar Yukawa model up to four-body (one complex scalar χ coupled to up to three real scalars φ) Fock sector truncation. The theory is properly renormalized and the coupled integral equations are derived. We then solved these equations in a parallel numerical procedure. We calculated the elastic electromagnetic form factor for the physical state. By comparing results from successive sector truncations (two-, three- and four-body), we showed that Fock sector convergence is achieved for the scalar Yukawa model. Therefore, we conclude that the Fock Sector Dependent Renormalization plus systematic Fock sector truncations constitutes an *ab initio* approach to quantum field theories on the light front.

The Fock Sector Dependent Renormalization scheme can be applied the bound-state problem in the scalar Yukawa model. Within the FSDR approach, all parameters of the bound-state system have been fixed and properly renormalized from the the single-particle (charge-one) sector. By solving the eigenvalue equation in the two-particle (charge-zero) sector, we will naturally take into account all contributions allowed by the Fock sector truncation, including, but not limited to, self energy [172], ladder [173], cross ladder [174], stretched box [175] etc. By comparing successive truncations, we can assess the convergence of the Fock sector expansion for the bound-state problem [176].

In parallel to the investigation of the scalar Yukawa model, we can also apply FSDR to the Yukawa model [150] and QED [35, 54, 119, 177]. Studying these applications will provide

valuable insights to the strongly interacting relativistic bound states. These explorations will also lay a solid foundation for solving QCD. The current approach can also be used to solve effective field theories non-perturbatively retaining full relativity.

The two distinct investigations in this thesis are unified under one theme: the *ab initio* approach to light-front quantum field theories. In particular, we have capitalized the computational physics implementation of this approach throughout the thesis. It is, therefore, essential to combine the strengths of the Basis Light-Front Quantization and the Fock Sector Dependent Renormalization in the future. The ever increasing computational capacity represent a growing opportunity for understanding non-perturbative quantum field theories on the light-front within the *ab initio* approach.

APPENDIX A. CONVENTIONS

Throughout the thesis, we use natural units, $\hbar = c = 1$. Let $x = (x^0, x^1, x^2, x^3) = (t, \boldsymbol{x})$ be the standard space-time coordinates. The signature of *Minkowski* space metric tensor is $g_{\mu\nu} = \mathrm{diag}\{+1, -1, -1, -1\}$.

Light-Front Coordinates

The light-front coordinates are defined as (x^+, x^-, x^1, x^2), where $x^+ = x^0 + x^3$ is the light-front time, $x^- = x^0 - x^3$ is the longitudinal coordinate, $\boldsymbol{x}^\perp = (x^1, x^2)$ are the transverse coordinates. The corresponding metric tensor and its inverse is,

$$\left[g_{\mu\nu}\right] = \begin{pmatrix} g_{++} & g_{+-} & g_{+1} & g_{+2} \\ g_{-+} & g_{--} & g_{-1} & g_{-2} \\ g_{1+} & g_{1-} & g_{11} & g_{12} \\ g_{2+} & g_{2-} & g_{21} & g_{22} \end{pmatrix} = \begin{pmatrix} 0 & \frac{1}{2} & 0 & 0 \\ \frac{1}{2} & 0 & 0 & 0 \\ 0 & 0 & -1 & 0 \\ 0 & 0 & 0 & -1 \end{pmatrix}, \tag{A.1}$$

$$\left[g^{\mu\nu}\right] = \begin{pmatrix} g^{++} & g^{+-} & g^{+1} & g^{+2} \\ g^{-+} & g^{--} & g^{-1} & g^{-2} \\ g^{1+} & g^{1-} & g^{11} & g^{12} \\ g^{2+} & g^{2-} & g^{21} & g^{22} \end{pmatrix} = \begin{pmatrix} 0 & 2 & 0 & 0 \\ 2 & 0 & 0 & 0 \\ 0 & 0 & -1 & 0 \\ 0 & 0 & 0 & -1 \end{pmatrix}. \tag{A.2}$$

Note that $\sqrt{-\det g} = \frac{1}{2}$. The Levi-Civita *tensor* is defined as [11],

$$\varepsilon^{\mu\nu\rho\sigma} = \frac{1}{\sqrt{-\det g}} \begin{pmatrix} \mu & \nu & \rho & \sigma \\ - & + & 1 & 2 \end{pmatrix} = \begin{cases} +2 & \text{if } \mu, \nu, \rho, \sigma \text{ is an even permutation of } -, +, 1, 2 \\ -2 & \text{if } \mu, \nu, \rho, \sigma \text{ is an odd permutation of } -, +, 1, 2 \\ 0 & \text{other cases.} \end{cases} \tag{A.3}$$

Similarly, the light-front components of a 4-vector $v = (v^0, \boldsymbol{v})$ is $(v^+, v^-, \boldsymbol{v}^\perp)$, where $v^\pm = v^0 \pm v^3$ and $\boldsymbol{v}^\perp = (v^1, v^2)$. Sometimes it is also useful to introduce the complex representation for the transverse vector $\boldsymbol{v}^\perp$: $v^L = v^1 - \mathrm{i}v^2$, and $v^R = v^1 + \mathrm{i}v^2 = (v^L)^*$. The components of the countervariant 4-vector $v_\mu = g_{\mu\nu}v^\mu$ are: $(v_-, v_+, \boldsymbol{v}_\perp)$, where $v_\pm = \frac{1}{2}(v_0 \pm v_3) = \frac{1}{2}v^\mp$, $\boldsymbol{v}_\perp = -\boldsymbol{v}^\perp$.

It is useful to introduce two vectors to symbolically restore the covariance: $\omega = (1, 0, 0, -1) = (1, \boldsymbol{\omega})$, and $\eta = (0, 1, 0, 0) = (0, \boldsymbol{\eta})$. They satisfy

$$\omega_\mu\omega^\mu = 0,\ \eta_\mu\eta^\mu = -1,\ \eta_\mu\omega^\mu = 0, \quad (\boldsymbol{\omega}^2 = \boldsymbol{\eta}^2 = 1). \tag{A.4}$$

Then, the longitudinal coordinate of a vector a can be written as $a^+ = \omega \cdot a$. Similarly, the transverse component of it becomes $\boldsymbol{a}^\perp = \boldsymbol{a} - \boldsymbol{\omega}(\boldsymbol{\omega} \cdot \boldsymbol{a})$.

The inverse derivatives $1/\partial^+$ and $1/(\partial^+)^2$ are resulted from solving constraint equations. They satisfy,

$$\partial^+\left(\frac{1}{\partial^+}f(x^-)\right) = f(x^-), \quad (\partial^+)^2\left(\frac{1}{(\partial^+)^2}f(x^-)\right) = f(x^-). \tag{A.5}$$

They can be formally written as,

$$\begin{aligned}\frac{1}{\partial^+}f(x^-) =& \frac{1}{4}\int_{-\infty}^{+\infty}\mathrm{d}y^-\mathrm{sign}(x^- - y^-)f(y^-),\\ \frac{1}{(\partial^+)^2}f(x^-) =& \frac{1}{8}\int_{-\infty}^{+\infty}\mathrm{d}y^-|x^- - y^-|f(y^-).\end{aligned} \tag{A.6}$$

by choosing the antisymmetric boundary conditions in x^-:

$$\begin{aligned}&\lim_{L\to\infty}\frac{1}{\partial^+}f(x^- = -L) + \big(\frac{1}{\partial^+}f\big)(x^- = +L) = 0\\ &\lim_{L\to\infty}\frac{1}{(\partial^+)^2}f(x^- = -L) + \big(\frac{1}{(\partial^+)^2}f\big)(x^- = +L) = 0.\end{aligned} \tag{A.7}$$

The coordinate space integration measure is defined as

$$\int \mathrm{d}^3x \equiv \int \mathrm{d}x_+\mathrm{d}^2x^\perp = \tfrac{1}{2}\int \mathrm{d}x^-\mathrm{d}^2x^\perp. \tag{A.8}$$

The full four-dimensional integration measure is,

$$\int \mathrm{d}^4x = \int \mathrm{d}x^0\mathrm{d}^3x = \frac{1}{2}\int \mathrm{d}x^+\mathrm{d}x^-\mathrm{d}^2x^\perp = \int \mathrm{d}^3x\,\mathrm{d}x^+. \tag{A.9}$$

In the momentum space, we use the Lorentz invariant integration measure:

$$\int \frac{\mathrm{d}^4p}{(2\pi)^4}\theta(p^+)2\pi\delta(p^2 - m^2) = \int \frac{\mathrm{d}^3p}{(2\pi)^3 2p^0}\theta(p^0) = \int \frac{\mathrm{d}^2p_\perp\mathrm{d}p^+}{(2\pi)^3 2p^+}\theta(p^+) = \int \frac{\mathrm{d}^2p_\perp}{(2\pi)^3}\int_0^1 \frac{\mathrm{d}x}{2x} \tag{A.10}$$

where $p^0 = \sqrt{\boldsymbol{p}^2 + m^2}$ is the on-shell energy and $x = p^+/P^+$ is the longitudinal momentum fraction. The corresponding normalization of the single-particle state is

$$\begin{aligned}\langle p, \sigma | p', \sigma' \rangle = 2p^0\theta(p^0)(2\pi)^3\delta^3(p-p')\delta_{\sigma\sigma'} = 2p^+\theta(p^+)(2\pi)^3\delta^3(p-p')\delta_{\sigma\sigma'} \\ = 2x(2\pi)^3\delta(x-x')\delta^2(\boldsymbol{p}_\perp - \boldsymbol{p}'_\perp)\delta_{\sigma\sigma'}. \quad \text{(A.11)}\end{aligned}$$

Here the light-front delta function is defined as $\delta^3(p) = \delta^2(\boldsymbol{p}_\perp)\delta(p^+)$.

Few-Body Kinematics

Two-Body kinematics Let $\boldsymbol{P}_\perp = \boldsymbol{p}_{1\perp} + \boldsymbol{p}_{2\perp}$, $P^+ = p_1^+ + p_2^+$ be the center-of-mass (c.m.) momentum of two on-shell particles with 4-momentum p_1, p_2, respectively ($p_a^2 = m_a^2$). Define the longitudinal momentum fraction $x_a = p_a^+/P^+$, ($x_1 + x_2 = 1$), and relative transverse momentum $\boldsymbol{p}_\perp = \boldsymbol{p}_{1\perp} - x_1\boldsymbol{P}_\perp$ ($-\boldsymbol{p}_\perp = \boldsymbol{p}_{2\perp} - x_2\boldsymbol{P}_\perp$). Then, the momentum space integration measure admits a factorization:

$$\int \frac{\mathrm{d}^2p_1^\perp \mathrm{d}p_1^+}{(2\pi)^3 2p_1^+} \int \frac{\mathrm{d}^2p_2^\perp \mathrm{d}p_2^+}{(2\pi)^3 2p_2^+} = \int \frac{\mathrm{d}^2p_1^\perp \mathrm{d}x_1}{(2\pi)^3 2x_1} \int \frac{\mathrm{d}^2p_2^\perp \mathrm{d}x_2}{(2\pi)^3 2x_2} = \int \frac{\mathrm{d}^2P^\perp \mathrm{d}P^+}{(2\pi)^3 2P^+} \int \frac{\mathrm{d}^2p^\perp \mathrm{d}x}{(2\pi)^3 2x(1-x)}. \quad \text{(A.12)}$$

where $x = x_1$. Similarly, the two-body Fock state

$$\begin{aligned}\langle p_1', p_2' | p_1, p_2 \rangle =& 2x_2\theta(p_2^+)(2\pi)^3\delta^2(p_2^\perp - p_2'^\perp)\delta(x_2 - x_2') \\ =& 2P^+\theta(P^+)(2\pi)^3\delta^3(P-P')2x(1-x)(2\pi)^3\delta^2(p_\perp - p'_\perp)\delta(x-x') \quad \text{(A.13)} \\ \equiv& \langle P'; \boldsymbol{p}'^\perp, x' | P; \boldsymbol{p}^\perp, x \rangle.\end{aligned}$$

Furthermore, the two-body invariant mass squared is,

$$s_2 \equiv (p_1 + p_2)^2 = \frac{\boldsymbol{p}_{1\perp}^2 + m_1^2}{x_1} + \frac{\boldsymbol{p}_{2\perp}^2 + m_2^2}{x_2} - \boldsymbol{P}_\perp^2 = \frac{\boldsymbol{p}_\perp^2 + m_1^2}{x} + \frac{\boldsymbol{p}_\perp^2 + m_2^2}{1-x}. \quad \text{(A.14)}$$

Here m_a is the a-th particle's mass.

Few-Body kinematics Define the few-body c.m. momentum $\boldsymbol{P}_\perp = \sum_a \boldsymbol{p}_{a\perp}$, $P^+ = \sum_a p_a^+$. Introduce the momentum fraction and the relative transverse momentum:

$$x_a = p_a^+/P^+, \quad \boldsymbol{k}_{a\perp} = \boldsymbol{p}_{a\perp} - x_a\boldsymbol{P}_\perp \quad \text{(A.15)}$$

Then, it is clear that $\sum_a x_a = 1$, and $\sum_a \boldsymbol{k}_{a\perp} = 0$. The few-body momentum space integration measure admits a factorization of the c.m. momentum:

$$\prod_a \int \frac{\mathrm{d}^2 p_a^\perp \mathrm{d}p_a^+}{(2\pi)^3 2p_a^+}\theta(p_a^+) = \int \frac{\mathrm{d}^2 P^\perp \mathrm{d}P^+}{(2\pi)^3 2P^+}\theta(P^+)\prod_a \int \frac{\mathrm{d}^2 k_a^\perp \mathrm{d}x_a}{(2\pi)^3 2x_a} \times 2(2\pi)^3\delta^2\Big(\sum_a \boldsymbol{k}_{a\perp}\Big)\delta\Big(\sum_a x_a - 1\Big) \tag{A.16}$$

The few-body invariant mass squared is,

$$s_n \equiv \Big(\sum_a p_a\Big)^2 = \sum_a \frac{\boldsymbol{k}_{a\perp}^2 + m_a^2}{x_a} \tag{A.17}$$

Lemma *cluster decomposition of* s_n:

Let $(x_a, \boldsymbol{k}_{a\perp})$, $(a = 1, 2\cdots, n)$ be n relative momenta, i.e. $\sum_a x_a = 1$, $\sum_a \boldsymbol{k}_{a\perp} = 0$. Define new relative momenta with respect to the cluster without the n-th particle: $\zeta_a = x_a/(1-x_n)$, $\boldsymbol{\kappa}_{a\perp} = \boldsymbol{k}_{a\perp} + \zeta_a \boldsymbol{k}_{n\perp}$. Then, the n-body invariant mass squared can be written as,

$$\begin{aligned}(1-x_n)\Big(\sum_{a=1}^{n}\frac{\boldsymbol{k}_{a\perp}^2 + m_a^2}{x_a} - M^2\Big) = \sum_{a=1}^{n-1}\frac{\boldsymbol{\kappa}_{a\perp}^2 + m_a^2}{\zeta_a} - m^2 \\ + (1-x_n)\Big(\frac{\boldsymbol{k}_{n\perp}^2 + m_n^2}{x_n} + \frac{\boldsymbol{k}_{n\perp}^2 + m^2}{1-x_n} - M^2\Big),\end{aligned} \tag{A.18}$$

or in short form,

$$(1-x_n)(s_n - M^2) = s_{n-1}^{\mathrm{rel}} - \big(m^2 - (1-x_n)(s_2 - M^2)\big) \equiv s_{n-1}^{\mathrm{rel}} - M_{\mathrm{int}}^2. \tag{A.19}$$

Gamma Matrices

In this convention, the 4-by-4 gamma matrices are defined as (cf. Dirac and chiral representation):

$$\gamma^0 = \begin{pmatrix} 0 & -\mathrm{i} \\ \mathrm{i} & 0 \end{pmatrix} \quad \gamma^3 = \begin{pmatrix} 0 & \mathrm{i} \\ \mathrm{i} & 0 \end{pmatrix} \quad \gamma^1 = \begin{pmatrix} -\mathrm{i}\sigma^2 & 0 \\ 0 & \mathrm{i}\sigma^2 \end{pmatrix} \quad \gamma^2 = \begin{pmatrix} \mathrm{i}\sigma^1 & 0 \\ 0 & -\mathrm{i}\sigma^1 \end{pmatrix} \tag{A.20}$$

where $\sigma = (1, \boldsymbol{\sigma})$ are the standard Pauli matrices,

$$\sigma^0 = \begin{pmatrix} 1 & 0 \\ 0 & 1 \end{pmatrix}, \quad \sigma^1 = \begin{pmatrix} 0 & 1 \\ 1 & 0 \end{pmatrix}, \quad \sigma^2 = \begin{pmatrix} 0 & -\mathrm{i} \\ \mathrm{i} & 0 \end{pmatrix}, \quad \sigma^3 = \begin{pmatrix} 1 & 0 \\ 0 & -1 \end{pmatrix}. \tag{A.21}$$

The γ-matrices defined here furnish a representation of the Clifford algebra $\mathrm{C}\ell_{1,3}(\mathbb{R})$:

$$\gamma^\mu\gamma^\nu + \gamma^\nu\gamma^\mu = 2g^{\mu\nu}. \tag{A.22}$$

Then, $S^{\mu\nu} \equiv \frac{\mathrm{i}}{4}[\gamma^\mu, \gamma^\nu]$ furnishes a spinorial representation of the Lorentz group. It is convenient to introduce the following 4-by-4 matrices,

- front-form: $\gamma^\pm \equiv \gamma^0 \pm \gamma^3$, $\boldsymbol{\gamma}^\perp \equiv (\gamma^1, \gamma^2)$, $\gamma^L \equiv \gamma^1 - \mathrm{i}\gamma^2$, $\gamma^R \equiv \gamma^1 + \mathrm{i}\gamma^2$, $\not{p} = p_\mu\gamma^\mu = \frac{1}{2}p^+\gamma^- + \frac{1}{2}p^-\gamma^+ - \boldsymbol{p}_\perp \cdot \boldsymbol{\gamma}_\perp$

  corollaries: $\gamma^+\gamma^+ = 0; \gamma^-\gamma^- = 0; \gamma^+\gamma^-\gamma^+ = 4\gamma^+, \gamma^-\gamma^+\gamma^- = 4\gamma^-; \gamma^0\gamma^\pm = \gamma^\mp\gamma^0$. The matrix form are:

$$\gamma^+ = \begin{pmatrix} 0 & 0 \\ 2\mathrm{i} & 0 \end{pmatrix}, \quad \gamma^- = \begin{pmatrix} 0 & -2\mathrm{i} \\ 0 & 0 \end{pmatrix}, \quad \gamma^L = \begin{pmatrix} \sigma^L & 0 \\ 0 & -\sigma^L \end{pmatrix}, \quad \gamma^R = \begin{pmatrix} -\sigma^R & 0 \\ 0 & \sigma^R \end{pmatrix},$$

  where,

$$\sigma^L = \sigma^1 - \mathrm{i}\sigma^2 = \begin{pmatrix} 0 & 0 \\ 2 & 0 \end{pmatrix}, \quad \sigma^R = \sigma^1 + \mathrm{i}\sigma^2 = \begin{pmatrix} 0 & 2 \\ 0 & 0 \end{pmatrix}.$$

- projections: $\Lambda^\pm \equiv \Lambda_\pm \equiv \frac{1}{2}\gamma^0\gamma^\pm$;

  corollaries: $\Lambda_\pm^2 = \Lambda_\pm$, $\Lambda^+\Lambda^- = 0$, $\Lambda^-\Lambda^+ = 0$, $\Lambda^+ + \Lambda^- = 1$.

  $\Lambda_\pm^\dagger = \Lambda_\pm$, $\overline{\Lambda}_\pm = \Lambda_\mp$, $\frac{1}{4}\gamma^+\gamma^- = \Lambda^-$, $\frac{1}{4}\gamma^-\gamma^+ = \Lambda^+$.

  Under the convention we use, the projections are diagonal and simple:

$$\Lambda^+ = \begin{pmatrix} 1 & & \\ & & \\ & & 0 \end{pmatrix}, \quad \Lambda^- = \begin{pmatrix} 0 & & \\ & & \\ & & 1 \end{pmatrix}$$

- parity matrix: $\beta = \gamma^0$; charge conjugation matrix: $\mathcal{C} = -\mathrm{i}\gamma^2$; time reversal matrix: $T = \gamma^1\gamma^3 = \mathcal{C}\gamma_5$

- chiral matrix: $\gamma^5 = \gamma_5 \equiv \mathrm{i}\gamma^0\gamma^1\gamma^2\gamma^3 = -\frac{\mathrm{i}}{4!}\varepsilon^{\mu\nu\rho\sigma}\gamma_\mu\gamma_\nu\gamma_\rho\gamma_\sigma$ is diagonal:

$$\gamma^5 = \begin{pmatrix} \sigma^3 & & \\ & & \\ & & -\sigma^3 \end{pmatrix}, \quad P_L = \frac{1}{2}\begin{pmatrix} \sigma^- & & \\ & & \\ & & \sigma^+ \end{pmatrix} \quad P_R = \frac{1}{2}\begin{pmatrix} \sigma^+ & & \\ & & \\ & & \sigma^- \end{pmatrix},$$

where $P_L = \frac{1}{2}(1-\gamma_5) = \mathrm{diag}\{0,1,1,0\}$, $P_R = \frac{1}{2}(1+\gamma_5) = \mathrm{diag}\{1,0,0,1\}$ are the two chiral projections, also diagonal. It is easy to see $P_L^2 = P_L$, $P_R^2 = P_R$, $P_L P_R = P_R P_L = 0$, $P_L + P_R = 1$.

- $\bar{\psi} \equiv \psi^\dagger \beta$ (for spinorial vector) and $\bar{A} = \beta A^\dagger \beta$ (for spinorial matrix).

  corollary:

$$\overline{\gamma^\mu} = \gamma^\mu, \quad \overline{S^{\mu\nu}} = S^{\mu\nu}, \quad \overline{\mathrm{i}\gamma_5} = i\gamma_5, \quad \overline{\gamma^\mu\gamma_5} = \gamma^\mu\gamma_5, \quad \overline{\mathrm{i}\gamma_5 S^{\mu\nu}} = \mathrm{i}\gamma_5 S^{\mu\nu}$$

  In other words, the spinorial representation is real.

- spin projection matrix S_z:

$$S_z = S^{12} = \frac{\mathrm{i}}{2}\gamma^1\gamma^2 = \frac{1}{2}\begin{pmatrix}\sigma^3 & \\ & \sigma^3\end{pmatrix}, \quad S^i = \frac{1}{2}\epsilon^{ijk}S^{jk} = \frac{1}{2}\begin{pmatrix}0 & -\mathrm{i}\sigma^i \\ \mathrm{i}\sigma^i & \end{pmatrix}$$

The gamma matrix identities Because gamma matrices satisfy anti-commutation relations, the trace of a string of gamma matrices follows the *Wick theorem* [7]:

> The trace of the product of gamma matrices equals the sum of all possible contractions with the corresponding permutation signatures included.

A contraction of any two gamma matrices γ_μ, γ_ν gives a factor $4g_{\mu\nu}$. If the two contracted gamma matrices are not adjacent, there would be a sign $(-1)^n$, where n is the number of exchange operations needed to makes them adjacent (but keeping their relative order).

Frequently used identities in $D = 4$ dimensions:

- $\mathrm{tr}\{\text{product of odd number of } \gamma\text{'s}\} = \mathrm{tr}\{\gamma_5 \cdot \text{ product of odd number of } \gamma\text{'s}\} = 0$
- $\mathrm{tr}\, 1 = 4, \quad \mathrm{tr}\,\gamma_5 = 0$
- $\mathrm{tr}\{\not{a}\not{b}\} = 4(a\cdot b), \quad \mathrm{tr}\{\gamma_5\not{a}\not{b}\} = 0$
- $\mathrm{tr}\{\not{a}\not{b}\not{c}\not{d}\} = 4\left((a\cdot b)(c\cdot d) - (a\cdot c)(b\cdot d) + (a\cdot d)(b\cdot c)\right), \quad \mathrm{tr}\{\gamma_5\not{a}\not{b}\not{c}\not{d}\} = -4\mathrm{i}\varepsilon^{\mu\nu\rho\sigma}a_\mu b_\nu c_\rho d_\sigma$

  Note that, when $\mu,\nu,\rho,\sigma = +,-,1,2$, $\varepsilon^{\mu\nu\rho\sigma} = \epsilon(\mu,\nu,\rho,\sigma)/\sqrt{-\det g}$

- $\gamma_\mu\gamma^\mu = 4, \quad \gamma_\mu \not{a} \gamma^\mu = (2-D)\not{a}, \quad \gamma_\mu \not{a}\not{b}\gamma^\mu = 4(a\cdot b) - (4-D)\not{a}\not{b}, \quad \gamma_\mu \not{a}\not{b}\not{c}\gamma^\mu = -2\not{c}\not{b}\not{a} + (4-D)\not{a}\not{b}\not{c}, \quad \gamma_\mu \not{a}\not{b}\not{c}\not{d}\gamma^\mu = 2\big(\not{d}\not{a}\not{b}\not{c} + \not{c}\not{b}\not{a}\not{d}\big) - (4-D)\not{a}\not{b}\not{c}\not{d};$

- $\not{a}\not{a} = a^2, \quad \not{a}\not{b} = -\not{b}\not{a} + 2(a\cdot b)$

Spinor Technology

The u, v spinors (Dirac spinors) are defined as,

$$\begin{aligned} u_s(p) &= \frac{1}{2\sqrt{p^+}}(\not{p}+m)\gamma^+\chi_s = \frac{1}{\sqrt{p^+}}(\not{p}+m)\beta\chi_s = \frac{1}{\sqrt{p^+}}(p^+ + \boldsymbol{\alpha}^\perp\cdot\boldsymbol{p}^\perp + \beta m)\chi_s; \\ v_s(p) &= \frac{1}{2\sqrt{p^+}}(\not{p}-m)\gamma^+\chi_{-s} = \frac{1}{\sqrt{p^+}}(\not{p}-m)\beta\chi_{-s} = \frac{1}{\sqrt{p^+}}(p^+ + \boldsymbol{\alpha}^\perp\cdot\boldsymbol{p}^\perp - \beta m)\chi_{-s}; \end{aligned} \tag{A.23}$$

where $\chi_+ = (1,0,0,0)^\intercal, \chi_- = (0,1,0,0)^\intercal$ are the basis of the two-component spinors (the dynamical spinors on the light front) and satisfy:

$$\Lambda_+\chi_s = \chi_s, \quad \Lambda_-\chi_s = 0, \quad \chi_s^\dagger\chi_{s'} = \delta_{ss'}, \quad S_z\,\chi_\pm = \pm\frac{1}{2}\chi_\pm. \tag{A.24}$$

The u, v spinors are polarized in the longitudinal direction:

$$S_z u_\pm(p^+, \boldsymbol{p}_\perp = 0) = \pm\tfrac{1}{2}u_\pm(p^+, \boldsymbol{p}_\perp = 0), \quad S_z v_\pm(p^+, \boldsymbol{p}_\perp = 0) = \mp\tfrac{1}{2}v_\pm(p^+, \boldsymbol{p}_\perp = 0). \tag{A.25}$$

and following the standard normalization scheme:

$$\bar{u}_s(p)u_{s'}(p) = 2m\delta_{ss'}, \quad \bar{v}_s(p)v_{s'}(p) = -2m\delta_{ss'}, \quad \bar{u}_s(p)v_{s'}(p) = \bar{v}_s(p)u_{s'}(p) = 0. \tag{A.26}$$

The spinor identities:

- Dirac equation:

$$(\not{p}-m)u_\sigma(p) = 0, \quad (\not{p}+m)v_\sigma(p) = 0; \tag{A.27}$$

- normalization:

$$\bar{u}_s(p)u_{s'}(p) = 2m\delta_{ss'}, \quad \bar{v}_s(p)v_{s'}(p) = -2m\delta_{ss'}, \quad \bar{u}_s(p)v_{s'}(p) = 0; \tag{A.28}$$

- spin sum:

$$\sum_{s=\pm} u_s(p)\bar{u}_s(p) = \not{p}+m, \quad \sum_{s=\pm} v_s(p)\bar{v}_s(p) = \not{p}-m; \tag{A.29}$$

- crossing symmetry:

$$u_s(p) = \sqrt{-1}v_{-s}(-p),\ \bar{u}_s(p) = \sqrt{-1}\bar{v}_{-s}(-p),\ v_s(p) = \sqrt{-1}u_{-s}(-p),\ \bar{v}_s(p) = \sqrt{-1}\bar{u}_{-s}(-p); \tag{A.30}$$

  Note that $p \to -p$ flips the sign of all four components of the momentum, including the light-front energy and the longitudinal momentum.

  The crossing symmetry is clearer if we define $w_s(p) = \frac{1}{2p^+}(\not{p} + m)\gamma^+\chi_s = \frac{1}{\sqrt{p^+}}u_s(p)$, and $z_s(p) = \frac{1}{2p^+}(\not{p} - m)\gamma^+\chi_{-s} = \frac{1}{\sqrt{p^+}}v_s(p)$. Then the cross symmetry between w and z is $z_s(p) = w_{-s}(-p), \bar{z}_s(p) = \bar{w}_{-s}(-p)$.

- Gordon identities:

$$\begin{aligned}
&2m\bar{u}_{s'}(p')\gamma^\mu u_s(p) = \bar{u}_{s'}(p')\big[(p+p')^\mu + 2\mathrm{i}S^{\mu\nu}(p'-p)_\nu\big]u_s(p);\\
&2m\bar{v}_{s'}(p')\gamma^\mu v_s(p) = -\bar{v}_{s'}(p')\big[(p+p')^\mu + 2\mathrm{i}S^{\mu\nu}(p'-p)_\nu\big]v_s(p);\\
&2m\bar{u}_{s'}(p')\gamma^\mu v_s(p) = \bar{u}_{s'}(p')\big[(p'-p)^\mu + 2\mathrm{i}S^{\mu\nu}(p'+p)_\nu\big]v_s(p);\\
&2m\bar{u}_{s'}(p')\gamma^\mu\gamma_5 u_s(p) = \bar{u}_{s'}(p')\big[(p-p')^\mu\gamma_5 + 2\mathrm{i}S^{\mu\nu}(p'+p)_\nu\gamma_5\big]u_s(p);
\end{aligned} \tag{A.31}$$

- other useful identities:

$$\begin{aligned}
&\bar{u}_s(p)\gamma^\mu u_{s'}(p) = 2p^\mu\delta_{ss'}, \quad \bar{v}_s(p)\gamma^\mu v_{s'}(p) = 2p^\mu\delta_{ss'};\\
&\bar{u}_{s'}(p')\gamma^+\gamma_5 u_s(p) = 2\sqrt{p^+p'^+}\,\delta_{ss'}\mathrm{sign}(s);\\
&\bar{u}_s(p)\gamma^+ u_{s'}(p') = \bar{v}_s(p)\gamma^+ v_{s'}(p') = 2\sqrt{p^+p'^+}\,\delta_{ss'}\\
&\bar{u}_s(\boldsymbol{p})\gamma^0 v_{s'}(-\boldsymbol{p}) = 0
\end{aligned} \tag{A.32}$$

Spinor vertices In general, the spinor vertex can be written as,

$$\begin{aligned}
V_n =&\bar{u}_{s'}(p')\not{\epsilon}_1\not{\epsilon}_2\cdots\not{\epsilon}_n u_(p)\\
=&\frac{1}{4\sqrt{p^+p'^+}}\chi^\dagger_{s'}\gamma^0\gamma^+(p'+m)\not{\epsilon}_1\not{\epsilon}_2\cdots\not{\epsilon}_n(\not{p}+m)\gamma^+\chi_s\\
=&\frac{1}{2\sqrt{p^+p'^+}}\chi^\dagger_{s'}\Lambda_+(p'+m)\not{\epsilon}_1\not{\epsilon}_2\cdots\not{\epsilon}_n(\not{p}+m)\gamma^+\chi_s\\
=&\frac{1}{4\sqrt{p^+p'^+}}\mathrm{tr}\big[(\not{p}'+m)\not{\epsilon}_1\not{\epsilon}_2\cdots\not{\epsilon}_n(\not{p}+m)\gamma^+\chi_{ss'}\big]
\end{aligned} \tag{A.33}$$

Now the spinor vertex is turned into the trace of a string of gamma matrices, and

$$\chi_s\chi^\dagger_{s'} \triangleq \frac{1}{2}\chi_{ss'} = \frac{1}{2}\begin{cases} 1+\gamma_5, & s=+,s'=+ \\ 1-\gamma_5, & s=-,s'=- \\ -\gamma^R = -\gamma^1 - \mathrm{i}\gamma^2, & s=+,s'=- \\ \gamma^L = \gamma^1 - \mathrm{i}\gamma^2, & s=-,s'=+ \end{cases} \tag{A.34}$$

- scalar vertex:

$$\bar{u}_{s'}(p')u_s(p) = \sqrt{p^+p'^+} \times \begin{cases} \frac{m}{p^+} + \frac{m}{p'^+}, & s,s'=++,-- \\ \frac{p^R}{p^+} - \frac{p'^R}{p'^+} = \frac{p^1+\mathrm{i}p^2}{p^+} - \frac{p'^1+\mathrm{i}p'^2}{p'^+}, & s,s'=+,- \\ \frac{p'^L}{p'^+} - \frac{p^L}{p^+} = \frac{p'^1-\mathrm{i}p'^2}{p'^+} - \frac{p^1-\mathrm{i}p^2}{p^+}, & s,s'=-,+ \end{cases} \tag{A.35}$$

- pseudo scalar vertex:

$$\bar{u}_{s'}(p')\gamma_5 u_s(p) = \sqrt{p^+p'^+} \times \begin{cases} \frac{m}{p'^+} - \frac{m}{p^+}, & s,s'=++ \\ \frac{m}{p^+} - \frac{m}{p'^+}, & s,s'=-- \\ \frac{p^R}{p^+} - \frac{p'^R}{p'^+} = \frac{p^1+\mathrm{i}p^2}{p^+} - \frac{p'^1+\mathrm{i}p'^2}{p'^+}, & s,s'=+,- \\ \frac{p^L}{p^+} - \frac{p'^L}{p'^+} = \frac{p^1-\mathrm{i}p^2}{p^+} - \frac{p'^1-\mathrm{i}p'^2}{p'^+}, & s,s'=-,+ \end{cases} \tag{A.36}$$

- vector vertex:

$$\begin{aligned} \bar{u}_{s'}(p')\gamma^+u_s(p) =& 2\sqrt{p^+p'^+}\,\delta_{ss'} \\ \bar{u}_{s'}(p')\gamma^-u_s(p) =& \frac{2}{\sqrt{p^+p'^+}} \begin{cases} m^2 + p^Rp'^L, & s,s'=+,+ \\ m^2 + p^Lp'^R, & s,s'=-,- \\ m(p^R - p'^R), & s,s'=+,- \\ m(p'^L - p^L), & s,s'=-,+ \end{cases} \\ \bar{u}_{s'}(p')\gamma^Lu_s(p) =& 2\sqrt{p^+p'^+} \begin{cases} \frac{p'^L}{p'^+}, & s,s'=+,+ \\ \frac{p^L}{p^+}, & s,s'=-,- \\ \frac{m}{p'^+} - \frac{m}{p^+}, & s,s'=+,- \\ 0, & s,s'=-,+ \end{cases} \\ \bar{u}_{s'}(p')\gamma^Ru_s(p) =& 2\sqrt{p^+p'^+} \begin{cases} \frac{p^R}{p^+}, & s,s'=+,+ \\ \frac{p'^R}{p'^+}, & s,s'=-,- \\ 0, & s,s'=+,- \\ \frac{m}{p'^+} - \frac{m}{p^+}, & s,s'=-,+ \end{cases} \end{aligned} \tag{A.37}$$

- pseudo vector:

$$\bar{u}_{s'}(p')\gamma^+\gamma_5 u_s(p) = 2\sqrt{p^+p'^+}\delta_{ss'}\text{sign}(s)$$

$$\bar{u}_{s'}(p')\gamma^-\gamma_5 u_s(p) = \frac{2}{\sqrt{p^+p'^+}}\begin{cases} -m^2 + p'^L p^R, & s,s' = +,+ \\ m^2 - p'^R p^L, & s,s' = -,- \\ m(p^R + p'^R), & s,s' = +,- \\ m(p^L + p'^L), & s,s' = -,+ \end{cases}$$

$$\bar{u}_{s'}(p')\gamma^L\gamma_5 u_s(p) = 2\sqrt{p^+p'^+}\begin{cases} \frac{p'^L}{p'^+}, & s,s' = +,+ \\ -\frac{p^L}{p^+}, & s,s' = -,- \\ \frac{m}{p^+} + \frac{m}{p'^+}, & s,s' = +,- \\ 0, & s,s' = -,+ \end{cases} \tag{A.38}$$

$$\bar{u}_{s'}(p')\gamma^R\gamma_5 u_s(p) = 2\sqrt{p^+p'^+}\begin{cases} \frac{p^R}{p^+}, & s,s' = +,+ \\ -\frac{p'^R}{p'^+}, & s,s' = -,- \\ 0, & s,s = +,- \\ \frac{m}{p^+} + \frac{m}{p'^+}, & s,s = -,+ \end{cases}$$

Polarization of Gauge Bosons

Define the polarization vector:

$$\varepsilon^\mu_\lambda(k) = (\varepsilon^+_\lambda, \varepsilon^-_\lambda, \boldsymbol{\varepsilon}^\perp_\lambda) = (0, 2\boldsymbol{\epsilon}^\perp_\lambda \cdot \boldsymbol{k}^\perp/k^+, \boldsymbol{\epsilon}^\perp_\lambda), \quad (\lambda = \pm 1) \tag{A.39}$$

where $\boldsymbol{\epsilon}^\perp_\pm = \frac{1}{\sqrt{2}}(1, \pm\mathrm{i})$. In fact, $\varepsilon^L_\lambda = \sqrt{2}\delta_{\lambda,+}, \varepsilon^R_\lambda = \sqrt{2}\delta_{\lambda,-}$. This definition satisfies the light-cone gauge $\omega \cdot A = A^+ = 0$ and Lorenz condition $\partial_\mu A^\mu = 0$,

$$\omega_\mu \varepsilon^\mu_\lambda(k) = \varepsilon^+_\lambda(k) = 0, \quad k_\mu \varepsilon^\mu_\lambda(k) = 0. \tag{A.40}$$

Polarization identities:

- orthogonality:

$$\varepsilon^\mu_\lambda(k)\varepsilon^*_{\lambda'\mu}(k) = -\delta_{\lambda,\lambda'}; \tag{A.41}$$

- helicity sum:

$$\sum_{\lambda=\pm}\varepsilon_\lambda^{i*}(k)\varepsilon_\lambda^j(k)=\delta^{ij},\quad d^{\mu\nu}\equiv\sum_{\lambda=\pm}\varepsilon_\lambda^{\mu*}(k)\varepsilon_\lambda^\nu(k)=-g^{\mu\nu}+\frac{\omega^\mu k^\nu+\omega^\nu k^\mu}{\omega\cdot k}-\omega^\mu\omega^\nu\frac{k^2}{(\omega\cdot k)^2}. \tag{A.42}$$

  In particular, if k is on-shell, i.e. $k^2=0$, the second identity is reduced to

$$\sum_{\lambda=\pm}\varepsilon_\lambda^{\mu*}(k)\varepsilon_\lambda^\nu(k)=-g^{\mu\nu}+\frac{\omega^\mu k^\nu+\omega^\nu k^\mu}{\omega\cdot k}. \tag{A.43}$$

- crossing symmetry:

$$\varepsilon_\lambda^{\mu*}(k)=\varepsilon_{-\lambda}^\mu(k)=\varepsilon_{-\lambda}^\mu(-k) \tag{A.44}$$

where $\omega^\mu=(1,0,0,-1)$, is the null normal vector of light-front, $\omega\cdot\omega=0$, $\omega\cdot v=v^+$.

Polarization of Massive Vector Bosons

Define the spin vector for the massive vector bosons:

$$e_\lambda(k)=(e_\lambda^+(k),e_\lambda^-(k),\boldsymbol{e}_\lambda^\perp(k))=\begin{cases}\frac{1}{m}\big(k^+,(\boldsymbol{k}_\perp^2-m^2)/k^+,\boldsymbol{k}^\perp\big), & \lambda=0\\ \big(0,2\boldsymbol{\epsilon}^\perp\cdot\boldsymbol{k}^\perp/k^+,\boldsymbol{\epsilon}^\perp\big), & \lambda=\pm1\end{cases} \tag{A.45}$$

where where $\boldsymbol{\epsilon}_\pm^\perp=\frac{1}{\sqrt{2}}(1,\pm\mathrm{i})$, and $\boldsymbol{\epsilon}_+^{\perp*}=\boldsymbol{\epsilon}_-^\perp$, $m^2=k_\mu k^\mu\triangleq k^2$ is the mass of the particle.

Spin identities:

- Proca equation, $k_\mu e_\lambda^\mu(k)=0$.

- orthogonality:

$$e_\lambda^\mu(k)e_{\lambda'\mu}^*(k)=-\delta_{\lambda,\lambda'}; \tag{A.46}$$

- spin sum:

$$K^{\mu\nu}\equiv\sum_{\lambda=-1}^{+1}e_\lambda^{\mu*}(k)e_\lambda^\nu(k)=-g^{\mu\nu}+\frac{k^\mu k^\nu}{k^2}. \tag{A.47}$$

  $k^\mu K_{\mu\nu}(k)=k^\mu k^\nu K_{\mu\nu}(k)=0$.

- crossing symmetry:

$$e_\lambda^{\mu*}(k)=e_{-\lambda}^\mu(k),\quad e_\lambda^\mu(-k)=(-1)^{\lambda+1}e_\lambda^\mu(k); \tag{A.48}$$

APPENDIX B. JACOBI DIFFERENTIAL EQUATION

The Jacobi polynomial $P_n^{(\alpha,\beta)}(z)$ is defined as [109],

$$P_n^{(\alpha,\beta)}(z) = \frac{1}{2^n}\sum_{k=0}^{n}\binom{n+\alpha}{k}\binom{n+\beta}{n-k}(z-1)^{n-k}(z+1)^k. \tag{B.1}$$

The Jacobi polynomials satisfy the following differential equation [109],

$$(1-z^2)\frac{\mathrm{d}^2}{\mathrm{d}z^2}P_n^{(\alpha,\beta)}(z)+\big[\beta-\alpha-(\alpha+\beta+2)z\big]\frac{\mathrm{d}}{\mathrm{d}z}P_n^{(\alpha,\beta)}(z)+n(n+\alpha+\beta+1)P_n^{(\alpha,\beta)}(z)=0. \tag{B.2}$$

for $z\in(-1,1)$. The longitudinal basis functions are defined as,

$$\chi_l^{(\alpha,\beta)}(x) = \mathcal{N}_l(1-x)^{\frac{\alpha}{2}}x^{\frac{\beta}{2}}P_l^{(\alpha,\beta)}(2x-1), \tag{B.3}$$

where $x\in(0,1)$, and $\mathcal{N}_l$ is a normalization constant. Let $z=2x-1$, or $x=\frac{1}{2}(1+z)$. Then, $1-z=2(1-x)$, $1+z=2x$, and $1-x=\frac{1}{2}(1-z)$. Eq. (B.3) becomes,

$$\chi_l^{(\alpha,\beta)}(\tfrac{1}{2}(1+z)) = \mathcal{N}_l\,2^{\frac{\alpha+\beta}{2}}(1-z)^{\frac{\alpha}{2}}(1+z)^{\frac{\beta}{2}}P_l^{(\alpha,\beta)}(z) \equiv \mathcal{N}_l\,2^{\frac{\alpha+\beta}{2}}u_l^{(\alpha,\beta)}(z), \tag{B.4}$$

Let us derive the differential equation satisfied by $u_l^{(\alpha,\beta)}(z) = (1-z)^{\frac{\alpha}{2}}(1+z)^{\frac{\beta}{2}}P_l^{(\alpha,\beta)}(z)$. Now, $P_l^{(\alpha,\beta)}(z) = (1-z)^{-\frac{\alpha}{2}}(1+z)^{-\frac{\beta}{2}}u_l^{(\alpha,\beta)}(z)$. Differentiating both size once, we get,

$$\frac{\mathrm{d}}{\mathrm{d}z}P_l^{(\alpha,\beta)}(z) = (1-z)^{-\frac{\alpha}{2}}(1+z)^{-\frac{\beta}{2}}\Big[\frac{\mathrm{d}}{\mathrm{d}z}u_l^{(\alpha,\beta)}(z)+\frac{1}{2}\Big(\frac{\alpha}{1-z}+\frac{\beta}{1+z}\Big)u_l^{(\alpha,\beta)}(z)\Big]. \tag{B.5}$$

Differentiating both size again, we get,

$$\begin{aligned}\frac{\mathrm{d}^2}{\mathrm{d}z^2}P_l^{(\alpha,\beta)}(z) &= (1-z)^{-\frac{\alpha}{2}}(1+z)^{-\frac{\beta}{2}}\Big[\frac{\mathrm{d}^2}{\mathrm{d}z^2}u_l^{(\alpha,\beta)}(z)+\Big(\frac{\alpha}{1-z}-\frac{\beta}{1+z}\Big)\frac{\mathrm{d}}{\mathrm{d}z}u_l^{(\alpha,\beta)}(z)\\ &+\frac{\alpha}{2}\Big(1+\frac{\alpha}{2}\Big)\frac{1}{(1-z)^2}u_l^{(\alpha,\beta)}(z)+\frac{\beta}{2}\Big(1+\frac{\beta}{2}\Big)\frac{1}{(1+z)^2}u_l^{(\alpha,\beta)}(z)-\frac{\alpha\beta}{2}\frac{1}{1-z^2}u_l^{(\alpha,\beta)}(z)\Big].\end{aligned} \tag{B.6}$$

Substituting Eq. (B.5–B.6) into Eq. (B.2), we get,

$$\frac{\mathrm{d}}{\mathrm{d}z}\Big((1-z^2)\frac{\mathrm{d}}{\mathrm{d}z}u_l^{(\alpha,\beta)}(z)\Big)-\frac{1}{2}\Big(\frac{\alpha^2}{1-z}+\frac{\beta^2}{1+z}\Big)u_l^{(\alpha,\beta)}(z)+\big(l+\tfrac{1}{2}(\alpha+\beta)\big)\big(l+\tfrac{1}{2}(\alpha+\beta)+1\big)u_l^{(\alpha,\beta)}(z)=0. \tag{B.7}$$

Plugging Eq. (B.3) in the above Eq. (B.7),

$$\frac{\mathrm{d}}{\mathrm{d}x}\Big(x(1-x)\frac{\mathrm{d}}{\mathrm{d}x}\chi_l^{(\alpha,\beta)}(x)\Big)-\frac{1}{4}\Big(\frac{\alpha^2}{1-x}+\frac{\beta^2}{x}\Big)\chi_l^{(\alpha,\beta)}(x)+\big(l+\tfrac{1}{2}(\alpha+\beta)\big)\big(l+\tfrac{1}{2}(\alpha+\beta)+1\big)\chi_l^{(\alpha,\beta)}(x)=0. \tag{B.8}$$

If $\alpha=\beta\equiv\mu$, Eq. (B.7) becomes,

$$\frac{\mathrm{d}}{\mathrm{d}z}\Big((1-z^2)\frac{\mathrm{d}}{\mathrm{d}z}u_l^{(\mu,\mu)}(z)\Big)-\frac{\mu^2}{1-z^2}u_l^{(\mu,\mu)}(z)+\big(l+\mu\big)\big(l+\mu+1\big)u_l^{(\mu,\mu)}(z)=0. \tag{B.9}$$

This equation is the Legendre differential equation, whose solutions are the *Legendre functions*: $c_1P^{\mu}_{l+\mu}(z)+c_2Q^{\mu}_{l+\mu}(z)$, where $P^{\mu}_{l+\mu}(z)$ and $Q^{\mu}_{l+\mu}(z)$ are the associated Legendre functions of the first and second kinds [109]. The coefficients can be determined from the boundary condition[1] $u_l^{(\mu,\mu)}(\pm1)=0$ and the normalization.

[1] If μ is an integer, the boundary condition is $u_l^{(\mu,\mu)}(\pm1)=0$ always satisfied by $P^{\mu}_{l+\mu}(z)$. However, for non-integer, to the author's knowledge, it depends on the conventions, and some popular definitions of $P^{\mu}_{l+\mu}(z)$ do not satisfy this boundary condition. On the other hand, the definition involving Jacobi polynomial, $(1-z)^{\frac{\mu}{2}}(1+z)^{\frac{\mu}{2}}P_l^{(\mu,\mu)}(z)$, always satisfies this boundary condition.

APPENDIX C. ANGULAR INTEGRALS

The transverse integrations read,

$$\int \frac{\mathrm{d}^2 q_\perp}{(2\pi)^2} \int \frac{\mathrm{d}^2 q'_\perp}{(2\pi)^2}\, \phi^*_{n'm'}(\boldsymbol{q}'_\perp)\phi_{nm}(\boldsymbol{q}_\perp) \times \frac{S_{s,\bar{s},s',\bar{s}'}(\sqrt{x(1-x)}\boldsymbol{q}_\perp, x, \sqrt{x'(1-x')}\boldsymbol{q}'_\perp, x')}{\frac{1}{2}\big(\sqrt{x'(1-x)}\boldsymbol{q}_\perp - \sqrt{x(1-x')}\boldsymbol{q}'_\perp\big)^2 + \frac{1}{2}\big(\sqrt{x'(1-x)}\boldsymbol{q}'_\perp - \sqrt{x(1-x')}\boldsymbol{q}_\perp\big)^2 + \Delta}. \quad \text{(C.1)}$$

where $\boldsymbol{q}_\perp = \boldsymbol{k}_\perp/\sqrt{x(1-x)}$, $\boldsymbol{q}'_\perp = \boldsymbol{k}'_\perp/\sqrt{x'(1-x')}$, $\Delta = \frac{1}{2}(x-x')^2\big[\frac{1}{xx'} + \frac{1}{(1-x)(1-x')}\big]m_f^2 + \mu_g^2 > 0$, and the spinor matrix elements are given in Table 2.1.

First, note that the spinor matrix elements takes the form of q, q', q^*q' or their complex conjugate, where $v = v_x + iv_y$, $v^* = v_x - iv_y$ are the complex representation of the 2-dimensional transverse vector $\boldsymbol{v}_\perp$. These terms can be absorbed in to the 2-dimensional harmonic oscillator functions using the following identities,

$$\begin{aligned} q\,\phi_{n,m}(\boldsymbol{q}_\perp) &= \begin{cases} \sqrt{n+|m|+1}\,b\,\phi_{n,m+1}(\boldsymbol{q}_\perp) - \sqrt{n}\,b\,\phi_{n-1,m+1}(\boldsymbol{q}_\perp), & m \geq 0 \\ \sqrt{n+|m|}\,b\,\phi_{n,m+1}(\boldsymbol{q}_\perp) - \sqrt{n+1}\,b\,\phi_{n+1,m+1}(\boldsymbol{q}_\perp), & m < 0; \end{cases} \\ q^*\,\phi_{n,m}(\boldsymbol{q}_\perp) &= \begin{cases} \sqrt{n+|m|+1}\,b\,\phi_{n,m-1}(\boldsymbol{q}_\perp) - \sqrt{n}\,b\,\phi_{n-1,m-1}(\boldsymbol{q}_\perp), & m \leq 0 \\ \sqrt{n+|m|}\,b\,\phi_{n,m-1}(\boldsymbol{q}_\perp) - \sqrt{n+1}\,b\,\phi_{n+1,m-1}(\boldsymbol{q}_\perp), & m > 0. \end{cases} \end{aligned} \quad \text{(C.2)}$$

where b is the basis scale parameter for harmonic oscillator functions.

Then, the rest of the angular integrations involves only $\exp(im\theta)$ and dot-product in the denominator, and takes the form,

$$I_{n,m,n',m'} \equiv \int \frac{\mathrm{d}^2 q_\perp}{(2\pi)^2} \int \frac{\mathrm{d}^2 q'_\perp}{(2\pi)^2}\, \phi^*_{n'm'}(\boldsymbol{q}'_\perp)\phi_{nm}(\boldsymbol{q}_\perp) \times \frac{1}{\frac{1}{2}\big(\sqrt{x'(1-x)}\boldsymbol{q}_\perp - \sqrt{x(1-x')}\boldsymbol{q}'_\perp\big)^2 + \frac{1}{2}\big(\sqrt{x'(1-x)}\boldsymbol{q}'_\perp - \sqrt{x(1-x')}\boldsymbol{q}_\perp\big)^2 + \Delta}. \quad \text{(C.3)}$$

To evaluate the angular integrations[1], we first perform a Talmi-Moshinsky transformation [47, 56] on the harmonic oscillator functions:

$$\phi_{nm}(\boldsymbol{q}_\perp)\phi^*_{n'm'}(\boldsymbol{q}'_\perp) = \sum_{N,M,N',M'} \mathcal{M}^{N,M,N',-M'}_{n,m,n',-m'}\, \phi_{NM}(\boldsymbol{Q}_\perp)\phi^*_{N'M'}(\boldsymbol{Q}'_\perp). \tag{C.4}$$

where the variables $\boldsymbol{Q}_\perp$ and $\boldsymbol{P}_\perp$ are,

$$\boldsymbol{Q}_\perp = \frac{1}{\sqrt{2}}(\boldsymbol{q}_\perp + \boldsymbol{q}'_\perp), \quad \boldsymbol{Q}'_\perp = \frac{1}{\sqrt{2}}(\boldsymbol{q}_\perp - \boldsymbol{q}'_\perp), \tag{C.5}$$

The transformation coefficients, $\mathcal{M}^{N,M,N',-M'}_{n,m,n',-m'}$, can be obtained analytically [47, 178]. Note that the Talmi-Moshinsky coefficients are proportional to Kronecker deltas:

$$\mathcal{M}^{N,M,N',M'}_{n,m,n',-m'} \propto \delta_{M-M',m-m'}\delta_{2N+|M|+2N'+|M'|,2n+|m|+2n'+|m'|}, \tag{C.6}$$

representing the energy conservation and the angular momentum conservation, respectively. Then the integral becomes,

$$\begin{aligned} I_{n,m,n',m'} =& \sum_{N,M,N',M'} \mathcal{M}^{N,M,N',-M'}_{n,m,n',-m'} \int \frac{\mathrm{d}^2 Q_\perp}{(2\pi)^2} \int \frac{\mathrm{d}^2 Q'_\perp}{(2\pi)^2}\, \phi_{NM}(\boldsymbol{Q}_\perp)\phi^*_{N'M'}(\boldsymbol{Q}'_\perp) \\ &\times \frac{1}{\frac{1}{2}\big(\sqrt{x'(1-x)} - \sqrt{x(1-x')}\big)^2 \boldsymbol{Q}^2_\perp + \frac{1}{2}\big(\sqrt{x'(1-x)} + \sqrt{x(1-x')}\big)^2 \boldsymbol{Q}'^2_\perp + \Delta} \\ =& \frac{\delta_{m,m'}}{2\pi} \sum_{N=0}^{n+n'+|m|} \mathcal{M}^{N,0,N',0}_{n,m,n',-m'} \int_0^\infty \mathrm{d}\rho \int_0^\infty \mathrm{d}\sigma \exp\big[-\tfrac{1}{2}(\rho+\sigma)\big] L_N(\rho) L_{N'}(\sigma) \\ &\times \frac{1}{\frac{1}{2}\big(\sqrt{x'(1-x)} - \sqrt{x(1-x')}\big)^2 \rho + \frac{1}{2}\big(\sqrt{x'(1-x)} + \sqrt{x(1-x')}\big)^2 \sigma + \frac{\Delta}{b^2}}. \end{aligned} \tag{C.7}$$

where, $N' = n + n' + |m| - N$ due to the Kronecker deltas. The residual radial integrals are evaluated numerically.

[1] It is also possible to evaluate the angular integration directly. Then one arrives an angular integral

$$\int_0^{2\pi} \mathrm{d}\phi \frac{e^{im\phi}}{1 - a\cos\phi} = \frac{2\pi}{1+a} \frac{{}_3F_2\left(\frac{1}{2}, 1, 1; 1-m, 1+m; \frac{2a}{1+a}\right)}{\Gamma(1-m)\Gamma(1+m)}, \quad (0 < a < 1)$$

The hypergeometric functions are not easy to use. Using the identify $\cos m\phi = \Re(\cos\phi + i\sin\phi)^m$,

$$\cos m\phi = (\cos\phi)^m \sum_{i=0}^{\lfloor m/2 \rfloor} \binom{m}{2i} (1 - \csc^2\phi)^i,$$

one reduces $\cos m\phi$ to the power of $\cos\phi$. By expressing the ratio with minimal denominator, one are left with

$$\int_0^{2\pi} \frac{\mathrm{d}\phi}{1 - a\cos\phi} = \frac{2\pi}{\sqrt{1-a^2}}$$

The problem with this method is that we don't get a closed-form expression.

APPENDIX D. GAUSS QUADRATURES

Gauss quadratures approximate the integral with summation:

$$\int_a^b \mathrm{d}x\, w(x) f(x) = \sum_{i=1}^{n} w_i f(x_i) + R_n, \tag{D.1}$$

where n is the order of the quadrature, x_i and w_i are the pre-chosen abscissas and weights, related to the orthogonal polynomials, specifically x_i is the i-th zero of the associated orthogonal polynomial. The residual term $R_n \propto f^{(2n)}(\xi)$ for some ξ. The Gauss quadratures are exact for lower order polynomials.

Several commonly used Gauss quadratures are given in Table D.1. More details can be seen in Ref. [109].

Integrals over non-standard intervals can be done similarly by a change of variable. For example,

$$\begin{aligned}\int_a^b \mathrm{d}z\, f(z) =& \tfrac{1}{2}(b-a)\int_{-1}^{+1} \mathrm{d}x\, f\big(\tfrac{1}{2}(b+a)+\tfrac{1}{2}(b-a)x\big)\\ \approx& \tfrac{1}{2}(b-a)\sum_i w_i\, f(\tfrac{1}{2}(b+a)+\tfrac{1}{2}(b-a)x_i)\\ \equiv& \sum_i W_i\, f(z_i)\end{aligned} \tag{D.2}$$

where x_i and w_i are the standard Gauss-Legendre quadratures and $z_i \equiv \frac{1}{2}(b+a)+\frac{1}{2}(b-a)x_i$, and $W_i \equiv \frac{1}{2}(b-a)w_i$ are the new abscissas and weights for the integration over interval (a,b).

Table D.1: Some commonly used Gauss quadratures.

polynomials	interval (a, b)	$w(x)$	abscissas x_i	weights w_i
Legendre $P_n(z)$	$(-1, 1)$	1	i-th root of $P_n(z)$	$\frac{2(1-x_i^2)}{(n+1)^2[P_{n+1}(x_i)]^2}$
Jacobi $P_n^{(\alpha,\alpha)}(z)$	$(-1, 1)$	$(1-x^2)^\alpha$	i-th root of $P_n^{(\alpha,\alpha)}(z)$	$\frac{[\Gamma(n+\alpha+1)]^2(n+\alpha+1)^2}{\Gamma(n+2\alpha+1)n!(n+2\alpha+1)^2}\frac{2^{2\alpha+1}(1-x_i^2)}{(n+1)^2[P_{n+1}^{(\alpha,\alpha)}(x_i)]^2}$
Jacobi $P_n^{(\alpha,\beta)}(z)$	$(-1, 1)$	$(1-x)^\alpha(1+x)^\beta$	i-th root of $P_n^{(\alpha,\beta)}(z)$	$\frac{\Gamma(n+\alpha+1)\Gamma(n+\beta+1)(2n+\alpha+\beta+2)^2}{\Gamma(n+\alpha+\beta+1)n!4(n+\alpha+\beta+1)^2}\frac{2^{\alpha+\beta+1}(1-x_i^2)}{(n+1)^2[P_{n+1}^{(\alpha,\beta)}(x_i)]^2}$
Laguerre $L_n(z)$	$(0, \infty)$	$\exp(-x)$	i-th root of $L_n(z)$	$\frac{x_i}{(n+1)^2[L_{n+1}(x_i)]^2}$
Associated Laguerre $L_n^\alpha(z)$	$(0, \infty)$	$x^\alpha\exp(-x)$	i-th root of $L_n^\alpha(z)$	$\frac{\Gamma(n+\alpha+1)x_i}{n!(n+1)^2[L_{n+1}^\alpha(x_i)]^2}$
Hermite $H_n(z)$	$(-\infty, \infty)$	$\exp(-x^2)$	i-th root of $H_n(z)$	$\frac{2^{n-1}n!\sqrt{\pi}}{n^2[H_{n-1}(x_i)]^2}$

BIBLIOGRAPHY

[1] ATLAS Collaboration, Phys. Lett. B, **716**, 1 (2012); [arXiv:1207.7214 [hep-ex]].

[2] CMS Collaboration, Phys. Lett. B, **716**, 30 (2012); [arXiv:1207.7235 [hep-ex]].

[3] T. Aoyama, M. Hayakawa, T. Kinoshita, and M. Nio, Phys. Rev. D **91**, 033006 (2015); [arXiv:1412.8284 [hep-ph]].

[4] P.J. Mohr, D.B. Newell, B.N. Taylor, "CODATA Recommended Values of the Fundamental Physical Constants: 2014", arXiv:1507.07956 [physics.atom-ph].

[5] S.J. Brodsky, P. Hoyer, Phys. Rev. D **83**, 045026 (2011); [arXiv:1009.2313 [hep-ph]].

[6] P.A.M. Dirac, Rev. Mod. Phys. **21**, 392 (1949).

[7] S. Weinberg: "The quantum theory of fields", Vol. 1. "Foundations", Cambridge University Press, 2005, ISBN: 9780521670531.

[8] H. Leutwyler, and J. Stern, Ann. Phys. **112**, 94 (1978).

[9] M. Burkardt, Adv. Nucl. Phys. **23**, 1, (1996); [arXiv:hep-ph/9505259].

[10] S.J. Brodsky, H.-C. Pauli and S. Pinsky, Phys. Rep. **301**, 299 (1998); [arXiv:hep-ph/9705477].

[11] A. Harindranath, "Light Front Field Theory and Light Front QCD", Lecture Notes, 2000.

[12] T. Heinzl, "Light-Cone Quantization: Foundations and Applications", H. Latal, W. Schweiger (Eds.): Lect. Notes Phys. **572** (2001) 55-142.

[13] A. Zee, "Quantum Field Theory in a Nutshell", Princeton University Press, Princeton, NJ, 2003. ISBN: 987-0-691-01019-9.

[14] K.G. Wilson, Phys. Rev. D **10**, 2445 (1974).

[15] J.S. Schwinger, Proc. Nat. Acad. Sc. **37** 452 (1951); *ibid.* **37**, 455 (1951).

[16] P. Maris, C.D. Roberts, Int. J. Mod. Phys. E **12**, 297 (2003).

[17] B.L.G. Bakker *et al.*, Nucl. Phys. Proc. Suppl. **251-252**, 165 (2014); [arXiv:1309.6333 [hep-ph]].

[18] M.E. Peskin, D.V. Schroeder, "An Introduction to Quantum Field Theory", Westview Press, 1995. ISBN-13 978-0-201-50397-5.

[19] P.A.M. Dirac, Can. Jour. Math. **2**, 129 (1950).

[20] P.A.M. Dirac, "Lectures on Quantum Mechanics", Belfer Graduate School of Science, Yeshiva University, 1964.

[21] J.L. Anderson, P.G. Bergman, Phys. Rev. **83**,1018 (1951).

[22] L.D. Faddeev, R. Jackiw, Phys. Rev. Lett. **60**, 1692 (1988).

[23] R. Jackiw, hep-th/9306075, MIT-CTP-2215, C93-06-28.4.

[24] Julian Schwinger, Phys. Rev. **82**, 914 (1951).

[25] Julian Schwinger, Phys. Rev. **91**, 713 (1953).

[26] George Leibbrandt, Phys. Rev. D **29**, 1699 (1984).

[27] John B. Kogut, Davison E. Soper, Phys. Rev. D **1**, 2901 (1970).

[28] S.J. Chang, R.G. Root, and T.M. Yan, Phys. Rev. D **7**, 1133 (1973).

[29] T.-M. Yan, quantization of coupled spin-one fields", Phys. Rev. D **7**, 1760 (1973).

[30] E. Tomboulis, Phys. Rev. D **8**, 2736 (1973).

[31] Aharon Casher, Phys. Rev. D **14**, 452 (1976).

[32] Wei-Min Zhang and Avaroth Harindranath, Phys. Rev. D **48**, 4868 (1993).

[33] S. Weinberg, Phys. Rev. **150**, 1313 (1966).

[34] J. Carbonell, B. Desplanques, V.A. Karmanov, and J.-F. Mathiot, Phys. Rep. **300**, 215 (1998); [arXiv:nucl-th/9804029].

[35] V.A. Karmanov, J.-F Mathiot, A.V. Smirnov, Phys. Rev. D **77**, 085028 (2008); [arXiv:0801.4507 [hep-th]].

[36] R.J. Perry, A. Harindranath, and K.G. Wilson, Phys. Rev. Lett. **65**, 2959 (1990).

[37] I. Tamm, J. Phys. (Moscow) **9**, 449 (1945).

[38] S.M. Dancoff, Phys. Rev. **78**, 382 (1950).

[39] M. Gell-Mann and F. Low, Phys. Rev. **84**, 350 (1951).

[40] K.G. Wilson, D.G. Robertson, arXiv:hep-th/9411007.

[41] H.-C. Pauli and S.J. Brodsky, Phys. Rev. D **32**, 1993 (1985).

[42] H.-C. Pauli and S.J. Brodsky, Phys. Rev. D **32**, 2001 (1985).

[43] J.R. Hiller, Nucl. Phys. Proc. Suppl. **90**,170 (2000); [arXiv:hep-ph/0007309].

[44] Leonard Susskind, arXiv:hep-th/9704080.

[45] Nathan Seiberg, Phys. Rev. Lett. **79**, 3577 (1997). [arXiv:hep-th/9710009];

[46] J.P. Vary, H. Honkanen, Jun Li, P. Maris, S.J. Brodsky, A. Harindranath, G.F. de Teramond, P. Sternberg, E.G. Ng, and C. Yang, Phys. Rev. C **81**, 035205 (2010); [arXiv:0812.1819 [nucl-th]].

[47] Yang Li, P.W. Wiecki, X. Zhao, P. Maris and J.P. Vary, Proc. Int. Conf. Nucl. Theory. Supercomputing Era (NTSE-2013), Ames, IA, USA, May 1–17, 2013, Eds. A.M. Schirokov and A.I. Mazur. Pacific National University, Khabarovsk, 2014, p.136.

[48] P. Maris, P. Wiecki, Yang Li, X. Zhao and J.P. Vary, Acta Phys. Polon. Supp., **6**, 321 (2013).

[49] S.J. Brodsky, G.F. de Teramond, H.G. Dosch, J. Erlich, Phys. Rept. **584**, 1 (2015); [arXiv:1407.8131 [hep-ph]].

[50] D. Gloeckner and R. Lawson, Phys. Lett. B **53**, 313 (1974).

[51] C. Lanczos, J. Res. Natl. Bur. Stand. **45**, 255 (1950). W.E. Arnoldi, Quart. Appl. Math. **9**, 17 (1951).

[52] B.R. Barrett, P. Navrátil, J.P. Vary, Prog. Part. Nucl. Phys. **69**, 131 (2013).

[53] H. Honkanen, P. Maris, J.P. Vary and S.J. Brodsky, Phys. Rev. Lett. **106**, 061603 (2011); [arXiv:1008.0068 [hep-ph]].

[54] X. Zhao, H. Honkanen, P. Maris, J.P. Vary, S.J. Brodsky, Phys. Lett. B **737**, 65-69 (2014); [arXiv:1402.4195 [nucl-th]].

[55] D. Chakrabarti, X. Zhao, H. Honkanen, R. Manohar, P. Maris, and J.P. Vary, Phys. Rev. D **89**, 116004 (2014); [arXiv:1403.0704v1 [hep-ph]].

[56] P. Wiecki, Yang Li, X. Zhao, P. Maris, J.P. Vary, Phys. Rev. D **91**, 105009 (2015); [arXiv:1404.6234 [nucl-th]].

[57] J.P. Vary, P. Wiecki, Yang Li, X. Zhao, P. Maris, Manuscript in preparation.

[58] X. Zhao, A. Ilderton, P. Maris, J.P. Vary, Phys. Lett. B **726**, 856 (2013); [arXiv:1309.5338 [nucl-th]].

[59] X. Zhao, A. Ilderton, P. Maris, J.P. Vary, Phys. Rev. D **88**, 065014 (2013); [arXiv:1303.3273 [nucl-th]].

[60] Yang Li, P. Maris, X. Zhao, J.P. Vary, "Quarkonium in a holographic basis", arXiv:1509.07212 [hep-ph].

[61] K.G. Wilson, T.S. Walhout, A. Harindranath, W.M. Zhang, R.J. Perry, and S.D. Głazek, Phys. Rev. D **49**, 6720 (1994).

[62] C. Bloch and J. Horowitz, Nucl. Phys. **8**, 91 (1958).

[63] C. Bloch, Nucl. Phys. **6**, 329 (1958).

[64] S. Okubo, Prog. Theor. Phys. **12**, 603 (1954).

[65] K. Suzuki and S.Y. Lee, Progr. Theor. Phys. **64**, 2091 (1980).

[66] R.J. Perry, Ann. Phys. **232**, 116 (1994); [arXiv:hep-th/9402015].

[67] Grangé, P. Neveu, A., Pauli, H.C., Pinsky, S., Werner, E. Eds., "New Non-Perturbative Methods and Quantization on the Light Cone", pp. 81–88, Springer Berlin Heidelberg (1998) ISBN: 978-3-540-64520-7; [arXiv:hep-th/9706053].

[68] S.D. Głazek and K.G. Wilson, Phys. Rev. D **48**, 5863 (1993).

[69] S.D. Głazek and K.G. Wilson, Phys. Rev. D **49**, 4214 (1994).

[70] F. Wegner, Ann. Physik. **3**, 77 (1994).

[71] M. Burkardt, Phys.Rev. D49 (1994) 5446; [hep-th/9312006].

[72] M. Burkardt and S. Dalley, Prog. Part. Nucl. Phys. **48**, 317 (2002); [hep-ph/0112007].

[73] S.S. Chabysheva and J.R. Hiller, Phys. Lett. B **711**, 417 (2012).

[74] N. Brambilla, *et al.*, Eur. Phys. J. C **71**, 1534 (2011); [arXiv:1010.5827 [hep-ph]].

[75] T. Applelquist, R. M. Barnett, K. Lane, Ann. Rev. Nucl. Part. Sci. **28**, 387 (1978).

[76] S. Godfrey and N. Isqur, Phys. Rev. D **32**, 189 (1985).

[77] N. Brambilla, A. Pineda, J. Soto, and A. Vairo, Rev. Mod. Phys. **77**, 1423 (2005); [arXiv:hep-ph/0410047].

[78] M. Neubert, Phys. Rept. **245**, 259 (1994); [arXiv:hep-ph/9306320].

[79] M.S. Bhagwat, P. Maris, Phys. Rev. C **77**, 025203 (2008); [arXiv:nucl-th/0612069].

[80] M. Blank and A. Krassnigg, Phys. Rev. D **84**, 096014 (2011); [arXiv:1109.6509 [hep-ph]].

[81] T. Hilger, C. Popovici, M. Gomez-Rocha and A. Krassnigg, Phys. Rev. D **91**, 034013 (2015); [arXiv:1409.3205 [hep-ph]].

[82] C.S. Fischer, S. Kubrak, R. Williams, Eur. Phys. J. A **51**, 10 (2015); [arXiv:1409.5076 [hep-ph]].

[83] C. McNeile, Lect. Notes Phys. **647**, 100 (2004); [arXiv:hep-lat/0210026].

[84] M.M. Brisudova and R. Perry, Phys. Rev. D **54**, 1831 (1996); [arXiv:hep-ph/9511443].

[85] M.M. Brisudova, R.J. Perry, KG. Wilson, Phys. Rev. Lett. **78**, 1227 (1997); [arXiv:hep-ph/9607280].

[86] S.D. Głazek and J. Młynik, Phys. Rev. D **74**, 105015 (2006); [arXiv:hep-th/0606235v2].

[87] T. Branz, T. Gutsche, V.E. Lyubovitskij, I. Schmidt, A. Vega, Phys. Rev. D **82**, 074022 (2010); [arXiv:1008.0268].

[88] T. Gutsche, V.E. Lyubovitskij, I. Schmidt, A. Vega, Phys. Rev. D **90**, 096007 (2014); [arXiv:1410.3738].

[89] H.-M. Choi, Phys. Rev. D **75**, 073016 (2007); [arXiv:hep-ph/0701263].

[90] M. Ablikim *et al.* (BESIII Collaboration), Phys. Rev. Lett. **110**, 252001 (2013); [arXiv:1303.5949 [hep-ex]]. Z.Q. Liu *et al.* (Belle Collaboration), Phys. Rev. Lett. **110**, 252002 (2013); [arXiv:1304.0121 [hep-ex]]. Erratum: Phys. Rev. Lett. **111**, 019901 (2013).

[91] R. Aaij *et al.* (LHCb collaboration), [arXiv:1507.03414 [hep-ex]].

[92] R. Alkofer and L. van Smekal, Phys. Rept. **353**, 281 (2001); [arXiv:hep-ph/0007355].

[93] M. Krautgartner, H.-C. Pauli and F. Wolz, Phys. Rev. D **45**, 3755 (1992).

[94] K.G. Wilson, Phys. Rev. D **2**, 1438 (1970).

[95] H.-C. Pauli, Eur. Phys. J. C **7**, 289 (1999); [arXiv:hep-th/9809005].

[96] A.P. Trawiński, S.D. Głazek, S.J. Brodsky, G.F. de Téramond, H.G. Dosch, Phys. Rev. D **90**, 074017 (2014); [arXiv:1403.5651v1 [hep-ph]].

[97] R. Bousso, Rev. Mod. Phys. **74**, 825 (2002); [arXiv:hep-th/0203101].

[98] L. Susskind, J. Math. Phys. **36**, 6377 (1995); [arXiv:hep-th/9409089].

[99] J.M. Maldacena, Adv. Theor. Math. Phys., **2**, 231 (1998); [arXiv:hep-th/9711200].

[100] S.S. Gubser, I.R. Klebanov, and A.M. Polyakov, Phys. Lett. B **428**, 105 (1998); [hep-th/9802109].

[101] E. Witten, Adv. Theor. Math. Phys. **2**, 253 (1998); [arXiv:hep-th/9802150].

[102] S.S. Gubser and A. Karch, Ann. Rev. Nucl. Part. Sci. **59**, 145 (2009); [arXiv:0901.0935 [hep-th]]

[103] J. Polchinski and M.J. Strassler, Phys. Rev. Lett. **88**, 031601 (2002).

[104] J. Erlich, E. Katz, D.T. Son, M.A. Stephanov, Phys. Rev. Lett. **95**, 261602 (2005);

[105] A. Karch, E. Katz, D.T. Son, M.A. Stephanov, Phys. Rev. D **74**, 015005 (2006).

[106] S.J. Brodsky, G.F. de Teramond and H.G. Dosch, Phys. Lett. B **729**, 3 (2014); [arXiv:1302.4105 [hep-th]].

[107] V. de Alfaro, S. Fubini and G. Furlan, Nuovo Cim. A **34**, 569 (1976).

[108] S.J. Brodsky and G.F. de Teramond, "AdS/CFT and light-front QCD," In Search for the Totally Unexpected in the LHC Era, Proceedings of the International School of Subnuclear Physics, Vol. 45, World Scientific Publishing Co. Singapore, 2009, [arXiv:0802.0514 [hep-ph]].

[109] M. Abramowitz, and I.A. Stegun. "Handbook of mathematical functions: with formulas, graphs, and mathematical tables", No. 55. Courier Corporation, 1964.

[110] G. Sterman et al., Rev. Mod. Physics **67**, 157 (1995).

[111] S.D. Głazek, Acta Phys. Polon. **B42**, 1933 (2011).

[112] S.S. Chabysheva, and J.R. Hiller, Ann. of Phys. **337**, 143-152 (2013); [arXiv:1207.7128 [hep-ph]].

[113] D. Chakrabarti and A. Harindranath, Phys. Rev. D **64**, 105002 (2001); [arXiv:hep-th/0110156].

[114] U. Trittmann and H.-C. Pauli, MPI H-V4-1997; [hep-th/9704215].

[115] H. Lamm and R.F. Lebed, J. Phys. G **41**, 125003 (2014); [arXiv:1311.3245 [hep-ph]].

[116] M. Mangin-Brinet, J. Carbonell, V.A. Karmanov, Phys. Rev. C **68**, 055203 (2003); [hep-th/0308179].

[117] R.J. Perry and A. Harindranath, Phys. Rev. D **43**, 4051 (1991).

[118] S. Głazek, A. Harindranath, S. Pinsky, J. Shigemitsu and K.G. Wilson, Phys. Rev. D **47**, 1599 (1993).

[119] J.R. Hiller and S.J. Brodsky, Phys. Rev. D **59**, 016006 (1998); [arXiv:hep-ph/9806541].

[120] S.A. Coon, M.I. Avetian, M.K.G. Kruse, U. van Kolck, P. Maris and J.P. Vary, Phys. Rev. C **86**, 054002 (2012); [arXiv:1205.3230 [nucl-th]].

[121] D.E. Soper, Phys. Rev. D **5**, 1956 (1972).

[122] S.J. Brodsky, S. Gardner and D.S. Hwang, Phys. Rev. D **73**, 036007 (2006); [arXiv:hep-ph/0601037v2];

[123] E. Anderson *et al.*, "LAPACK Users' Guide", 3rd Eds., Society for Industrial and Applied Mathematics, Philadelphia, PA, 1999.

[124] K.A. Olive *et al.* (Particle Data Group), Chin. Phys. C38, 090001 (2014), [`http://pdg.lbl.gov`].

[125] A.J. Bevan *et al.* (Belle Collaboration), Eur. Phy. J. C **74**, 3026 (2014); [arXiv:1406.6311 [hep-ex]].

[126] X. Ji, Phys. Rev. Lett. **78**, 610 (1997); [arXiv:hep-ph/9603249].

[127] X. Ji, Phys. Rev. D **55**, 7114 (1997); [arXiv:hep-ph/9609381].

[128] M. Burkardt, Phys. Rev. D **62**, 071503(R) (2000). Erratum: Phys. Rev. D **66**, 119903(E) (2002).

[129] S.J. Brodsky, M. Diehl, D.S. Hwang, Nucl. Phys. B **596**, 99 (2001); [arXiv:hep-ph/0009254].

[130] D.R. Yennie, M.M. Lévy, and D.G. Ravenhall, Rev. Mod. Phys. **29**, 144 (1957).

[131] J.P.B.C. de Melo and T. Frederico, Phys. Rev. C **55**, 2043 (1997); [arXiv:nucl-th/9706032v3].

[132] S.D. Drell and T.M. Yan, Phys. Rev. Lett. **24**, 181 (1970);

[133] G.B. West, Phys. Rev. Lett. **24**, 1206 (1970).

[134] Cédric Lorcé, Phys. Rev. D **79**, 113011 (2009).

[135] I.L. Grach and L.A. Kondratyuk, Sov. J. Nucl. Phys. **39**, 198 (1984).

[136] V.A. Karmanov, Nucl. Phys. A **608**, 316 (1996).

[137] J.J. Dudek, R.G. Edwards and D.G. Richards, Phys. Rev. D **73**, 074507 (2006); [arXiv:hep-ph/0601137].

[138] P. Maris, AIP Conf. Proc. **892**, 65–71 (2007); [arXiv:nucl-th/0611057].

[139] G.P. Lepage, S.J. Brodsky, Phys. Rev. D **22**, 2157 (1980).

[140] R. Van Royen, V.F. Weisskopf, Nuovo Cim. A **50**, 617 (1967); Nuovo Cim. A **51**, 583 (1967).

[141] W. Kwong, J.L. Rosner, C. Quigg, Ann. Rev. Nucl. Part. Sci. **37**, 325 (1987).

[142] D. Becirevic, G. Duplancic, B. Klajn, B. Melic and F. Sanfilippo, Nucl. Phys. B **883**, 306 (2014).

[143] C.T.H. Davies, C. McNeile, E. Follana, G.P. Lepage, H. Na, J. Shigemitsu (HPQCD Collaboration), Phys. Rev. D **82**, 114504 (2010); [arXiv:1008.4018 [hep-lat]].

[144] C. McNeile, C.T.H. Davies, E. Follana, K. Hornbostel, G.P. Lepage (HPQCD Collaboration), Phys. Rev. D **86**, 074503 (2012); [arXiv:1207.0994 [hep-lat]].

[145] G.C. Donald, C.T.H. Davies, R.J. Dowdall, E. Follana, K. Hornbostel, J. Koponen, G.P. Lepage, C. McNeile (HPQCD Collaboration), Phys. Rev. D **86**, 094501 (2012); [arXiv:1208.2855 [hep-lat]].

[146] B. Colquhoun, R.J. Dowdall, C.T.H. Davies, K. Hornbostel, G.P. Lepage (HPQCD Collaboration), Phys. Rev. D **91**, 074514 (2015); [arXiv:1408.5768 [hep-lat]].

[147] F. Jegerlehner, Nuovo Cim. C **34**, Supp. 1, 31 (2011); [arXiv:1107.4683 [hep-ph]].

[148] S.D. Głazek, K.G. Wilson, Phys. Rev. D **57**, 3558 (1998); [arXiv:hep-th/9707028].

[149] V.A. Karmanov, J.-F. Mathiot, A.V. Smirnov, Phys. Rev. D **82**, 056010 (2010); [arXiv:1006.5640 [hep-th]].

[150] V.A. Karmanov, J.-F. Mathiot and A.V. Smirnov, Phys. Rev. D **86**, 085006 (2012); [arXiv:1204.3257 [hep-th]].

[151] P. Grangé, J.-F. Mathiot, B. Mutet, and E. Werner, "Taylor-Lagrange renormalization scheme, Pauli-Villars subtraction, and light-front dynamics", Phys. Rev. D **82**, 025012 (2010); [arXiv:1006.5282 [hep-th]].

[152] Yang Li, V.A. Karmanov, P. Maris, J.P. Vary, Few-Body Syst. **56**, 495 (2015); [arXiv:1411.1707 [nucl-th]].

[153] Yang Li, V.A. Karmanov, P. Maris, J.P. Vary, Phys. Lett. B **748**, 278 (2015); [arXiv:1504.05233 [nucl-th]].

[154] D.S. Hwang and V.A. Karmanov, Nucl. Phys. **B 696**, 413 (2004); [arXiv:hep-th/0405035].

[155] S.J. Brodsky, J.R. Hiller, G. McCartor, Ann. Phys. **321**, 1240 (2006).

[156] G.C. Wick, Phys. Rev. **96**, 1124 (1954);

[157] R.E. Cutkosky, Phys. Rev. **96**, 1135 (1954).

[158] S.J. Brodsky, J.R. Hiller and G.McCartor, Phys. Rev. D **64**, 114023 (2001); [arXiv:hep-ph/0107038].

[159] G. Baym, Phys. Rev. **117**, 886 (1960).

[160] F. Gross, C. Şavklı, and J. Tjon, Phys. Rev. D **64**, 076008 (2001); [arXiv:nucl-th/0102041].

[161] W. Zimmermann, Comm. Math. Phys. **15**, 208 (1969).

[162] A.V. Smirnov, unpublished.

[163] V.A. Karmanov, Yang Li, P. Maris, J.P. Vary, Manuscript in preparation.

[164] K.E, Atkinson, "A Survey of Numerical Methods for the Solution of Fredholm Integral Equations of the Second Kind", Philadelphia: S.I.A.M., (1976).

[165] Y. Kim, I.J. Shin, T. Tsukioka, Prog. Part. Nucl. Phys. **68**, 55 (2013); [arXiv:1205.4852 [hep-ph]].

[166] N. Brambilla *et al.*, Eur. Phys. J. C **74**, 2981 (2014); [arXiv:1404.3723 [hep-ph]].

[167] V.T. Kim, G.B. Pivovarov and J.P. Vary, Phys. Rev. D **69**, 085008 (2004); [hep-th/0310216].

[168] D. Chakrabarti, A. Harindranath, L. Martinovic, G.B. Pivovarov and J.P. Vary, Phys. Lett. B **617**, 92 (2005); [hep-th/0310290].

[169] A. Misra, Phys. Rev. D **53**, 5874 (1996).

[170] S.J. Brodsky, F.-G. Cao, G.F. de Teramond, Phys. Rev. D **84**, 075012 (2011); [arXiv:1105.3999 [hep-ph]].

[171] B. Pasquini, S. Cazzaniga, and S. Boffi, Phys. Rev. D **78**, 034025 (2008); [arXiv:0806.2298 [hep-ph]].

[172] C.-R. Ji, Phys. Lett. B **322**, 389 (1994).

[173] J.J. Wivoda and J.R. Hiller, Phys. Rev. D **47**, 4647 (1993).

[174] J. Carbonell and V.A. Karmanov, Eur. Phys. J. A **27**, 11 (2006).

[175] C.-R. Ji and Y. Tokunaga, Phys. Rev. D **86**, 054011 (2012).

[176] C. Şavklı, J. Tjon and F. Gross, Phys. Rev. C **60**, 055210 (1999).

[177] X. Zhao, Few-Body Syst. **56**, 257 (2015).

[178] L. Chaos-Cador and E. Ley-Koo, Int. J. Quantum Chem. **97**, 844 (2004).